Electromagnetic modeling for SAR polarimetry and interferometry

Davod Poreh

Università degli Studi di Napoli Federico II

Reality is merely an illusion, albeit
a very **persistent** one.

Albert Einstein

This page intentionally left blank.

On the cover
Mean amplitude of an Italian CosmoSkyMed radar image of the northern part of Naples, together with PSs on the railway and nearby region.

Parts of this book have been published in the following journals/books:

D. Poreh, D. Riccio, "Building's subsidence observed in Mexico City by remote sensing data", Mapping urban areas from space conference, 4^{th} November 2015, ESA Frascati.

D. Poreh, A. Iodice, D. Riccio, G. Ruello, "Railways' stabilities observed in Campania (Italy) by InSAR data", IEEE Young Professional, 4-6 December 2015, Barcelona.

G. Di Martino, A. Iodice, D. Poreh and D. Riccio, "Soil moisture retrieval from polarimetric SAR data: a short review of existing methods and a new one", European Space Agency, ESA SP 740 (Proceedings of Living Planet Symposium 2016), Prague (Czech Republic), May 2016, CD-ROM.

G. Di Martino, A. Iodice, D. Poreh and D. Riccio, "Polarimetric SAR Raw Signal Simulation", Proceedings RiNEM 2016, Parma (Italy), September 2016, in print.

G. Di Martino, A. Iodice, D.Poreh, D. Riccio, "A fully polarimetric SAR raw signal simulator", IEEE Young Professional, 20-21October 2016 DLR Germany.

G. Di Martino, A. Iodice, D.Poreh, D. Riccio, "Pol-SARAS: a fully polarimetric SAR raw signal simulator and its application to soil moisture retrieval", Pol-InSAR conference in Frascati 2017.

D. Poreh, A. Iodice, D. Riccio, G. Ruello, "Railways' stability observed in Campania (Italy) by InSAR data", European Journal of Remote Sensing, vol.49, pp. 417-431, 2016.

D. Amitrano, V. Belfiore, F. Cecinati, G. Di Martino, A. Iodice, P.-P. Mathieu, S. Medagli, D. Poreh, D. Riccio, G. Ruello, "Urban Areas Enhancement in Multitemporal SAR RGB Images Using Adaptive Coherence Window and Texture Information", IEEE Journal of Selected Topics in

Applied Earth Observations and Remote Sensing, vol.9, no.8, pp. 3740-3752, 2016.

G. Di Martino, A. Iodice, D.Poreh, D. Riccio, "Pol-SARAS: a fully polarimetric SAR raw signal simulator for extended scenes", accepted for IEEE transaction papers.

G. Di Martino, A. Iodice, D.Poreh, D. Riccio, G. Ruello, "Physical models for evaluating the interferometric coherence of potential persistent scatterers", Proceedings on IGARSS 2017, Texas, USA.

G. Di Martino, A. Iodice, D.Poreh, D. Riccio, "A fully polarimetric SAR raw signal simulator", Proceedings on IGARSS 2017, Texas, USA.

D. Poreh, A. Iodice, D. Riccio, G. Ruello, "Railways' stability observation by satellite radar images", Book chapter in "Railway Engineering", InTECH, 2017 (ISBN 978-953-51-5571-3).

This page intentionally left blank.

Preface

In past decades, monitoring of the Earth's surface has brought lots of attention to research communities. The thought of monitoring Earth's surface from 800 kilometers altitude, with no instruments located on or touching it sounds crazy. This monitoring might be of any millimetric movements on the Earth's surface or man-made objects, water content of soil, the Earth's surface roughness, vegetation covers, ice thickness, etc. Continuing progress in physics since the nineties (or even earlier) has made satellite radar interferometry and satellite polarimetrey practically feasible.

Due to my long-held eagerness to learn these techniques, I have trained in radar satellite/airborne remote sensing, laser remote sensing, and passive satellite remote sensing in many European countries including Germany and Italy, consequently studying and producing many radar interferograms, persistent scatterers, polarimetiric data sets, airborne/sea laser data, topographic data, passive satellite data, etc. The extensive investigation and research while difficult, have given me the tools and techniques to answer some of the questions that we are facing. I hope the information in this book will make a meaningful contribution to the field and open new doors to innovative techniques.

Ludwig Wittgenstein once said " knowledge is in the end based on acknowledgment". Here I gratefully name some of the many people to whom I owe my research and my life: Foremost, I would like to thank Daniele Ric-

cio for his supervision and overall guidance. I certainly learned a lot from him, and not only about radar remote sensing. Ever inspiring through his constant enthusiasm and caring, Daniele enabled me to participate in many interesting projects with a strong belief in me over the years. Furthermore, I feel similarly indebted and grateful to Antonio Iodice for his kindness. In addition to really admiring his scientific mind and style of thinking, there was the pleasure of enjoying lots of good Italian food together for many years. I would especially also like to thank Giuseppe Ruello for his kind behavior and gentle manner.

I am also grateful to my colleagues at the ITEE-DIETI University of Naples in Italy: Alessio Di Simone, Domenico Antonio Giuseppe Dell'Aglio, Donato Amitrano, and Gerardo Di Martino, being in whose company represented the best time of my life in Italy.

Finally, I would like to thank the many other members of our department at the ITEE-DIETI University of Naples in Italy. I am sorry I cannot mention all of the people who joined us for shorter or longer terms over the years.

The satellite/airborne radar data sets used in this book have been provided by European Space Agency (ESA), Agenzia Spaziale Italiana (ASI), and National Snow and Ice Data Center (NSIDC). SRTM and AIRSAR data have been made available by National Aeronautics and Space Administration (NASA). Temperature data are from National Oceanic And Atmospheric Administration (NOAA). The background imagery in some of the figures in this book is obtained from Google Maps.

I greatly enjoyed the research and writing of this book, and hope the reader will similarly enjoy the content.

Contents

This page intentionally left blank.

Abstract

Electromagnetic modeling for SAR polarimetry and interferometry

Investigation of the globe remotely from hundreds of kilometers altitude, and fast growing of environmental and civil problems, triggered the necessity of development of new and more advanced techniques. Electromagnetic modeling of polarimetry and interferometry has always been a key driver in remote sensing research, ever since of the first pioneering sensors were launched. Polarimetric and interferometric SAR (Synthetic Aperture Radar) surveillance and mapping of the Earth surface has been attracting lots of interest since 1970s.

This thesis covers two SAR's main techniques: (1) space-borne Interferometric Synthetic Aperture Radar (InSAR), which has been used to measure the Earth's surface deformation widely, and (2) SAR Polarimetry, which has been used to retrieve soil and vegetation physical parameters in wide areas.

Time-series InSAR methodologies such as PSI (Permanent Scatterer Interferometry) are designed to estimate the temporal characteristics of the Earth's deformation rates from multiple InSAR images acquired over time. These techniques also enable us to overcome the limitations that conventional InSAR suffer, with a very high accuracy and precision. In this thesis, InSAR time-series analysis and modeling basis, as well as a case study in the Campania region (Italy), have been addressed. The Campania region is characterized by intense urbanization, active volca-

noes, complicated fault systems, landslides, subsidence, and hydrological instability; therefore, the stability of public transportation structures is highly concerned. Here Differential Interferometric Synthetic Aperture Radar (DInSAR), and PSI techniques have been applied to a stack of 25 X-band radar images of Cosmo-SkyMed (CSK) satellites collected over an area in Campania (Italy), in order to monitor the railways' stability. The study area was already under investigation with older, low-resolution sensors like ERS1&2 and ENVISAT-ASAR before, but the number of obtained persistent scatterers (PSs) was too limited to get useful results.

With regard to SAR polarimetry, in this thesis a fully polarimetirc SAR simulator has been presented, which is based on the use of sound direct electromagnetic models and it is able to provide as output the simulated raw data of all the three polarization channels in such a way as to obtain the correct covariance or coherence matrixes on the final focused polarimetic radar images. A fast Fourier-domain approach is used for the generation of raw signals. Presentation of theory is supplemented by meaningful experimental results, including a comparison of simulations with real polarimetric scattering data.

Nomenclature

List of acronyms

$1D$	One-dimensional
$2D$	Two-dimensional
$3D$	Three-dimensional
$ALOS$	Advanced Land Observing Satellite
AOI	Area Of Interest
APS	Atmospheric Phase Screen
$ASAR$	Advanced Synthetic Aperture Radar
ASI	Agenzia Spaziale Italiana
BSA	Back/Bi-static Scattering Alignment
c	Speed of light $= 300,000 km/s$
$crosspol$	cross-polarisation
$copol$	co-polarisation
$corr$	correlation coefficient
$COSMO$-$SkyMed$	COnstellation of small Satellites for the Mediterranean basin Observation
DEM	Digital Elevation Model
$DInSAR$	Differential Interferometric Synthetic Aperture Radar
DLR	Deutschen Zentrums fur Luft- und Raumfahrt (German Space Agency)

DoC	Degree of Coherency
DoP	Degree of Polarization
$DORIS$	Delft Object-oriented Radar Interferometric Software
EM	Electromagnetic field
$Envisat$	Environmental satellite
ERS	European Remote Sensing satellite
ESA	European Space Agency
fBm	fractional Brownian motion
FT	Fourier Transform
FFT	Fast Fourier Transform
GIS	Geographic Information System
GO	Geometrical Optics
IEM	Integral Equation Models
$InSAR$	Interferometric Synthetic Aperture Radar
ifg	Interferogram
KA	Kirchhoff Approximation
LOS	Line of Sight
$NASA$	National Aeronautics and Space Administration
$NSIDC$	National Snow and Ice Data Center
$P\{\cdot\}$	Probability Density Function
$P\{\cdot,\cdot\}$	Joint probability distribution function
PO	Physical Optics
$Pol\text{-}SAR$	Polarimetric SAR
PRF	Pulse Repetition Frequency
PS	Persistent/permanent Scatterer
PSC	Persistent Scatterer Candidate
PSI	Persistent Scatterer Interferometry
PSP	Permanent Scatterers Potentials
$PTSM$	Polarimetric Two Scale Model
$RADAR$	RAdio Detection And Ranging
$RADARSAT$-2	Launched in December 2007, Canada's next-generation commercial radar satellite
RCS	Radar Cross Section, $\sigma(\theta, \varphi)$
$ROI\text{-}PAC$	The Repeat Orbit Interferometry PACkage developed at JPL and Caltech

SAR	Synthetic Aperture Radar
$SBAS$	Small BAseline Subset
SNR	Signal-to-Noise Ratio
SLC	Single-Look Complex
SPM	Small-Perturbation Method
$SRTM$	Shuttle Radar Topography Mission
$StaMPS$	Stanford Method for PS
TSM	Two-Scale Models
TEM	Transverse ElectroMagnetic wave
$UAVSAR$	Unmanned Aerial Vehicle SAR
$WGS84$	World Geodetic System 1984

List of symbols

B	Baseline $[m]$
$B_{\parallel}$	Parallel baseline [m]
$B_{\perp}$	Perpendicular baseline [m]
B_{temp}	Temporal baseline [days]
$\underline{B}$	Magnetic flux density
$\underline{E}$	Electric field
$\underline{H}$	Magnetic field
$\underline{D}$	Electric flux density
ρ	Charge density
$\underline{J}$	Source vector current
ϵ	Permittivity
μ	Permeability
ω	Angular velocity/frequency
k	Wave number
τ	Pulse length
λ	Wave lenght
ξ	Impedance
f	Frequency
f_s	Received pulse sampling frequency
f_d	Doppler frequency
Δf	Chirp bandwidth
v_r	Radial velocity of the sensor
$\underline{R}$	Slant range vector
$\hat{u}$	Unit vector in the direction of u
D_P	Displacements of the point P
$I_0(\cdot)$	Modified Bessel function
$erfc(\cdot)$	Complementary error function, i.e., $erfc(x) = 1 - erf(x)$
$f_\theta(\cdot)$	Error distribution functions
$\underline{\underline{G}}\,(x, y)$	Dyadic Green's function
$\underline{\underline{I}}$	Unite dyad matrix
$R_{\parallel}$	Parallel Fresnel reflection component

$R_\perp$	Perpendicular Fresnel reflection component
n	Index of refraction
$\hat{h}$	Horizontal polarization
$\hat{v}$	Perpendicular polarization
ϑ_0	Scene-center look angle
ϑ_l	Local incidence angle
ϑ_i	Incidence angle
ϑ_s	Scattered angle
β	Orientation (or rotation) angle
S	Scattering matrix
$z(x, y)$	Stochastic process
H_t	Hurst coefficient
T	Topothesy
k	Isotropic roughness wavenumber
D	Fractal dimension
$\underline{r}$	Generic point
A	Illuminated area
$\langle f \rangle$	Statistical mean of f
$Q(\tau)$	fBm structure function
$\Gamma(\cdot)$	Gamma function
$W(\cdot)$	Power spectral density
$w(\cdot)$	Polarization-independent zero-mean circular complex Gaussian random variable
κ_x and κ_y	Fourier mates of x and y
$\underline{h}(\theta, \varphi)$	Effective antenna height
P_S	Scattered power density
G	Antenna gain
$\lvert f \rvert$	Amplitude of the f
$\underline{\underline{f}}^*$	Complex Conjugate of $\underline{\underline{f}}$
$\underline{\underline{f}}^\dagger$	Transpose of $\underline{\underline{f}}$
$\underline{\underline{T}}\ (x, y)$	Coherency matrix
$\underline{\underline{C}}\ (x, y)$	Covariance matrix
$\underline{\underline{Q}}\ (x, y)$	Stokes vector
$\underline{k}_L$	Lexicographic vector basis
$\underline{k}_P$	Pauli vector basis
Φ	Interferometric phase

φ_{atm}	Atmospheric contribution Phase
φ_{orb}	Orbital error Phase
φ_{def}	Displacement component of the total observed phase
φ_{scat}	Scattering component of the total observed phase
φ_{DEM}	Phase of the topographic contribution
φ_n	Noise component of the phase
D_a	Amplitude dispersion index
σ_φ	Phase standard deviation
φ_{ij}^{ms}	Phase double-difference
$h(x^{'}, r^{'})$	SAR raw signal
$\gamma(x, r)$	Reflectivity map
$g(\cdot)$	System impulse response
δa and δb	Independent identically distributed zero-mean Gaussian random variables
a_0 and b_0	Azimuth and range slopes prescribed by the external DEM
$p(x, y)$	Small-scale roughness parameter maps
$\sigma(x, y)$	Large-scale roughness parameter maps
$\sigma \equiv (\sigma_x, \sigma_y, \rho)$	Input large-scale roughness parameters
$\epsilon(x, y)$	Complex dielectric permittivity map
$W(k)$	Powre spectral density
$\underline{\underline{R}}_2(\beta)$	Unitary rotation matrix
F_H and F_V	Bragg (if SPM is used) or the Fresnel (if PO is used) coefficients for H and V polarization
x'	Azimuth coordinate of the antenna position
R	Distance from the antenna to the generic point of the scene
R_0	Distance from the line of flight to the centre of the scene
$u(\cdot)$	Azimuth illumination diagram of the real antenna over the ground
$X = \lambda R_0 / L$	Real antenna azimuth footprint
$rect[t/T]$	The standard rectangular window function, i.e., $rect[t/T] = 1$ if $\|t\| \leq T/2$, otherwise $rect[t/T] = 0$
r'	$c/2$ times the time elapsed from each pulse transmission

H	Entropy
α	An angle that is related to eigenvalues and eigenvectors of coherency matrix and used in H-α charts
SD	Standard deviation

Chapter 1

Introduction

While it is true that talk about satellite/airborne remotely sensed monitoring primarily brings to mind the obvious military and security implications, many studies carried out have indeed focused on the vital civilian applications, management, environments, oil and gas, transportation, pollutants, etc. Given that electromagnetic (EM) waves and their propagation, interaction with the medium, and transfer are known as the three main pillars of remote sensing techniques, modeling of EM fields in remote sensing, their scattering from surfaces, and interaction with the medium are really important.

One of the best features of remote sensing that makes it indispensible with respect to the other techniques, is the coverage of vast areas in a short time span, an ability that is more noteworthy especially when in situ inspections (i.e., ground truth and/or measured data) are not easily feasible. In some cases the study area can only be reached in by an aircraft, and visual inspection needing weather-reliant solar illumination and full coverage of a specific area requiring many flight missions, which is time consuming and costly. On the other hand satellites come to the same area periodically and collect data in strip or spot formats with different sizes varying from tens to hundreds of kilometers depending on the mission's preferences. With the satellite's constellation based arrangements, the visiting time would be improved dramatically. For instance, with respect to Italian CosmoSkyMed (CSK) [1] satellites which work in four constella-

tions (in X-band), the visiting time might be improved to around 12 hours. In this thesis we use Interferometric Synthetic Aperture Radar (InSAR), and Polarimetirc Synthetic Aperture Radar (Pol-SAR) data sets, to show the strength of the techniques. Both airborne and satellite data sets have been employed.

SAR is classified in the realm of active microwave remote sensing [2]. In the SAR arrangement systems, the technique provides the ability to produce very high (spatial) resolution radar imagery with signal processing. This practically means that the technique could enhance the discrimination criteria between different targets significantly. SAR surveillance has become very mature over more than 30 years of activities with airborne, satellite, and ground-based techniques. Some of the most important SAR sensors are: ERS1&2, ENVISAT-ASAR, RadarSAT, SIR-X, SIR-C, etc. And that of Polarimetirc SAR (i.e., Pol-SAR): ALOS-PALSAR (from Japan) [3], RadarSAT-2 (from Canada) [4], and TerraSAR-X (from Germany) [5, 6]. A new era of radar remote sensing began in 2014 when the Sentinel family (from ESA) satellites were sent into orbit. This large number of orbiting satellites (InSAR and Pol-SAR) emphasizes the significance of radar remote sensing techniques.

With optical remote sensing, despite many similarities with radar techniques, the main difference is that these satellites are not transmitting any EM fields, but just collecting the backscattered EM (illuminated) wave from objects (with the exception of the lidar systems). Another difference is the employment of different EM frequencies rather than radar frequencies (i.e., microwave frequencies). The scattering mechanism of EM field is highly dependent on the EM wavelength [2, 7]. As a quick result the area of applicability of these two different techniques (radar and optical) is noted. Preference for using active or passive remote sensing is dictated by the aim and data availabilities. Generally speaking, the EM field interacts with objects that are not smaller than its wavelength [2, 8]. Therefore, smaller objects become transparent to the remote sensing surveillance. For instance in the microwave region, clouds are transparent for the SAR systems (especially for low frequencies). This is an advantage for radar remote sensing, which is functional in any weather conditions [9]. Another advantage of radar techniques is the ability of penetration in vegetated areas, which itself is a function of employed wavelength [10].

In radar measurements, not only amplitude, but also the phase of the EM fields is measured. This measurement is the core aspect of interfermometry and polarimetric radar techniques [11, 12, 13]. In optical remote sensing only co- and cross-polarization of EM fields are collected with no phase measurements. Without phase measurements of EM fields, many acquisitions need to have a fully polarmetric image of the study area, which would increase the complexity of the sensors and data storage significantly.

The space-time behavior of the EM fields is described by the Maxwell equations, and one of the fundamental concepts of EM theory is polarization (or polarisation). Polarimetry deals with the geometrical aspect of the EM fields [6, 13, 14, 15] and relates to the shape that the EM field draws on a plane transverse to the propagation direction. When two different targets are illuminated with the same EM field and same polarization, they are likely to scatter the EM fields with different polarization states. Meanwhile, the polarization state can be used as a screening tool to differentiate the scatterers. Two different objects with different shapes and materials are expected to have different polarization signatures. To fully describe the polarimetric behavior of the targets, at least four acquisitions are needed. In case of reciprocity of the cross polarization, this might be decreased to three channels. Such an arrangement is known as "fully polarimetric" signature of the targets. In case of limitation of budgets, hardware, request for higher resolution imageries, and need for small amount of data storage, dual-arrangement is employed.

1.1 Electromagnetic modeling for SAR interferometry

Since the late 1980's space-borne Interferometric Synthetic Aperture Radar (InSAR) has been used to widely measure the Earth's surface deformation. Consequently with this technique, the effects of earthquake, volcanism, oil and gas extraction, groundwater flow, ice motion, and natural civil processes such as landslide, subsidence, sinkholes, etc, can be measured with very high accuracy and precision with wide-scale coverage over a short time span. Moreover, the InSAR data archive is available since 1992 from launch of the ERS-1 satellite; a big advantage for studying any historical movement of the Earth's surface in many spots across the globe.

However, despite the excellent performance of the conventional InSAR methodologies, temporal decorrelation -decrease in similarity between images-, geometrical decorrelation, and phase delay due to atmospheric effects on EM fields, are three major limitations of the application. But for some specific conditions like urban areas or terrain surfaces having rock outcrops (for which there are good scatterers for EMs), temporal decorrelation decreases dramatically, and features remain coherent in the interferograms produced for a long temporal baselines [16, 17, 18, 19]. To overcome the coherency problems of backscatterers (coherency changes in the backscatters during the time period considered) in repeat pass SAR interferometry, Permanent Scatterers Interferometry (PSI) was developed at Politecnico di Milano (POLIMI-university of Milan) by A.Ferretti, F.Rocca, and C.Prati [20, 21].

With respect to this new InSAR technique, some radar pixels remain coherent during the time period considered. With this method and by using a large stack of InSAR images (usually more than 20 images), atmospheric errors (which refer to Atmospheric Phase Screen, APS) also could be estimated sufficiently, and in the general phase equations, phase could be corrected accordingly. In the standard PSI methodologies, a single master image with specific criteria is selected (from N images), and $N-1$ differential interferograms w.r.t. the master image are generated. Then, with different approaches, PSCs (Permanent Scatterer Candidates) are selected. By refinements of the selected PSCs, and PSPs (Permanent Scatterer Potentials) final PSI points can be generated. The output of PSI algorithms are deformation time series of the scatterers, and the elevation of those scatterers.

This methodology shows promising results in urban areas, where it is able to achieve an average of 100 PSs/km^2 (points densities) with low resolution sensors like ERS1&2 and ENVISAT-ASAR, and an average of a couple of thousands PSs/km^2 with high resolution sensors like TerraSARX and Cosmo-SkyMed (CSK). On the contrary, rural/vegetated areas may not be explored properly with PSI methodology, mainly due to the absence of proper scatterers in rural/vegetated areas, and change in coherence of the illuminated area during the time period considered . Another disadvantage of the PSI is the need for a minimum amount of images for performing appropriate phase unwrapping steps, which could severely

influence the degree of correctness of the selected PSC. This limitation is resolved with a newer methodology known as Small BAseline Subset (SBAS) [22, 23]. In SBAS, far more interferograms are created than in a single master approach (like PSI). The unwrapping procedure for SABAS and PSI also differ: in SBAS, at least in its original implementation, the interferograms are unwrapped first spatially and then temporally, while it is the opposite in the PSI analysis. InSAR time series methodologies are relational, i.e, all the time series that are calculated for PS points, are measured w.r.t. a reference point. But, many promising methodologies, like Continuous GPSs (C-GPS), could resolve this problem properly. The main test/control of a PS being a real scatterer (not just a statistical consequence of a series of analysis) is by using C-GPS stations, although, test of ensample coherence distributions is also a weaker criteria.

1.2 Electromagnetic modeling for SAR polarimetry

Recently, polarimetric Synthetic Aperture Radar has been successfully applied to soil moisture retrieval, forest monitoring, change detection and marine applications [6]. Meanwhile, a polarimetric SAR raw signal simulator, based on a sound physical electromagnetic scattering model, would be certainly useful for mission planning, algorithm development and testing, and prediction of suitability of the system to different applications. This simulator should be able to consider extended scenes, whose macroscopic topography is possibly prescribed by an external Digital Elevation Model (DEM), and to account for terrain roughness and soil electromagnetic parameters. Simulated raw signals of the different polarimetric channels, when focused via standard SAR processing algorithms, should lead to a realistic polarimetric covariance (or coherency) matrix. In this thesis, we present a new simulator that we named "Pol-SARAS": a fully polarimetric version of the available SARAS [24, 25, 26, 27], a pretty old model-based raw signal simulator that was made by ITEE-DIETI University of Naples in Italy. SARAS can only simulate one polarimetric channel at a time, with the result that the data of different channels turn out to be independent. Accordingly, although the correct relations between the polarimetric channels' powers are obtained, the covariance (or coherence)

matrix of the final images is not realistic. This improvement now enables the Pol-SARAS to simultaneously produce the raw signals of the different polarimetric channels in such a way as to obtain the correct covariance or coherence matrices on the final images. Pol-SARAS only considers surface scattering, but, due to the modular structure of the simulator, other scattering mechanisms (volumetric, double bounce) can also be included, if reliable models are available.

1.3 Thesis contents

(i) The second chapter introduces the EM concepts that advantageously facilitat understanding of the InSAR and Pol-SAR analysis and modeling. For the sake of brevity, we concentrate on the subjects that are related to the techniques.

(ii) The third chapter is dedicated to understanding of the Interferometric Synthetic Aperture Radar (InSAR), providing the basic tools and fundamental knowledge for the development of the techniques.

(iii) The fourth chapter concerns about the PSI analysis and modeling that was carried out for a case study in the Campania region, Italy. We apply the DInSAR and PS technique to the remote monitoring of railways in the Campania region. In particular, we are interested in monitoring a bridge over the Volturno river, at Triflisco. As widely reported in the literature, the Campania region is very unstable in terms of the Earth surface deformations. Therefore this area must go under geo-based investigation periodically. In addition, in the Campania region, the railways and bridges are pretty old, and are prone to sudden or slow deformation threats. For instance, the bridge over the Volturno river and the railways considered in this study were built in 1953. To evaluate possible deformation of this bridge, employment of high resolution Cosmo-SkyMed radar images is proposed, and an InSAR/PSI analysis has been carried out. The results presented here show fairly stable conditions on the studied railways and the main targeted bridge, with periodic thermal deformation.

(iv) The fifth chapter is dedicated to the Pol-SARAS simulator descriptions. Firstly, the rationale of the proposed simulator is given, highlighting similarities and differences with the available SARAS (the older version). Section (5.4) is dedicated to the description of simulation results. In particular, in Section (5.4.1) the polarimetric coherency matrixes obtained from simulated data are compared with those obtained by available approximate analytical scattering models; in Section (5.4.2) a comparison between simulated and real polarimetric data is presented; and in Section (5.4.3) potential applications of the simulator to soil moisture retrieval and azimuth terrain slope retrieval from SAR polarimetric data are illustrated. Finally, concluding remarks are reported in Section (5.5).

(v) The last chapter deals with the conclusions and results in this thesis.

Bibliography

[1] AGENZIA SPAZIALE ITALIANA (2007) *COSMO-SkyMed SAR Products Handbook.*

[2] Rothwell EJ, Cloud MJ (2001) *Electromagnetics.* CRC Press, Boca Raton.

[3] ALOS (2007) *Information on PALSAR product for ADEN users.*

[4] Slade B (2009) *RADARSAT-2 product description.* Dettwiler and Associates, MacDonals.

[5] Fritz T, Eineder M (2009) *TerraSAR-X, ground segment, basic product specification document,* DLR.

[6] Lee JS, Pottier E (2009) *Polarimetric radar imaging: from basics to applications.* CRC Press, Boca Raton.

[7] Cloude RS (1995) *An introduction to wave propagation and antennas.* UCL Press, London.

[8] Stratton JA (1941) *Electromagnetic theory.* McGraw-Hill, New York.

[9] Richards JA (2009) *Remote sensing with imaging radarsignals and communication technology.* Springer, Berlin.

[10] Cloude SR, Corr DG, Williams ML (2004) Target detection beneath foliage using polarimetric synthetic aperture radar interferometry. *Waves Random Complex Media* 14:393414.

[11] Papathanassiou KP, Cloude SR (2001) Single-baseline polarimetric sar interferometry. *IEEE Transactions on Geoscience and Remote Sensing* 39:23522363.

[12] Cloude SR (2009) *Polarisation: applications in remote sensing.* Oxford University Press, 978-0-19-956973-1.

[13] Bamler R, Hartl P (1998) *Synthetic aperture radar interferometry.* Inverse Problems 14:154.

[14] Ulaby FT, Elachi C (1990) *Radar polarimetry for geo-science applications.* Artech House, Norwood.

[15] Zebker HA, Van Zyl JJ (1991) Imaging radar polarimetry: a review. *Proc IEEE,* 79.

[16] Usai, S. (1997), The use of man-made features for long time scale INSAR, *International Geoscience and Remote Sensing Symposium,* Singapore, 3-8 Aug 1997, pp. 15421544.

[17] Usai, S. and Hanssen, R. (1997), Long time scale INSAR by means of high coherence features, *Third ERS Symposium-Space at the Service of our Environment,* Florence, Italy, 17-21 March 1997, pp. 225228.

[18] Usai, S. and Klees, R. (1998), On the Feasibility of Long Time Scale INSAR, *International Geoscience and Remote Sensing Symposium,* Seattle, Washington, USA, 6-10 July 1998, pp. 24482450.

[19] Ferretti, A., Monti-Guarnieri, A., Prati, C. and Rocca, F. (1998), Multi-image DEM Reconstruction, *International Geoscience and Remote Sensing Symposium,* Seattle, Washington, USA, 610 July 1998, pp. 13671369.

[20] Ferretti, A., Prati, C. and Rocca, F. (1999a), Multibaseline InSAR DEM Reconstruction: The Wavelet Approach, *IEEE Transactions on Geoscience and Remote Sensing,* 37(2):705715.

[21] Ferretti, A., Prati, C. and Rocca, F. (2000), Nonlinear Subsidence Rate Estimation using Permanent Scatterers in Differential SAR Interferometry, *IEEE Transactions on Geoscience and Remote Sensing,* 38(5):22022212.

[22] Berardino P., Fornaro G., Lanari R., Sansosti E. (2002) - A new algorithm for surface deformation monitoring based on small baseline differential SAR interferograms. *IEEE Transactions on Geoscience and Remote Sensing.* 40, 23752383.

[23] Lanari R., Mora O., Manunta M., Mallorqui J.J., Berardino P., Sansosti E. (2004) - A small-baseline approach for investigating deformations on full-resolution differential SAR interferograms. *IEEE Transactions on Geoscience and Remote Sensing.* 42, 13771386.

[24] G. Franceschetti, M. Migliaccio, D. Riccio, and G. Schirinzi, "SARAS: a synthetic aperture radar (SAR) raw signal simulator, *IEEE Transactions on Geoscience and Remote Sensing*, vol.30, no. 1, pp.110 123, Jan. 1992.

[25] G. Franceschetti, R. Guida, A. Iodice, D. Riccio, and G. Ruello, "Efficient Simulation of Hybrid Stripmap/Spotlight SAR Raw Signal From Extended Scenes", *IEEE Transactions on Geoscience and Remote Sensing*, vol.42, no. 11, pp. 2385-2396, Nov. 2004.

[26] G. Franceschetti, A. Iodice, S. Perna, and D. Riccio, "SAR Sensor Trajectory Deviations: Fourier Domain Formulation and Extended Scene Simulation of Raw Signal", *IEEE Transactions on Geoscience and Remote Sensing*, vol.44, no. 9, pp. 2323-2334, Sept. 2006

[27] S. Cimmino, G. Franceschetti, A. Iodice, D. Riccio, and G. Ruello, "Efficient Spotlight SAR Raw Signal Simulation of Extended Scenes", *IEEE Transactions on Geoscience and Remote Sensing*, vol.41, no. 10, pp. 2329- 2337, Oct. 2003.

Chapter 2

Electromagnetic waves fundamentals

2.1 Maxwell's equations

The Principals of remote sensing are built on electromagnetic (EM) waves, their propagation, polarization (or polarisation), wave incidence/reflection, antenna patterns and thousands of other similar parameters. Electromagnetic waves are generated whenever an electrical charge changes its velocity [1, 2, 3]. When an electron in an atom moves from a higher to a lower energy level, it radiates a wave (EM) of particular frequency and wavelength. Electromagnetic waves and the aforementioned concepts may be better understood by starting with Maxwell's equations, which solely explain the entire theory of electricity and magnetism. These equations were introduced by James Clerk Maxwell in 1860, and can present the behavior of electric and magnetic fields at almost any point in space:

$$\begin{cases} \nabla \times \underline{E} &= -\frac{\partial \underline{B}}{\partial t}, \\ \nabla \times \underline{H} &= \underline{J} + \frac{\partial \underline{D}}{\partial t}, \\ \nabla \cdot \underline{B} &= 0, \\ \nabla \cdot \underline{D} &= \rho, \end{cases} \tag{2.1}$$

where $\underline{E}$, $\underline{H}$, $\underline{D}$, and $\underline{B}$, are the electric and magnetic fields, electric

flux density, and magnetic flux density respectively. Source vector currents $\underline{J}$ and the scalar charge density ρ in Maxwell's equations are the sources of the existing fields. In addition, each physical environment (even vacuum or free space) is characterized by two important parameters, ε, and μ, known as the permittivity and permeability of the wave respectively. For free space they are defined as:

$$\mu_0 = 4\pi \times 10^{-7} H/m, \qquad \varepsilon_0 = 8.854 \times 10^{-12} F/m,$$

The wave propagation equation stems from Maxwell's equations:

$$\nabla \times \nabla \times \underline{E} + \varepsilon_0 \mu_0 \frac{\partial^2 \underline{E}}{\partial^2 t} = -\mu_0 \frac{\partial \underline{J}}{\partial t}, \tag{2.2}$$

A wave that satisfies Maxwell's equations (and hence, the wave propagation equation), could have a general form, but for a start we consider the time harmonic regime:

$$\underline{E}(\underline{r}, t) = \underline{E}_0(\underline{r}) e^{j\omega t}, \tag{2.3}$$

where angular frequency $\omega = 2\pi f$ and f is the frequency of the propagated wave (in Hz).

By direct substitution of (2.3) in (2.2), the propagation wave would be changed to the Helmholtz equation, and has the solution in the form of [4]:

$$\underline{E}(x) = j\omega\mu_0 \iiint_V \underline{\underline{G}}(\underline{x}, \underline{y}) \cdot \underline{J}(y) dV, \tag{2.4}$$

This electric field can only be approximated by a plane wave, when the distance from the source tends to be infinite. The integration is calculated over the volume V, and the $\underline{\underline{G}}(\underline{x}, \underline{y})$ is known as the dyadic Green's function [2, 3]:

$$\underline{\underline{G}}(\underline{x}, \underline{y}) = (\underline{\underline{I}} - \underline{r}\,\underline{r})g + \frac{j}{KR}\left(\underline{\underline{I}} - 3\underline{r}\,\underline{r}\right)g - \frac{1}{K^2R^2}\left(\underline{\underline{I}} - 3\underline{r}\,\underline{r}\right)g, \tag{2.5}$$

where $\underline{\underline{I}}_{3\times3}$ is the unit dyad matrix, $R = |\underline{x} - \underline{y}|$, $r = \frac{(\underline{x}-\underline{y})}{|\underline{x}-\underline{y}|}$, and g is

the energy conservation factor, that also is known as scalar or free space Green's function:

$$g(x,y) = \frac{e^{-jk|\underline{x}-\underline{y}|}}{4\pi|\underline{x}-\underline{y}|}, \tag{2.6}$$

where $k = |\underline{k}| = 2\pi/\lambda$ is the wave number and λ is the wavelength of the propagated wave. In the limitation of $R \to \infty$ which shows movements away from the sources, just the first term of equation (2.5) dominate. In other words, the $\underline{\underline{G}}(\underline{x},\underline{y})$ will be:

$$\lim_{R\to\infty} \underline{\underline{G}}(\underline{x},\underline{y}) = \left(\underline{\underline{I}} - \underline{r}\,\underline{r}\right)\frac{e^{-jk|\underline{x}-\underline{y}|}}{4\pi|\underline{x}-\underline{y}|}, \tag{2.7}$$

which shows that, oscillation of the electric field is solely restricted to the plane perpendicular (known as polarization plane) to the propagation of the wave direction. For this reason, this kind of electromagnetic wave is known as Transverse ElectroMagnetic wave (TEM). With respect to the equations (2.1), and (2.4), i.e., by substitution of $\underline{J}$, the electric field in any point could be calculated.

For $\underline{J} = 0$, the source of EM waves does not exist, so, Maxwell's equations will be much easier to deal with. In this case, the only remaining problem is the evaluation of the electrical permittivity of the medium ε at any given point.

2.2 Electromagnetic scattering

In remote sensing, we are interested in the interaction/scattering of EMs with/from different materials, which change their amplitudes, directions, and polarizations accordingly. Generally speaking, there does not exist an analytic solution- except for simple natural surfaces - for the scattering field of EMs, only approximate solutions with usage of simple models for boundary conditions can be achieved. For example, in the case of sufficiently smooth surface, this surface will behave like a mirror, which is known as specular (from the Latin word for mirror) reflection, which could be characterized by the Fresnel coefficients for perpendicular and parallel components:

$$\begin{cases} R_{\perp} &= \frac{cos\vartheta_i - \sqrt{n^2 - sin^2\vartheta_i}}{cos\vartheta_i + \sqrt{n^2 - sin^2\vartheta_i}}, \\ R_{\parallel} &= \frac{\sqrt{n^2 - sin^2\vartheta_i} - n^2 cos\vartheta_i}{\sqrt{n^2 - sin^2\vartheta_i} + n^2 cos\vartheta_i}, \end{cases} \tag{2.8}$$

where $n = \sqrt{\mu\varepsilon}$, is the index of refraction ($n = 1$, for free space), and transmitted wave would be $1 + R$.

For natural surfaces (non-smooth surfaces), other models should be employed. While Kirchhoff Approximation (KA), Physical Optics (PO), Small-Perturbation Method (SPM), are among the best known models [5, 6], some others like Two-Scale Models (TSM), and Integral Equation Models (IEM), have also been the focus of interest in recent years [3, 7].

With some work on equations (2.4), (2.7), and Green's equality, the scattered and the transmitted EM from any surface i.e., Huygen's principle will be derived:

$$\underline{E}_s(r) = \int_S \left\{ j\omega\mu_0 \underline{\underline{G}}(r, r') \cdot \left[\hat{n} \times \underline{H}(r') \right] + \nabla \times \underline{\underline{G}}(r, r') \cdot \left[\hat{n} \times \underline{E}(r') \right] \right\} dS, \tag{2.9}$$

$$\underline{E}_t(r) = \int_S \left\{ j\omega\mu_0 \underline{\underline{G}}(r, r') \cdot \left[\hat{n}_d \times \underline{H}(r') \right] + \nabla \times \underline{\underline{G}}_d(r, r') \cdot \left[\hat{n}_d \times \underline{E}(r') \right] \right\} dS, \tag{2.10}$$

where $\hat{n}/\hat{n}_d$ is the unit vector to the surface of scattering/transferring at any point, $\underline{\underline{G}}$ and $\underline{\underline{G}}_d$ are the dyadic Green's functions for upper and lower parts of the reflecting media. These equations are only valid for harmonic time dependence and the vectors are complex. In Figure 2.1, the generic configuration of an EM wave (polarized one), that is incident upon the plane $x-y$ (with $\hat{k}_i$ unit vector) and scattered from this surface is given. For a backscatterer case that is of much interest in remote sensing, we have $\vartheta_i - \vartheta_s = \pi$. Two unit vectors of $\hat{h}$ and $\hat{v}$, are showing the directions of horizontal and perpendicular polarizations. $\hat{h}$ polarization is always perpendicular to the incidence/scatterer plane, while $\hat{v}$ always lies inside of the wave plane (perpendicular to $\hat{h}$).

Without loss of generality, we assume that the incident wave is a single (polarized) plane wave:

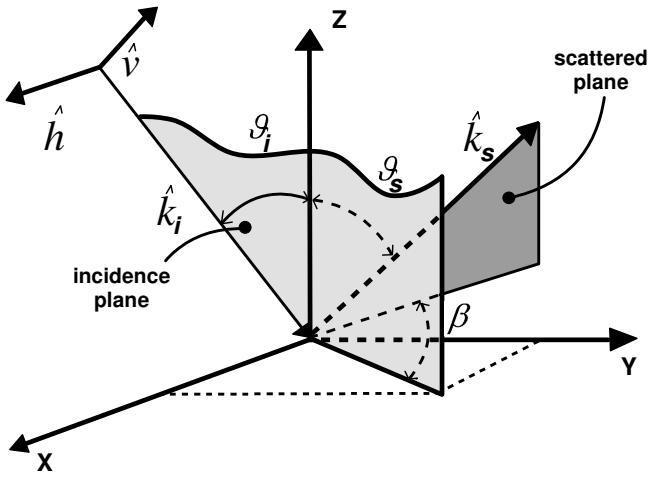

Figure 2.1. Configuration of EM wave scattering from a smooth surface is depicted. $\hat{v}$ is inside the wave incidence plane, and $\hat{h}$ is perpendicular to that.

$$\underline{E}_i = \hat{p} E_p e^{-j\underline{k}_i \cdot \underline{r}}, \tag{2.11}$$

where $\hat{p}$ is either $\hat{h}$ or $\hat{v}$ describing the polarization vectors (see Figure 2.1). With this configuration, the magnetic field of the incident wave would be found:

$$\underline{H}_i = \hat{k}_i \times \underline{E}_i / \xi, \tag{2.12}$$

where ξ is the Impedance. On the other hand, each of the electrical and magnetic fields could be decomposed in the polarization vector directions:

$$\underline{E}_i = \underline{E}_v \hat{v} + \underline{E}_h \hat{h}, \tag{2.13}$$

with similar representations for $\underline{H}_i$, $\underline{H}_s$, and $\underline{E}_s$. It is a rule that whenever incident wave and the propagation media are presented, the scattered vectors could be calculated (at least approximately).

The scattering matrix of an EM wave, S, in the far-field approximations leads us to the scattering component of the electrical field:

$$\underline{E}_s = -\frac{jke^{-jkr}}{4\pi r} S \cdot \underline{E}_i, \tag{2.14}$$

where the scattering matrix S has the form of:

$$S = \begin{bmatrix} S_{hh} & S_{hv} \\ S_{vh} & S_{vv} \end{bmatrix}, \tag{2.15}$$

The mathematical models mentioned in the beginning of this section are widely used to address the scattering matrix S. The next sections, explain some of the important scattering models for natural surfaces, and their brief applications.

2.3 How rough is rough?

Understanding the roughness of a surface is not always easy. One of the best criteria for this task is the Rayleigh criterion (after the third Baron Rayleigh). Imagine an EM wave incident on a natural surface at an angle of ϑ_i, and scattered specularly from its surface with the same angle i.e., $\vartheta_s = \vartheta_i$, the time delay between these two radiated rays, one from the upper surface (plane b in Figure 2.2), and the other from the lower surface (plane a), is the criterion. For this task, we make a reference plane (a) and a plane (secondary plane) above this reference plane (b), with height deviation of Δh (i.e., height changes of the surfaces a and b). The phase difference dictated by the roughness reads:

$$\Delta\varphi = \frac{4\pi\Delta h cos\vartheta_i}{\lambda}, \tag{2.16}$$

The surface will be practically smooth/rough, if we make some conditions for $\Delta\varphi$. For $\Delta\varphi < \pi/2$ (as a conventional value for a surface being smooth), we will get $\Delta h < \frac{\lambda}{8cos\vartheta_i}$. Some other criteria like $\Delta\varphi < 4\pi/25$, are also proposed in the literature. For instance, in the normal incident (i.e., $\vartheta_i = 0$), the surface is smooth if $\Delta h < \frac{\lambda}{8}$, which for radar band $X(\lambda = 2.5 - 4.0cm)$, will be less than half of a centimeter $\Delta h < 0.5$.

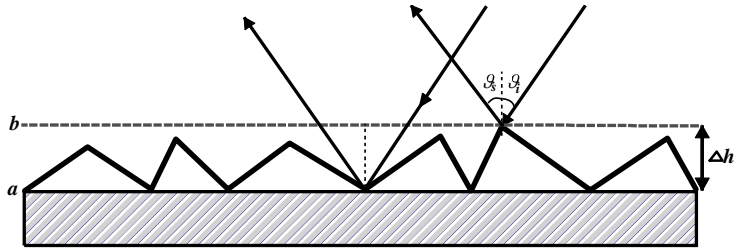

Figure 2.2. Two rays are specularly reflected with angle of $\vartheta_s(=\vartheta_i)$ from two planes with height deviation of Δh.

2.4 Classical solutions for the scattering from natural surfaces

In this section some of the well-known solutions for electromagnetic scattering from natural surfaces are given. Natural surfaces exhibit statistical scale invariance properties that are not satisfied by classical surface models, meanwhile fractal modeling would be an ideal proxy for the classical approaches. In this book we use fractal scattering surfaces for our analysis. For more details about fractal analysis of surface scattering see [6, 8].

A stochastic process $z(x, y)$ describes a fractional Brownian motion (fBm) surface if, for every x, y, x', y', it satisfies the following relation:

$$P\{z(x,y) - z(x',y') < \bar{\xi}\} = \frac{1}{\sqrt{2\pi}\tau^{H_t}} \int_{-\infty}^{\bar{\xi}} exp\Big(- \frac{\xi^2}{2s^2\tau^{2H_t}}\Big) d\xi, \quad (2.17)$$

where $\tau = \sqrt{\tau_x^2 + \tau_y^2} = \sqrt{(x-x')^2 + (y-y')^2}$, H_t is the Hurst coefficient, and s is the incremental standard deviation with the dimension of m^{1-H_t}. [8] showed that in the case of $0 < H_t < 1$, such a process ideally exist (with a probability of one), and exhibits a self affinity with a fractal dimension of $D = 3 - H_t$. Note that the fBm process is defined with two parameters and is non-stationary [8]. However, according to (2.17), its increments over any fixed horizontal distance τ are stationary isotropic zero mean Gaussian processes, with a variance of $s^2\tau^{2H_t}$. Furthermore, the slope of chords joining points on the surface at fixed distance of τ, is

a Gaussian random variable with a root mean square (rms) value equal to s/τ^{1-H_t}.

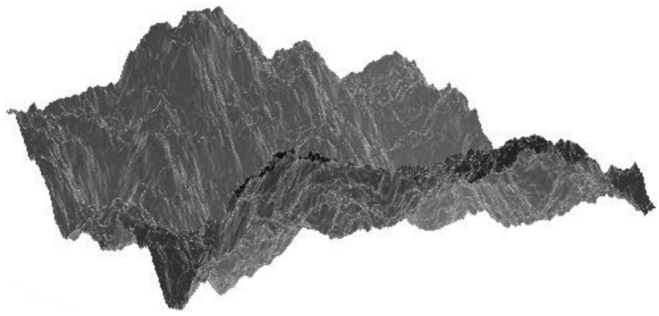

Figure 2.3. fBm surface for $H_t = 0.9$ and $s = 0.7m^{0.1}$.

An example of fBm surface is given in Figure 2.3.

By using the fBm definition, computation of the close form of scattering power density via Kirchhoff Approach (KA) and Small Pertubation Method (SPM) is possible (see for instance [8]).

2.4.1 The Kirchhoff Approximation (KA)

One of the most popular mathematical models for surface scattering approximations is the Kirchhoff model (named after Gustav Kirchhoff). In the Kirchhoff Approximation (KA), the scattered field tangent to the surface of incident field is approximated. For each point of the surface, the local incidence angle is evaluated, with respect to the tangential plane changes (which itself has been provided with the local normal vector $\hat{n}$). Hence, the KA model is sometimes known as tangent plane approximation, and KA could be divided in two modules:

- Physical Optics (PO model), which is valid for rougher surfaces, and,
- Geometrical Optics (GO model).

The PO model has appeared frequently in the literature and has recently attracted lots of interest. Imagine that the relative permittivity of the two media (separated by reflecting surface) would be ε_r, and by

far field approximation, the incident field could be considered as a locally plane wave with linear polarization.

For any given generic point of $\underline{r} = \big(x, y, z(x,y)\big)$, we have:

$$\underline{E}^i(\underline{r}) = \hat{p} E_p e^{-j\underline{k}_i \cdot \underline{r}}, \tag{2.18}$$

where $\hat{p} = \hat{h}$ or $\hat{v}$, describes the polarization of the field (see Figure 2.1), and $k_i = k(sin\vartheta_i, 0, -cos\vartheta_i)$ where k is the wavenumber. Similar definitions exist for scattering polarization vector $\hat{q}$. By using the KA and the small-slope approximation, the generic component of the scattered filed in Fraunhofer region (far field region) is expressed by following [9]:

$$\hat{q} \cdot \underline{E}^s(\underline{r}) = E_{pq} = \frac{jkE_p e^{-jkR_0}}{4\pi R_0} f_{pq}(\vartheta_i, \vartheta_s, \beta) \iint_A e^{-j\underline{u}\cdot\underline{r}'} dA, \tag{2.19}$$

where $\underline{u} = \underline{k}_i - \underline{k}_s$, and $\underline{k}_s$ is the scattering vector,

$$\begin{cases} u_x &= k(sin\vartheta_i - sin\vartheta_s cos\beta), \\ u_y &= -ksin\vartheta_s sin\beta, \\ u_z &= -k(cos\vartheta_i + cos\beta), \end{cases} \tag{2.20}$$

where ϑ_i is the incidence angle, ϑ_s, and β are the scattering angles (see Figure 2.1), A is the illuminated area, R_0 is the distance from center of A to the receiver, and f_{pq} is a dimensionless function depending on incidence, scattering angles, their polarizations (i.e., $\hat{p}$ and/or $\hat{q}$), and ϵ_r.

With consideration of the PO solution, the mean square value of the generic component of the scattered field would be

$$\langle |E_{pq}|^2 \rangle = \frac{k^2 |E_p|^2 |f_{pq}|^2 A}{(4\pi R_0)^2} I, \tag{2.21}$$

where the term I is the (polarization independent) Kirchhoff scattering integral

$$I = \iint_A exp\Big\{-ju_x\tau_x - ju_y\tau_y\Big\} exp\Big\{-\frac{1}{2}u_z^2 Q(\tau)\Big\} d\tau_x d\tau_y, \tag{2.22}$$

where $Q(\tau)$ is the fBm structure function defined as

$$Q(\tau) = \langle |z(x,y) - z(x',y')|^2 \rangle = s^2 \tau^{2H_t}, \tag{2.23}$$

Integral of equation (2.22) can be expressed as [8]

$$I = 2\pi \begin{cases} 2H_t \sum_{n=1}^{+\infty} \frac{(-1)^{n+1} 2^{2nH_t}}{n!} \frac{n\Gamma(1+nH_t)}{\Gamma(1-nH_t)} \frac{(\sqrt{2}|u_z|s/2)^{2n}}{(u_x^2+u_y^2)^{nH_t+1}} & ,H_t \leq 1/2 \\ \frac{1}{2H_t} \sum_{n=0}^{+\infty} \frac{(-1)^n}{2^{2n}(n!)^2} \Gamma\left(\frac{1+n}{H_t}\right) \frac{(u_x^2+u_y^2)^{2nH_t+2}}{(\sqrt{2}|u_z|s/2)^{\frac{2n+2}{H_t}}} & ,H_t \geq 1/2 \end{cases} \tag{2.24}$$

being $\Gamma(\cdot)$ the Gamma function. The truncation criteria of I are detailed in [10]. For the case of backscattering (i.e., $\varphi_s = \pi$ and $\vartheta_s = \vartheta_i$), $f_{pq} = 0$ for $p \neq q$, and $f_{pq} = -2R_p(\bar{\vartheta})/cos\vartheta_i$ for $p = q$, with R_p being the surface Fresnel reflection coefficient

$$R_p(\vartheta) = \begin{cases} \frac{cos\vartheta - \sqrt{\epsilon_r - sin^2\vartheta}}{cos\vartheta + \sqrt{\epsilon_r - sin^2\vartheta}} & ,p = h \\ \frac{\epsilon_r cos\vartheta - \sqrt{\epsilon_r - sin^2\vartheta}}{\epsilon_r cos\vartheta + \sqrt{\epsilon_r - sin^2\vartheta}} & ,p = v \end{cases} \tag{2.25}$$

These equations are evaluated at $\bar{\vartheta} \neq 0$ for small incidence angles and/or large roughness with respect to the wavelength, and at $\bar{\vartheta} \cong \vartheta_i$ for large incidence angle and small roughness with respect to the wavelength [11, 12].

If the surface models are adequate and the KA approximations are valid, the aforementioned formulas could be employed.

The equation (2.17) satisfies many natural surfaces in a wide but limited range of scale lengths, which is known as the range of fractalness, while, the valid scattering surface models must be employed in the permitted range of fractalness.

[6] show that depending on the scattering directions, a value τ^* exists, such that scale lengths much smaller or much larger than τ^* do not appreciate the scattering process efficiently. In the case of backscattering, τ^* is given by

$$\tau^* = \left(\frac{\lambda}{4\pi s \sqrt{H_t} cos\vartheta_i} \right)^{\frac{1}{H_t}}, \tag{2.26}$$

Meanwhile, in the microwave frequencies, most natural surfaces can be modeled as fractals. The validity of KA holds if the surface mean radius of curvature is much greater than the wavelength, while the small slope approximation can be used if the rms slope is much smaller than unity. Both of these conditions are met [6] if

$$\frac{s}{k\big(10/\tau^*\big)^{2-H_t}} \ll 1, \tag{2.27}$$

2.4.2 The Small Perturbation Method (SPM)

In the case of small surface variations (small roughness) with respect to the incident wavelength, and small slope of the rough (fractal) surfaces, perturbative approach could be used. [6] and [13] show that with use of Rayleigh hypothesis and surface field series expansion, the Small Perturbation Method (SPM) enables expressing the backscattered power density as

$$\langle |E_{pq}|^2 \rangle = \frac{|E_p|^2 4A|k^2 \beta_{pq} cos^2\vartheta|^2}{(2\pi R_0)^2} W(2ksin\vartheta), \tag{2.28}$$

where $W(\cdot)$ is the polarization independent power spectral density of the fBm process

$$W(k) = S_0 k^{-\eta}, \tag{2.29}$$

with $k = \sqrt{k_x^2 + k_y^2}$ (being k_x and k_x the Fourier mates of x and y), and S_0 and η the spectral parameters, given by

$$\begin{cases} S_0 &= s^2 2^{2H_t} 2\pi H_t \frac{\Gamma(1+H_t)}{\Gamma(1-H_t)}, \\ \eta &= 2 + 2H_t = 8 - 2D, \end{cases} \tag{2.30}$$

The coefficient β_{pq} in the backscattering direction for $p \neq q$ is equal to $\beta_{pq} = 0$, and for $p = q$ it reads

$$\beta_{pq}(\vartheta) = \begin{cases} \frac{cos\vartheta - \sqrt{\epsilon_r - sin^2\vartheta}}{cos\vartheta + \sqrt{\epsilon_r - sin^2\vartheta}} & ,p = h \\ (\epsilon_r - 1)\frac{sin^2\vartheta - \epsilon(1 - sin^2\vartheta)}{(\epsilon_r cos\vartheta + \sqrt{\epsilon_r - sin^2\vartheta})^2} & ,p = v \end{cases} \tag{2.31}$$

Note that the equation (2.28) holds only within the range of fractalness of the surface and only if $s/\lambda \ll 1$.

2.4.3 Two-Scale Model (TSM)

The Two-Scale Model (TSM) is among the most valuable and widely used models and is discussed in greater detail in the next chapters, where new model of Polarization Two Scale Model (PTSM) and Polarimetric Two-Scale and Two-Component Model (PTSTCM) will be addressed. This section, addresses just the elementary approach of TSM.

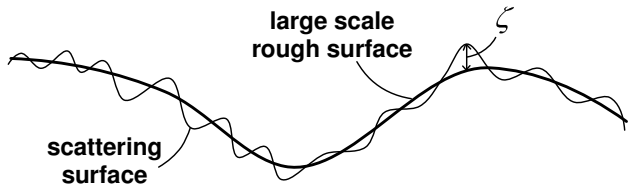

Figure 2.4. TSM model representation: small scale roughness superimposed on the large scale fluctuations.

Usually in nature, surfaces exist in two different scales ζ_1 and ζ_2, regional and local scales (Figure 2.4), thus making representation of a surface with just KA or SPM, somewhat is difficult and possibly not sufficiently valid. Therefore, the TSM model has been developed to overcome this problem. Mathematically speaking, TSM could be represented as a superposition of KA and SPM methodologies, with SPM taking care of the small roughness changes, and KA responsible for the local slopes:

$$TSM = KA + SPM, \tag{2.32}$$

For brilliant examples of TSM applications in practice, readers may refer to the sea surfaces monitoring in [14].

2.4.4 Integral Equation Model (IEM)

Practically speaking, KA is often used for high frequency approximations, and mostly $\vartheta_i < 20°$, on the other hand, SPM is suitable for low frequencies and $20° < \vartheta_i < 84°$. As mentioned earlier, in the equation (2.32),

TSM is a combination of KA and PSM, which inherently limits them in respect of both methods. For overcoming this limitation, [11] modified KA in a manner that could handle rapid fluctuations of the illuminated surfaces, and named this methodology, Integral Equation Model (IEM). This model is valid given the condition $k\zeta \cdot kl < 1.2\epsilon^{0.5}$, where k is the wavenumber, l is the correlation lenght, ζ is the root-mean-square height, and ϵ is the dielectric (relative) constant.

2.5 Radar Cross Sections (RCS)

When the EM wave is incident on a natural object, the incident energy spreads in all directions. This dispersal is known as scattering, and the resulting field distribution of the reflected energy (scattered wave), depends on many factors like the target's geometry, ϵ, λ, direction of wave arrival/incidence, and wave polarizations. The object that scattered the energy is called scatterer, and the spatial distribution of the scattered energy is known as scattering cross section. Post World War II, besides the speed, weight, and payloads of targets, RCS has become one of the main intrinsic specifications of objects in radar based topics. With definition of RCSs, engineers from different disciplines can understand each other properly. RCS has been used with numerous branches of engineering like aircraft design, jet propulsions, aerodynamic design, structural design, remote sensing, and many other similar disciplines.

For definition of RCSs in radar remote sensing, we need to compare two power densities: one measured at the target, and the other at the radar receiver.

The electric field distribution of a radar wave that is propagated by an antenna is given by:

$$\underline{E}(r,\theta,\varphi) = \frac{j\xi I}{2\lambda r} e^{-jkr} \underline{h}(\theta,\varphi), \tag{2.33}$$

where I is the current field, ξ is the impedance, and $\underline{h}(\theta,\varphi)$ is the effective antenna height of the transmitter. The power density of the incident wave at any point reads:

$$S(r,\theta,\varphi) = \frac{1}{2\xi} |\underline{E}_i(r,\theta,\varphi)|^2, \tag{2.34}$$

We assume that a scatterer behaves like an antenna, and an effective capture area σ, extracts a portion of the incident power:

$$P = \sigma \cdot S(r, \theta, \varphi) = \sigma \cdot \frac{1}{2\xi} |\underline{E}_i(r, \theta, \varphi)|^2, \tag{2.35}$$

We also assume that our target scatters the captured energy in all directions, and our target's dimensions are small compared to r. The RCS value $\sigma(\theta, \varphi)$ would be:

$$\sigma(\theta, \varphi) = \lim_{r \to \infty} \frac{P}{\frac{1}{2\xi} |\underline{E}_i(r, \theta, \varphi)|^2}, \tag{2.36}$$

Practically, RCS is the ratio of the scattered EM wave to the incident one. The capture area σ, is known as radar cross section or scattering cross section of the target/scatterer, and could be measured from equation (2.36). There are many other ways to measure σ, rather than measuring electric fields and r, by making use of the equation (2.36). In this equation, scatterers are assumed to be point scatterers with no dimension, something that is not always true. As a rule of thumb, the higher the RCS value of an object, the easier it is for it to be identified as a radar scatterer. But this definition is closly related to the wavelength λ of the radar waves, and direction of illuminations and scattering. In equation (2.36) the limitation $r \to \infty$, stresses this point that $\sigma(\theta, \varphi)$ is not dependent on the r, in other words, the $\sigma(\theta, \varphi)$ in this equation is standardized. $\sigma(\theta, \varphi)$ of targets, can be measured and/or calculated analytically too. RCSs of elementary objects like dihedrals, trihedrals, dipoles, etc, are given in many radar text books. Normalized Radar Cross Section (NRCS) is just evaluation of $\sigma(\theta, \varphi)$ inside an area like A which consists of many scatterer objects:

$$\sigma^0 = \lim_{r \to \infty} \frac{4\pi r^2 \langle |\underline{E}_s(r, \theta, \varphi)|^2 \rangle}{A |\underline{E}_i(r, \theta, \varphi)|^2}, \tag{2.37}$$

where symbol $\langle f \rangle$ stands for the statistical mean of f.

The radar cross section $\sigma(\theta, \varphi)$, will lead us directly to the term of the radar equation. The radar equation accounts for, radar system parameters, target parameters, background attributions like noise, and propagation effects/mediums. If we assume same antenna gains for transmitter and the receivers $G_T = G_R = G$, the received power of the signal will be:

$$P_R = \frac{P_T G^2 \sigma \lambda^2}{(4\pi)^3 / r^4}, \tag{2.38}$$

where P_R , P_T, are the received and transmitted powers respectively, and G is the antenna gain for both transmitter and the receivers.

2.6 Radar polarization

Viking's tales say that calcite mineral $CaCo_3$ was used frequently for ship navigations in foggy conditions, which may be the beginning of the polarimetric world (about AD 1000). The first classical use of polarimetry dates back to 1669 A.C, where Erasmus Bartholinus a Danish philosopher recognized a double picture appearance from a single object, when a calcite mineral was used. Long after the Erasmus era, in 1809 Etienne Malus (1775-1812) used the word "Polarization" to express the transverse effects of light. Isaac Newton (1643-1727) also talked about the "edge of the lights", which shows he had some sort of understanding about "polaride lights". Around 1845, Michael Faraday who was known for many electromagnetic field observations and experiments, vigorously talked about the polarimetric act of light. The works of James Clark Maxwell (1831-1879), theoretically strengthened the idea of the polarimetric parts of light offering the benefit of his well known equations, which can solve any kind of light behavior including ploarimetry. After Maxwell's great involvement, Gorge Stokes a mathematician from Cambridge (UK) also made valuable attempts in polarimetry in 1852. In the late nineteenth century, French mathematician, Henry Poincaré developed a $3D$ representation of polarized light on his famous sphere. The twentieth century was the start of a big endeavor on Maxwell's equations, which developed greatly with quantum mechanics. People like Sinclair, Kennaugh, and Huynen made further great contributions to polarimetric radar imaging in the 1940s, which was followed by the works of Ulaby, Fung, Valenzuela, Plant, and Alpers.

More recently, in 1988 NASA's AirSAR aircraft provided full polarimetic radar imaging in P-, L-, C-bands simultaneously, and was in operation till 2004, being followed in 2009 by AirSAR's Successor: the very high resolution L band Unmanned Aerial Vehicle SAR (UAVSAR), which is presently still in operation.

In space-borne polarimetirc SARs, many sensors are able to generate polaimetric images, namely: SIT-C/X-SAR (NASA+Germany+Italy), ENVISAT-ASAR (ESA), ALOS-PALSAR 1 and 2 (Japan), RADARSAT-2 (Canada), TerraSAR-X (Germany), Sentinel-1 (ESA), RCM (Canada), and CosmoSkyMed (Italian four constellation satellites).

Some of the radar remote sensing polarization usages, like recognition of targets, classifications, soil moisture, surface roughness, DEM generations, urban areas, etc, are covered in these literature [3, 7, 15, 16, 17].

2.6.1 Polarization ellipse

Imagine a planar wave is propagating in $\hat{z}$ direction with the electric field of

$$\underline{E} = \underline{E}_x\hat{x} + \underline{E}_y\hat{y} = |\underline{E}_x|e^{j\varphi_x}\big(\hat{x} + \hat{y}\frac{|\underline{E}_y|}{|\underline{E}_x|}e^{j(\varphi_y-\varphi_x)}\big), \tag{2.39}$$

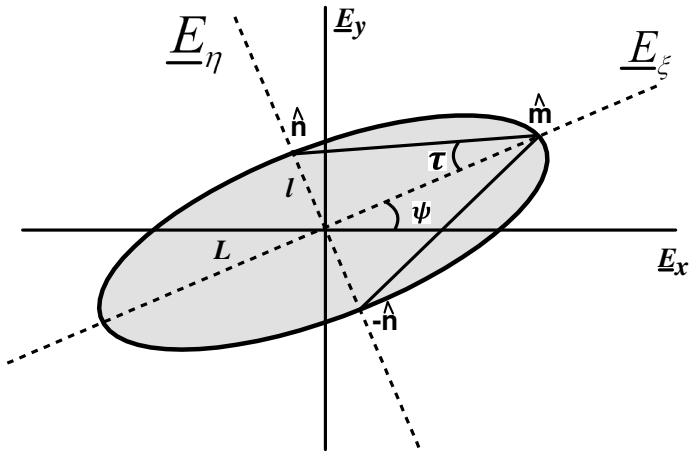

Figure 2.5. Polarization ellipse of a planar wave ($-\pi/2 \leq \psi \leq \pi/2$, and $-\pi/4 \leq \tau \leq \pi/4$).

where $|\cdot|$ is the amplitude of the electrical field, and φ_x, φ_y are the phases of this wave in $\hat{x}$ and $\hat{y}$ directions respectively. It could easily be shown (from Faraday's or Maxwell-Ampère laws) that magnetic and

electrical fields of any planar wave are orthogonal (see for instance [18]). Fundamentally, electrical fields could be used (solely) to describe the polarization configuration of the waves [15].

On a plane transverse to the propagation direction ($\hat{z}$ for example), a geometrical shape (Figure 2.5) is drawn with the tip of electric field: an ellipse [3, 7], which can be described by two angles and amplitude of the electrical field. Orientation $\psi \in [-\pi/2, \pi/2]$, and ellipticity $\tau \in [-\pi/4, \pi/4]$ angles represent the polarization signature effectively (see Table 2.1). On the other hand, two Deschamps parameters α and $\Delta\varphi$ could be exploited to describe the polarized waves [19]

$$\begin{cases} \Delta\varphi & = \varphi_x - \varphi_y, \\ tan\alpha & = \left(\frac{|\underline{E}_y|}{|\underline{E}_x|}\right), \end{cases} \tag{2.40}$$

Actually, they are related to each other via:

$$\begin{cases} tan2\psi & = tan2\alpha cos\Delta\varphi, \\ sin2\tau & = sin2\alpha sin\Delta\varphi, \end{cases} \tag{2.41}$$

As it is depicted in Figure 2.5, the electrical fields also could be represented in another coordinate system named $\hat{m}$, and $\hat{n}$:

$$\underline{E} = \underline{E}_\xi \hat{m} + \underline{E}_\eta \hat{n}, \tag{2.42}$$

where the vector $\begin{pmatrix} \underline{E}_\xi \\ \underline{E}_\eta \end{pmatrix}$ is known as Jones vector, a complex vector that is characterized by four degrees of freedom (see Table 2.1).

2.6.2 Stokes vectors

If the polarization characteristics of the EM wave change over time, the wave is known as non-stationary or partially polarized wave. A wave's coherency matrix is given by

$$\underline{\underline{T}} = \langle \underline{E}\ \underline{E}^\dagger \rangle = \begin{bmatrix} \langle \underline{E}_H \underline{E}_H^* \rangle & \langle \underline{E}_H \underline{E}_V^* \rangle \\ \langle \underline{E}_V \underline{E}_H^* \rangle & \langle \underline{E}_V \underline{E}_V^* \rangle \end{bmatrix}, \tag{2.43}$$

Table 2.1. Polarization ellipse and Jones vector parameters for some canonical polarization states.

Polarization state	**Orientation angle** ψ	**Ellipticity angle** τ	**Unit Jones Vector**
Linear horizontal	0	0	$\begin{pmatrix}1\\0\end{pmatrix}$
Linear vertical	$\pi/2$	0	$\begin{pmatrix}0\\1\end{pmatrix}$
Linear 45°	$\pi/4$	0	$\frac{1}{\sqrt{2}}\begin{pmatrix}1\\1\end{pmatrix}$
Linear 135°	$-\pi/4$	0	$\frac{1}{\sqrt{2}}\begin{pmatrix}1\\-1\end{pmatrix}$
Left circular	$[-\pi/2...\pi/2]$	$\pi/4$	$\frac{1}{\sqrt{2}}\begin{pmatrix}1\\j\end{pmatrix}$
Right circular	$[-\pi/2...\pi/2]$	$-\pi/4$	$\frac{1}{\sqrt{2}}\begin{pmatrix}1\\-j\end{pmatrix}$

where $*$ and $\dagger$, stand for complex conjugate and transpose of the vectors respectively, and $\langle\cdot\rangle$ stands for statistical averaging of the signal [20, 21]. $\underline{\underline{T}}$ is positive definite (or at least semi definite) and has Hermitian symmetry, i.e., its eigenvalues are both real and non-negative. The power of the EM wave is equal to the trace of the matrix $\underline{\underline{T}}$. The off-diagonal elements show the cross-correlation/polarization characteristics of the EM wave. If there is no correlation of any kind, i.e., $\langle \underline{E}_H \underline{E}_V^* \rangle = \langle \underline{E}_V \underline{E}_H^* \rangle$, the wave would be completely un-polarized [22, 23]. One complete un-polarized wave has a polarization radically changing over time, and from a statistical point of view, each component (H or V) has the same amount of power. From the other side, when $det(\underline{\underline{T}}) = 0$ the wave is completely polarized (which is also known as stationary case).

For describing the partially polarized wave, usually Stokes vector is used

$$\underline{\underline{Q}} = \begin{bmatrix} q_0 \\ q_1 \\ q_2 \\ q_3 \end{bmatrix} = \begin{bmatrix} |\underline{E}_H|^2 + |\underline{E}_V|^2 \\ |\underline{E}_H|^2 - |\underline{E}_V|^2 \\ 2|\underline{E}_H||\underline{E}_V| cos\Delta\varphi \\ 2|\underline{E}_H||\underline{E}_V| sin\Delta\varphi \end{bmatrix} = \begin{bmatrix} A^2 \\ A^2 cos2\tau cos2\psi \\ A^2 cos2\tau sin2\psi \\ A^2 sin2\psi \end{bmatrix}, \tag{2.44}$$

Since $q_0^2 = q_1^2 + q_2^2 + q_3^2$, the four Stokes parameters are not independent

(this relation is only valid for fully polarized waves). For fully describing the partial polarizations, the average of the fields must be considered

$$\underline{\underline{Q}} = \begin{bmatrix} q_0 \\ q_1 \\ q_2 \\ q_3 \end{bmatrix} = \begin{bmatrix} \langle \underline{E}_H \underline{E}_H^* \rangle + \langle \underline{E}_V \underline{E}_V^* \rangle \\ \langle \underline{E}_H \underline{E}_H^* \rangle - \langle \underline{E}_V \underline{E}_V^* \rangle \\ \langle \underline{E}_H \underline{E}_V^* \rangle + \langle \underline{E}_V \underline{E}_H^* \rangle \\ \langle \underline{E}_H \underline{E}_V^* \rangle + j \langle \underline{E}_V \underline{E}_H^* \rangle \end{bmatrix}, \tag{2.45}$$

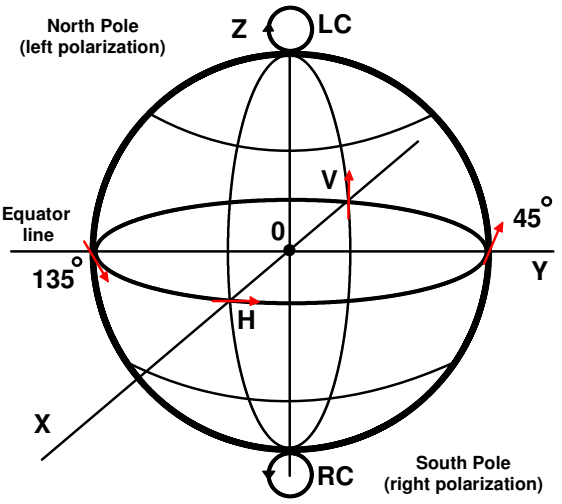

Figure 2.6. Poincaré sphere represents the location of all possible polarizations of waves.

With this notation $\begin{pmatrix} 1 & 1 & 0 & 0 \end{pmatrix}^\dagger$, and $\begin{pmatrix} 1 & -1 & 0 & 0 \end{pmatrix}^\dagger$ are horizontally and vertically polarized Stokes verctos respectively.

The degree of coherency (DoC) is defined as

$$DoC = \frac{|\langle \underline{E}_H \underline{E}_V^* \rangle|}{\sqrt{|\langle \underline{E}_H \underline{E}_H^* \rangle| + |\langle \underline{E}_V \underline{E}_V^* \rangle|}}, \tag{2.46}$$

And the degree of polarization (DoP)

$$DoP = \frac{\sqrt{q_1^2 + q_1^2 + q_3^2}}{q_0}, \tag{2.47}$$

For a completely un-polarized wave, $DoC = DoP = 0$, and for a completely polarized wave $DoC = DoP = 1$. For partial polarizations ($DoP < 1$) we get $q_0^2 \geq q_1^2 + q_2^2 + q_3^2$, i.e., the first element of Stokes vector stays intact, while the other three decrease significantly.

2.6.3 Poincaré Polarization Sphere

One of the best and most powerful ways to visualize the field polarization phenomenon is via the employment of the Poincaré sphere (Figure 2.6). In this kind of visualization, the two dimensional complex wave is transformed into the three dimensional real space coordinate system [23, 25]. The left and right hand polarized waves are represented on the upper and lower hemisphere respectively. The linear polarizations are located on the equator of the Poincaré sphere (see also Table 2.1). Completely polarized wave, i.e., $DoP = 1$, is mapped on the Poincaré sphere (i.e., on the surface), and partially polarized waves ($DoP < 1$), are mapped inside the Poincaré sphere.

2.6.4 Target-based Wave Decomposition

Sometimes it is easier to represent the decomposition of the targets with a vector rather than a matrix, because the algebraic manipulation is much easier [22, 25]. In the literature, two well known polarization vectors are utilized: Lexicographic, and Pauli basis [3, 7]. In principle the two representations are completely equivalent [26].

1. Lexicographic vector basis

$$\underline{\underline{\Psi}}_L = \left(2 \begin{bmatrix} 1 & 0 \\ 0 & 0 \end{bmatrix}, 2 \begin{bmatrix} 0 & 1 \\ 0 & 0 \end{bmatrix}, 2 \begin{bmatrix} 0 & 0 \\ 1 & 0 \end{bmatrix}, 2 \begin{bmatrix} 0 & 0 \\ 0 & 1 \end{bmatrix} \right), \tag{2.48}$$

   And the 4-D Lexicographic feature vector is

$$\underline{k}_L = \left(S_{hh}, S_{hv}, S_{vh}, S_{vv} \right)^{\dagger}, \tag{2.49}$$

   This representation is quite useful and makes the calculations much easier, and the elements simply represent the horizontal, vertical dipoles, and 45° oriented dihedrals [7].

2. Pauli vector basis

The Pauli basis (spin basis Pauli vector) for BSA (Back/Bi-static Scattering Alignment) coordinate systems is given by the following [22]

$$\underline{\underline{\Psi}}_P = \left(\sqrt{2} \begin{bmatrix} 1 & 0 \\ 0 & 1 \end{bmatrix}, \sqrt{2} \begin{bmatrix} 1 & 0 \\ 0 & -1 \end{bmatrix}, \sqrt{2} \begin{bmatrix} 0 & 1 \\ 1 & 0 \end{bmatrix}, \sqrt{2} \begin{bmatrix} 0 & -j \\ j & 0 \end{bmatrix} \right), \quad (2.50)$$

And the Pauli scattering vector is

$$\underline{k}_P = \big(S_{hh} + S_{vv}, S_{hh} - S_{vv}, S_{hv} + S_{vh}, j(S_{hv} - S_{vh})\big)^{\dagger}, \quad (2.51)$$

The Pauli scattering vector is directly associated with the physical targets properties. For instance, first element is representing isotropic scatterers like spheres and surfaces (e.g. bare/surface soils). The second element is related to the double bounce (mainly) scattering mechanism, and the last two are representing a 45° dihedral, and a non reciprocal target respectively [3, 17]. The Pauli scattering vector could be used to decompose observed targets coherently.

In SAR remote sensing, these vectors are a bit different. The reason is that the SAR systems utilize mono-static or backscattering based arrangements, i.e., observed targets are mainly reciprocal. In such a case, we usually put $S_{hv} = S_{vh}$, and the Lexicographic and the Pauli scattering vectors will be

$$\begin{cases} \underline{k}_L &= \big(S_{hh}, \sqrt{2}S_{hv}, S_{vv}\big)^{\dagger}, \\ \underline{k}_P &= 1/\sqrt{2}\big(S_{hh} + S_{vv}, S_{hh} - S_{vv}, 2S_{hv}\big)^{\dagger}, \end{cases} \quad (2.52)$$

Two Pauli and Lexicographic scattering vectors are related to each other via

$$\begin{cases} \underline{k}_L &= \underline{\underline{D}}_3^{-1} \underline{k}_P, \\ \underline{k}_P &= \underline{\underline{D}}_3 \underline{k}_L, \end{cases} \quad (2.53)$$

where

$$\underline{\underline{D}}_3 = \frac{1}{\sqrt{2}} \begin{bmatrix} 1 & 0 & 1 \\ 1 & 0 & -1 \\ 0 & \sqrt{2} & 0 \end{bmatrix}, \tag{2.54}$$

Span of the basic vectors is given by $Span = |S_{hh}|^2 + |S_{hv}|^2 + |S_{vh}|^2 + |S_{vv}|^2$. And for the backscatter case, it reads: $Span = |S_{hh}|^2 + 2|S_{hv}|^2 + |S_{vv}|^2$.

2.6.5 Coherence and covariance matrices

For the mono-static case and in the case of reciprocity, the covariance matrix in Lexicographic vector base is given by:

$$\underline{\underline{C}} = \langle \underline{k}_L \underline{k}_L^* \rangle = \begin{bmatrix} \langle |S_{HH}|^2 \rangle & \sqrt{2}\langle S_{HH} S_{HV}^* \rangle & \langle S_{HH} S_{VV}^* \rangle \\ \sqrt{2}\langle S_{HV} S_{HH}^* \rangle & 2\langle |S_{HV}|^2 \rangle & \sqrt{2}\langle S_{HV} S_{HH}^* \rangle \\ \langle S_{VV} S_{HH}^* \rangle & \sqrt{2}\langle S_{VV} S_{HV}^* \rangle & \langle |S_{VV}|^2 \rangle \end{bmatrix}, \tag{2.55}$$

And the coherency matrix in Pauli scattering vector base reads (see [7])

$$\underline{\underline{T}} = \langle \underline{k}_P \underline{k}_P^* \rangle, \tag{2.56}$$

Fundamentally we can express the covariance and coherence matrices in any bases that could be represented in the form of

$$\underline{k}_X = \big(k_1, k_2, k_3\big)^\dagger, \tag{2.57}$$

The coherence and the covariance matrices are related to each other via

$$\underline{\underline{T}} = \underline{\underline{U}}\, \underline{\underline{C}}\, \underline{\underline{U}}^{-1}, \tag{2.58}$$

where $\underline{\underline{U}}_3$ is the special unitary transformation matrix [7].

The trace of the covariance matrix $\underline{\underline{C}}$ represents the total power or span of the scattering matrix

$$TotalPower = trace(\underline{\underline{C}}) = span(S), \tag{2.59}$$

Off diagonal terms of $\underline{\underline{C}}$ are the cross-correlations among the scattering vectors, which give us information about the degree of polarization of the scatterers.

2.6.6 H-α decomposition

As explained in the last section, the coherency matrix can be represented by equation (2.58). Coherency matrix is an hermitian and non negative matrix with three eigenvalues and eigenvectors:

$$\underline{\underline{T}}\,\underline{\underline{U}} = \underline{\underline{U}}\,\underline{\underline{\Lambda}}, \tag{2.60}$$

where $\underline{\underline{U}}$ is the eigenvectors matrix, and $\underline{\underline{\Lambda}}$ is a diagonal matrix which is filled with the eigenvalues of matrix $\underline{\underline{T}}$

$$\underline{\underline{T}} = \underline{\underline{U}}\,\underline{\underline{\Lambda}}\,\underline{\underline{U}}^{*\dagger}, \tag{2.61}$$

These eigenvectors ($\underline{u}_i s$) have five degrees of freedom

$$\underline{u}_i = \left(cos\alpha_i e^{j\varphi_{1i}}, cos\beta_i sin\alpha_i e^{j\varphi_{2i}}, sin\beta_i sin\alpha_i e^{j\varphi_{3i}}\right), \tag{2.62}$$

where φs are the phase terms, βs represent the physical rotation of the scatterers around the Line Of Sight (LOS) of the sensor, and αs are the internal degrees of freedom of the targets, i.e., type of the scattering mechanism. Moreover, due to the orthogonality, the coherency matrix can be expressed as

$$\underline{\underline{T}}_s = \sum_{i=1}^{3} \lambda_i \underline{u}_i \cdot \underline{u}_i^* = \sum_{i=1}^{3} \lambda_i \underline{\underline{T}}_i, \tag{2.63}$$

$\underline{\underline{T}}_i$ is a rank 1 coherency matrix that describes the scattering properties of a single target.

We recall that the entropy H is related to the eigenvalues of the coherency matrix and mainly measures the "degree of randomness" of the scattering process:

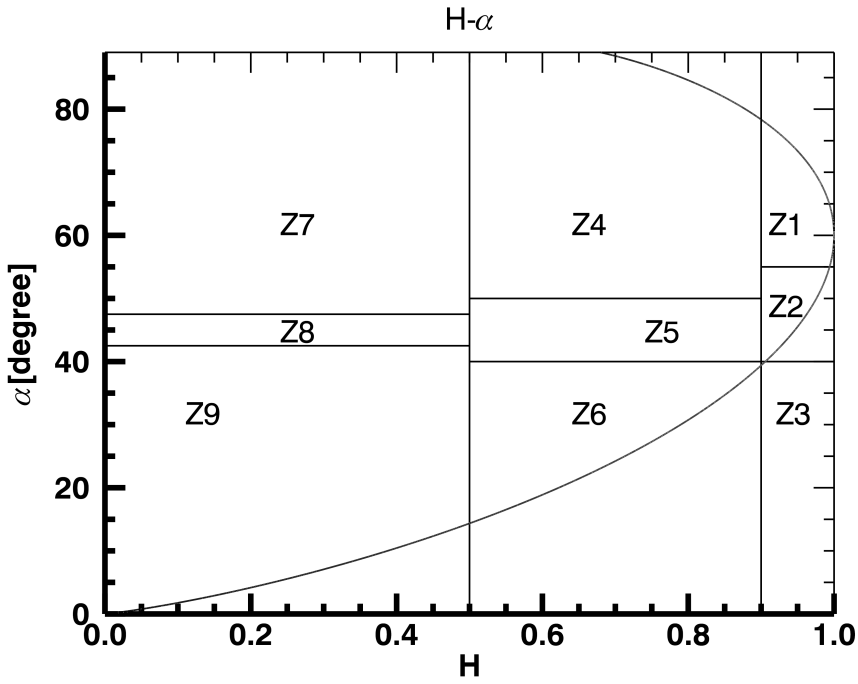

Figure 2.7. $H - \alpha$ unsupervised classification mechanism, with the corresponding scattering regions ($Z1 - Z9$).

$$H = -\sum_{i=1}^{3} P_i log_3 P_i, \tag{2.64}$$

where $P_i = \lambda_i / \sum_{i=1}^{3} \lambda_i$.

This factor also can be used as a degree of confusion associated with each scattering mechanism, i.e., the larger the entropy, the greater is the uncertainty associated with the scattering mechanism. Furthermore, the mean scattering angle α is related to the eigenvalues and eigenvectors of the coherency matrix, with maximum likelihood of

$$\alpha = \sum_{i=1}^{3} P_i \alpha_i, \tag{2.65}$$

with P_i being the probablity of each α_i.

Meanwhile, entropy H and α (which is known as $H - \alpha$) can be used as a hard (unsupervised) classifier for different scattering mechanisms. As Figure 2.7 shows, 9 scattering regions can be classified accordingly:

- Z9- Low entropy surface scattering: surfaces such as water at L and P-bands, sea ice at L-band, and very smooth land surfaces;
- Z8- Low entropy dipole scatting mechanism: corresponds to isolated dipoles, vegetation with strong correlated orientation of anisotropic scattering elements;
- Z7- Low entropy multiple scattering: low entropy double- or even bounce scattering mechanism, such as isolated dielectric and metallic dihedral scatterers;
- Z6- Medium entropy surface scattering: entropy increases due to change in the surfaces roughness and canopy propagation effects;
- Z5- Medium entropy canopy scattering: moderate entropy but with a dominate dipole type scattering mechanism. Central statistical distribution of the orientation angles, cause the entropy increases. Scattering from vegetated surfaces, with anisotropic scatterers and moderate correlation of scatterer orientations fall in this zone;
- Z4- Medium entropy and multiple scattering: This zone includes the dihedral scatterers with moderate entropy. For instance in forestry, double bounce mechanism occurs at lower bands following propagation through a canopy. Canopy tends to increase the entropy of the scattering process. A similar mechanism is also evident in urban areas;
- Z3- High entropy surface scattering: This region is not very realistic in nature i.e., it is not possible to distinguish surface scattering with entropy;

- Z2- High entropy vegetation scattering: scattering from forest canopies, and any other kinds of surface vegetation with randomly high anisotropic elements. No polarization dependence is considered in this class;

- Z1- High entropy vegetation scattering: double bounce mechanisms could be distinguished in this region despite the high amount of entropy. The typical examples are forestry and vegetation with well-developed branches and crown structures;

Note that the regions $Z1 - Z9$ are not equally populated and the real targets lie within theoretical bounds that represent the minimum and maximum allowable values of α (which is a function of entropy itself).

Bibliography

[1] Jackson, J. D. (1999). *Classical Electrodynamics.* Third edition. Wiley.

[2] Cloude, S. R. (1995a). *An Introduction to Electromagnetic Wave Propagation and Antennas.* UCL Press.

[3] Cloude SR (2009) *Polarisation. applications in remote sensing.* Oxford University Press, Oxford, 978-0-19-956973-1.

[4] Chen, H. C. (1985). *Theory of Electromagnetic Waves: a Coordinate-Free Approach.* McGraw-Hill.

[5] G. Franceschetti, A. Iodice, M. Migliaccio, and D. Riccio, "Scattering from natural rough surfaces modelled by fractional Brownian motion twodimensional processes," *IEEE Transactions on Geoscience and Remote Sensing*, vol.47, no. 9, pp. 14051415, Sep. 1999.

[6] G. Franceschetti, A. Iodice, and D. Riccio, "Fractal models for scattering from natural surfaces," *Scattering,* R. Pike and P. Sabatier, Eds. London, U.K.: Academic, 2001, pp. 467485.

[7] Lee JS, Pottier E (2009) *Polarimetric radar imaging: from basics to applications.* CRC Press, Boca Raton.

[8] G. Franceschetti, D. Riccio, *Scattering, Natural Surfaces and Fractals,* Academic Press, Burlington, 2007.

[9] Tsang, L., and J. A. Kong. 2001. *Scattering of Electromagnetic Waves*, Vol.3: Advanced Topics, New York: Wiley Inter science.

[10] S. Perna, A. Iodice, "On the Use of Series Expansions for Kirchhoff Diffractals", *IEEE Transactions on Antennas and Propagation,* vol.59, no. 2, pp. 595-610 February, 2011.

[11] Fung, A.K. (1994) *Microwave Scattering and Emission Models and Their Applications,* Artech House, Norwood, MA.

[12] T. D. Wu, K. S. Chen, J. Shi, A. K. Fung, "A Transition Model for the Reflection Coefficient in Surface Scattering", *IEEE Transactions on Geoscience and Remote Sensing,* vol.39, no. 9, pp. 2040-2050, September 2001.

[13] Tsang, L., J. A. Kong, and K. H. Ding. 2000, *Scattering of Electromagnetic Waves, Vol.1: Theory and Applications,* New York: Wiley Inter science.

[14] Huang, X. and Jin, Y.Q. (1995) Scattering and emission from two-scale randomly rough sea surface with foam scatterers. *IEE Proceedings HMicrowaves, Antennas, and Propagation,* 142 (2), 109114. Kong, J. A. (1985). Electromagnetic Wave Theory. Wiley.

[15] Goldstein DH, Collett E (2003) *Polarized light.* CRC, Boca Raton.

[16] Mott H (2007) *Remote sensing with polarimetric radar.* Wiley, Hoboken.

[17] Zebker HA, Van Zyl JJ (1991) Imaging radar polarimetry: a review. *Proc IEEE* 79:15831606.

[18] Rothwell EJ, Cloud MJ (2001) *Electromagnetics.* CRC Press, Boca Raton.

[19] Deschamps GA (1951) Geometrical representation of the polarization of a plane electromagnetic wave. *Proc IRE* 39:540544.

[20] Jones R (1941) A new calculus for the treatment of optical systems. I. description and discussion; II. Proof of the three general equivalence theorems; III. The Stokes theory of optical activity. *Journal Opt Soc Am* 31:488503.

[21] Wolf E (2003) Unified theory of coherence and polarization of random electromagnetic beams. *Phys Letters* 312:263267.

[22] Cloude SR (1987) *Polarimetry: the characterization of polarization effects in EM scattering.* Electronics Engineering Department. York, University of York.

[23] Lneburg E (1995) Principles of radar polarimetry. *Proc IEICE Trans Electron Theory* E78-C: 13391345.

[24] Bebbington DH (1992) Target vectors: Spinorial concepts. *Proceedings of the 2nd international workshop on radar polarimetry,* IRESTE, Nantes, France, pp 2636.

[25] Ulaby FT, Elachi C (1990) *Radar polarimetry for geo-science applications.* Artech House, Norwood.

[26] Strang G (1988) *Linear algebra and its applications, 3rd edition.* Thomson Learning, New York.

This page intentionally left blank.

Chapter 3

Synthetic Aperture Radar (SAR)

3.1 Radar concepts and history

The word Radar is used to refer to a specific band of EM waves and as well as an engineering system (see, e.g., [1, 2]). An engineering radar system has three primary functionalities:

1. It transmits microwave signals towards the targets through the antenna/s.

2. It receives the portion of the transmitted energy that gets backscattered from the targets, in the ratio dictated by the radar cross sections.

3. It quantifies the strength (detection) and the time delay (ranging) of the backscattered signal, to measure the needed quantities.

In the radar system, antenna is a device that couples energy between the outgoing and the transmission lines [3]. In remote sensing, antennas can be dish like, spiral, or a series of antennas to transmit and/or receive the backscattered EM signals (see for instance [4]). Transmitting antennas take Radio-Frequency (RF) energy from the transmitter and convert it into a form of radar wave with a desired shape that further will illuminate the target surfaces. On the other hand, the receiving antenna/s, acquire

the EM energy from a specific direction, and then guide it to the receiver unit through the wave guides. In most radar systems, the same antenna/s (known as mono-static radar) transmit and receive the EM energy, with a duplexer to be used to switch the antennas between the transmitting and receiving missions. When the same antenna does not function as transmitter and receiver it is called a bi-static radar system. Since the received signals are weak and hard to analyse, the amplification aid needs to perform proper signal processing for better diagnostics [1].

The antenna's gain is a non-dimensional parameter, used to describe the radiation intensity produced by an antenna in a specific direction, in comparison with an isotropic antenna with the same input power [5].

Radar systems are used widely nowadays in engineering, geophysics, geology, imaging, police velocity meters, civil engineering, and for environmental purposes [1]. Some of the main contributions of radar imagery are in the following areas: ice and glacier monitoring (see, e.g., [6, 7, 8]), slick detection [9], ocean waves [10, 11], the Earth [12, 13], soil moisture [14], terrain deformation [15, 16], weather forecasting/atmospheric monitoring [17], and geo-hazard mapping [18, 19, 20].

Historically, the earliest attempt at studying reflection of radio frequency waves from materials/metals is attributed to Heinrich Roudolf Hertz, who in 1886 used 450 MHz spark-gap transmitter and receiver to examine Maxwell's equations. In 1903 a German engineer Christian Hulsmeyer developed a radar (continuous wave) ship detector system for the German Navy, which was considered a weak tool because of limited applications. The acronym RADAR (for "RAdio Detection And Ranging") was coined during World War II (1940s), and prior to that, had not been listed as a word in many dictionaries. Radar was developed to replace highly attenuated light waves which suffer significantly from atmospheric effects. Thus, radar is an all-day, all-weather conditions tool, which can work even before the target becomes optically visible. As radar sends its own signal, it is classified as an active rather than a passive device. In this case, users can clock the time, and measure the traveling time of the energy that has traveled from antenna to target and back from target to antenna. Radars can be classified into Continuous Wave (CW), and pulse radars (see for instance [21]). In CW, the radar emits ontinuous system of energy, and mixes the received signal with a sample of emitted signal to

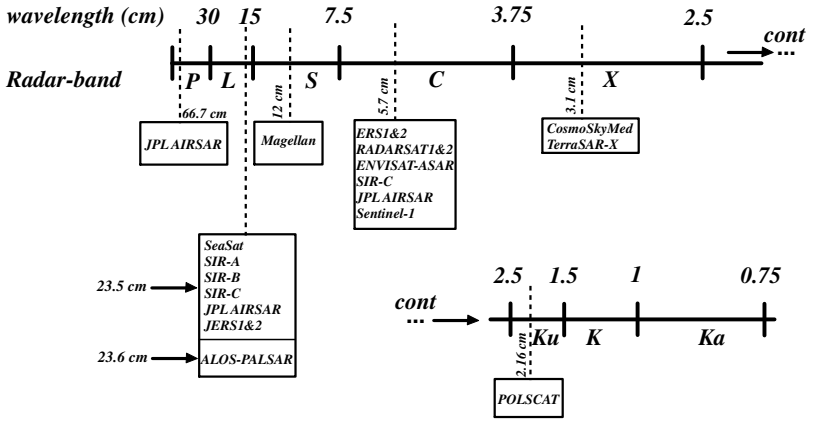

Figure 3.1. Some of the main well-known active or deactivated radar satellite sensors, with the wavelength and radar-band of the named operational domains.

retrieve information about the targets. These radar systems are able to prove the existence of the targets, but unable to find the range/distance information. One popular example of CW radars is the police's radar devices, a kind of Moving Target Indicator (MTI). In pulse radar, a relatively short burst of energy (Radio-Frequency, RF) is emitted, with the system being in listening mode for getting the echo. In 1922, the first continuous radar made by Taylor cooperating [22]. The first pulse radar in 60 MHz, was built by the Naval Research Laboratory (NRL) in 1934. During the 1930s, Britain and Germany were cooperating on radar systems for tracing of ships, and airplanes. The first imaging radar from Earth's surface was built during WWII. This radar system was capable of a 360° rotation of antenna, but despite the elegant configurations, some notable distortions in the imaging modes were reported. In the early 1950s, Side Looking Radars (SLR) were developed to resolve the ambiguities attached to the surface's objects. At the beginning SLR systems were solely designed for military proposes, but gradually (in the midd 1960s) attention turned to the civil and environmental (none military) benefits too. In the SLR

scanning methodologies, the images have low resolution qualities in the azimuth directions. As a rule of thumb, the smaller the bandwidth of the radar system signals, the higher the resolution of imageries in the azimuth direction. To reach the smaller bandwidth in the radar systems, one should choose between use of bigger antenna or smaller radar wave configuration. Use of bigger antenna size is practically impossible for airplanes and satellites. On the other hand, very small EM waves (small λs) are subjected to attenuations by atmosphere and clouds. So, for having high resolution radar imageries, signal processing techniques must be employed. For instance, in Synthetic Aperture Radar (SAR) missions, with the forward movements of the radar sensors, a huge antenna size is synthetically produced, without the need to decrease the EM wavelength, or increase the physical size of the antenna dramatically.

Figure 3.2. A radar scan from the shuttle in band L (SIR-A) of the African Sahara, in comparison with an optical image from Landsat ETM+ (image courtesy of JPL).

In 1951, Doppler beam-sharpening radar sensors was invented by Carl A.Willy at Goodyear corporations. In 1952 the first airplane equipped

with a SAR sensor (working in the 930 MHz) was flown in the sky over Washington DC. Until the 1960s, the Goodyear aircraft corporation attained to enormous achievements in SAR technologies. During the same period, USSR, France, and England, also devoted themselves to SAR based systems.

SeaSat radar satellite, the very first SAR based satellite that was launched in June 1978 for ocean studies [23]. Then Space shuttle of NASA (SIR-C/X SAR) was equipped with a SAR system in the 1990s, which gave us a treasury of topographic imageries of 80% of the Earth, from radar based instruments [24]. In July 1991, with launch of the ERS-1, European Remote Sensing Satellite by the European Space Agency (ESA), a new generation of special satellites dedicated to InSAR technology, was launched one by one from countries like Japan [25], Canada, Germany, and Italy.

Radar imaging missions have not been limited only to our planet, the Earth. For instance, the Magellan satellite mapped 98% of the planet Venus from 1990 to 1992 with imageries in resolution of 150 meters.

Various radar sensors are currently operational with different revisiting time and pixel resolutions all around the Earth [26, 27]. These radar satellites are gathering data at roughly $800km$ above the Earth's surface using C, X, and L radar bands. Figure 3.1, lists some of the main well known sensors with the radar frequency and wavelength of the named operational domains. As mentioned earlier, radar imaging systems provide their own energy sources, and could operate both during the day and/or night and through cloud cover or rainy weather. Radar remote sensing uses the microwave portion (actually very narrow) of the electromagnetic spectrum. It covers a frequency from 0.3 GHz to 300 GHz, or in wavelength terms, from 1 mm to 1 m. In Radar systems, the wavelengths are characterized by symbols like: X, C, L, etc, to show the wavelength/frequency of the transmitted signal (Figure 3.1). For instance CosmoSkyMed or TerraSAR-X uses the X band radar, which means the transmitted electromagnetic signal has a 3.1 cm wavelength. The newest imaging satellite Santinel-1 uses the C-band radar wavelength. Because of wide surface coverage (e.g. 100×100 for ERS 1&2, and ENVISAT-ASAR sensors), frequent visiting of the sensors, e.g., 12 hours for CosmoSkyMed sensors in crisis times [28], and more recently very high resolution sensors like TerraSAR-X and

CosmoSkyMed (sub-meter resolution imageries), InSAR is going to play a very important role in engineering, civil, and environmental science in the near future. After the launch of the Sentinel-1 in spring 2014, a family of sentinel satellites will be in orbit, highlighting a new upcoming era of radar satellites.

In the upcoming sections, InSAR concepts/fundamentals, like producing of the interferograms, coherency, image geo-referencing, etc., will be addressed concisely.

3.2 Radar wave penetration in various environments

As explained earlier, radar waves are not influenced significantly by clouds and/or atmosphere (but total radar phase should be corrected/compensated accordingly), except for conditions like very heavy rain and tornados, etc. Radar waves could be scattered volumetrically from targets, because of bigger wavelength compared to optical based monitoring sensors/devices. This property helps the radar waves to penetrate inside the target, which is a function of many different factors. For instance in Figure 3.2, a radar scan from shuttle in L-band (SIR-A) of the African Sahara is compared with an optical image from Landsat ETM+. As this figure shows, the radar wave has the ability to penetrate beneath Earth's surface up to certain depths. The penetration depth is a function of wavelength, humidity, and the dielectric properties of the environments. As a rule of thumb, the depth of penetration (or skin depth) in an environment is given by $\frac{\lambda\sqrt{\epsilon_r^{'}}}{2\pi\epsilon_r^{''}}$, where $\epsilon_r^{'}$, and $\epsilon_r^{''}$ are related to the dielectric (relative permittivity, i.e., $\epsilon_r = \epsilon_r^{'} - j\epsilon_r^{''}$) properties of the environment (another similar formula is $\frac{1}{\sqrt{\pi f \mu \sigma}}$). For instance in the Sahara example (where humidity is very low), penetration depth in the subsoil material is approximately estimated at 1 or 2 meters.

Given the rule, the higher the wave length, the deeper the penetration of the radar wave, the P and L band scanning of the radar waves will give information from greater depths beneath Earth's surface than the C and X band scanning. Similar evaluations for penetration in vegetation areas also exist: P and L-band radar could reach the ground in the vegetated

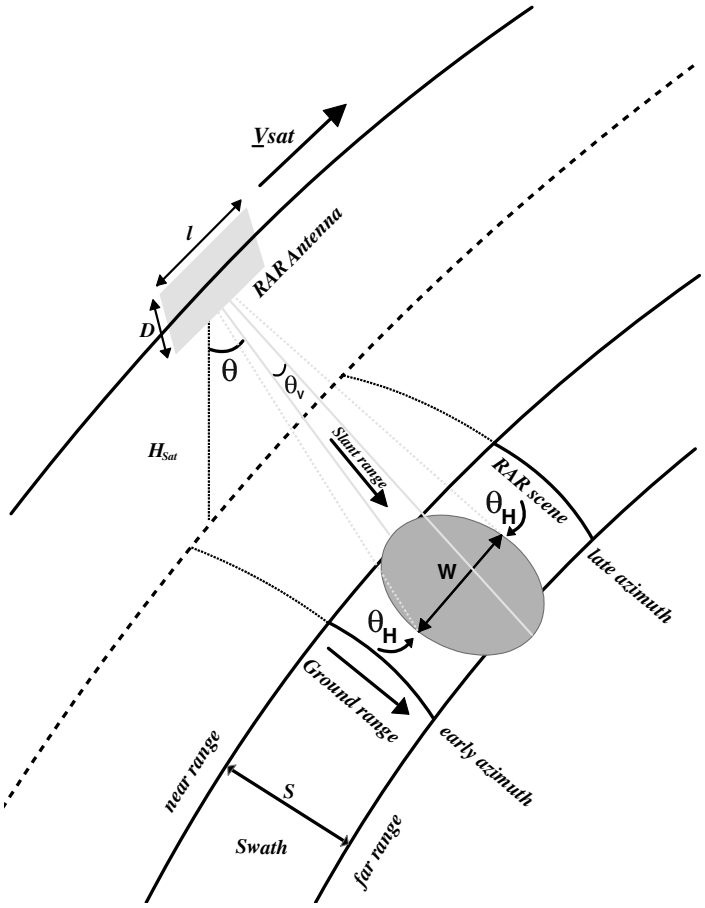

Figure 3.3. Radar system arrangement and technique for developing Real Aperture Radar (RAR) configuration has been depicted in this figure.

areas, while at the same time, X-band waves are mainly scattered by the leaves and upper parts of the vegetated area.

3.3 How Real Aperture Radar (RAR) works

In Figure 3.3 the geometrical configuration of the Real Aperture Radar (RAR) is presented. An antenna with length of l, and width of D illu-

minates the ground in horizontal and vertical beam widths at the rate of $\theta_H = \alpha\frac{\lambda}{l}$, $\theta_V = \alpha\frac{\lambda}{D}$ respectively, where $0.9 < \alpha < 1.4$, and λ is the wavelength of the transmitted EM wave. In Figure 3.3, the dashed area is known as the radar footprint, and the ground swath is given by $S = \frac{\lambda R}{D \cdot cos\theta}$, where θ is the look angle, and R is the slant range. The EM wave has the pulse length of τ_p and Pulse Repetition Frequency of PRF. The range R is related to the two way travel time of t as: $R = Ct/2$. As a rule of thumb with $C = 300,000\ km/s$ (speed of light): $R[km] \equiv 0.15t[\mu s]$ and/or $150m \equiv 1\mu s$. If we consider a pulse length of $37\mu s$ (see Figure 3.4), which we have for C-band radar systems like ENVISAT-ASAR, the distance for moving a pulse during this time is $c\tau[m] \equiv 11.100[m]$, and two objects could be segregated via this pulse if their distance would be less than $0.5c\tau[m] = 5.55[km]$, which demonstrates the resolution of the RAR system radars. 0.5 is considered because of the two-way travel time arrangements. This resolution is independent of the sensor elevation, but is a function of pulse length of τ_p. The ground resolution of the RAR arrangement is just division of $0.5c\tau$ to $sin\theta$, i.e., $\delta_r = \frac{c\tau}{2sin\theta}$.

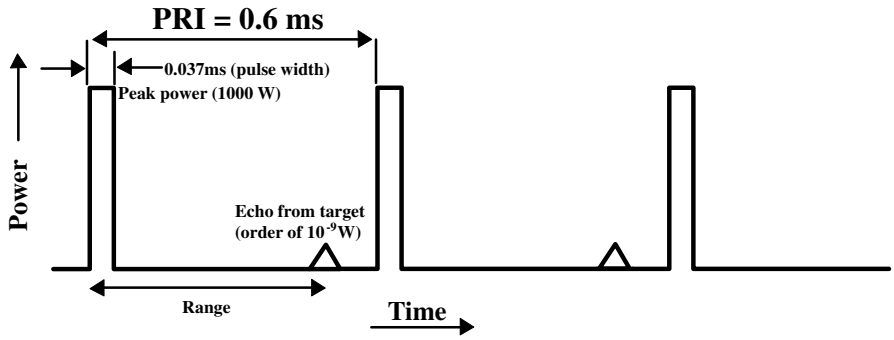

Figure 3.4. Generated pulse in ENVISAT-ASAR sensor.

The fundamentals of calculation of the image resolution in the azimuth direction for a RAR system, is given in Figure 3.5. As this this figure depicts, $\theta_H = \frac{\lambda}{l}$ and the resolution in the azimuth direction is $\delta_a = R\frac{\lambda}{l}$.

As an example, for a satellite with antenna length (physical size) of $l = 10m$, working in C-band, and orbiting at the height of 800 km above Earth, azimuth resolution will be 4.48 km, in other words, objects less

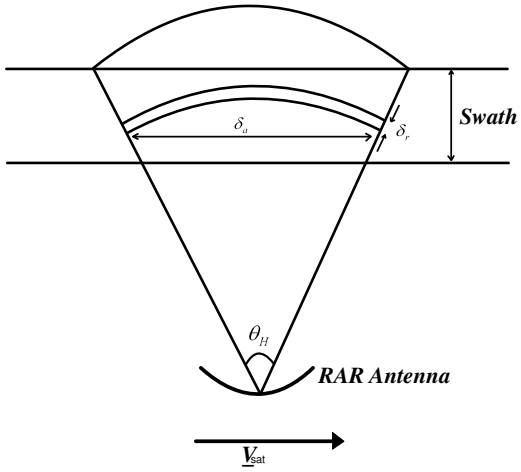

Figure 3.5. Radar resolutions for azimuth and range directions in RAR systems.

than 4.48 km, will not be detected with the RAR method. Azimuth resolution in the RAR systems is related to the length of antenna and distance of satellite from targets. For reaching high resolution imageries, use of big antenna is obligatory, something that is not usually possible. Consequently, engineers have invented another kind of satellite that with signal processing, and forward movement techniques, enables very high resolution radar imageries. In these techniques, with signal processing and Doppler effects, a very long radar antenna is synthetically created; with synthetic antenna size of around 5 km.

3.4 Synthetic Aperture Radar (SAR)

Synthetic Aperture Radar (SAR) is classified under the side looking radars, which mounted on an aircraft or on a satellite, are capable of scanning the earth's surface in different bandwidths.

Basic operation of the SARs in satellite remote sensing is also described with side looking radar terminology. Signal pulses are sent to the Earth's surface perpendicular to the orbit direction, and backscattered signals

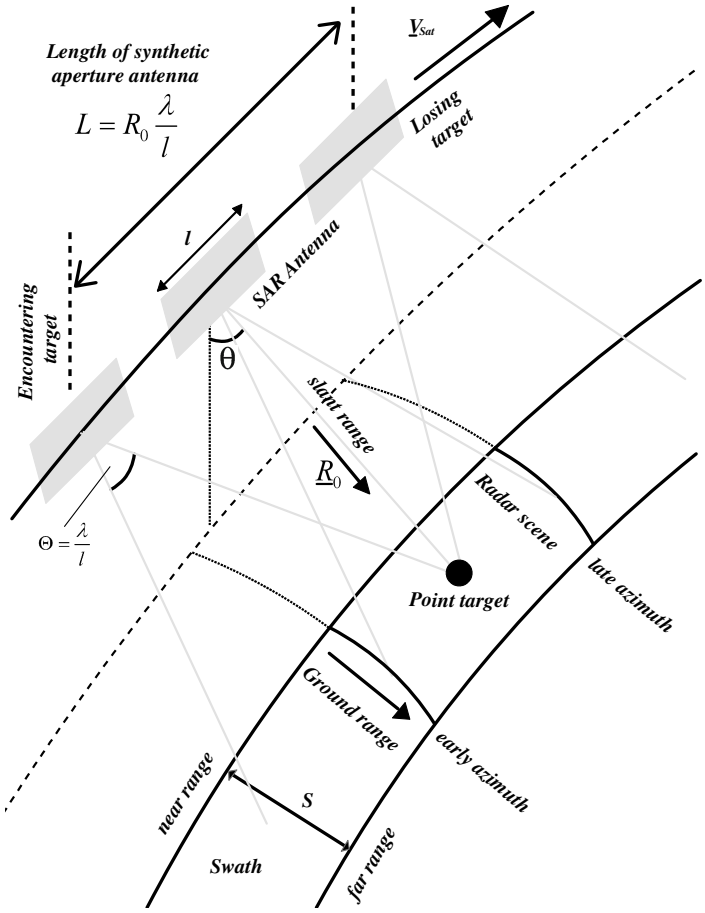

Figure 3.6. Synthetic Aperture Radar (SAR) arrangement.

are collected from scatterers. Frequency information (phase) is the main factor in InSAR (Interferometric SAR) radar scanning. In what is known as coherent radar, phase and amplitude of backscattered signals collected for later processing should be stable within the period of the sending and receiving of the signal.

The launch of ERS-1 (European Remote Sensing Satellite) by European Space Agency (ESA) in July 1991, initiated the new era of Interferometric SAR (InSAR) with which we are now acquainted. This

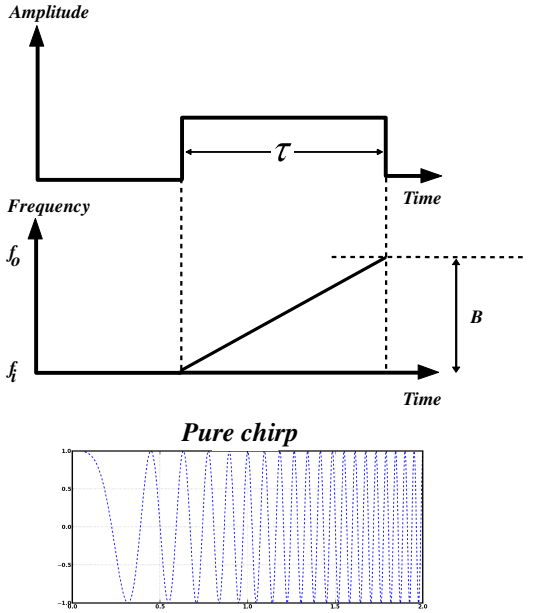

Figure 3.7. Signal compression fundamentals for generating chirps in SAR.

satellite was initially planned for a five year operational life, but was operated until March 2000. ERS-2 the-sister of ERS-1 was launched in April 1995 and was capable of working in so called tandem-mode, which means operating of two satellites together. ERS-2 followed ERS-1 in the same orbit with a temporal spacing of 30 minutes delay. Other important SAR sensors are: JERS (Japanese Earth Resources Satellite) - SIR-C/X - RADARSAT1&2 -ENVISAT (launched in 2002) - Shuttle radar Topography Mission (SRTM)- TerraSAR-X (Germany) and Cosmo-SkyMed (Italy). Besides, since 2014, the new generation Sentinel family satellites initiating the new era of In/SAR satellites. ALOS-2 satellite is also launched at the 2014, which is designed for interferometric and fully polarimetric radar scanning.

3.5 How to make synthetic aperture

The forward movement of the radar antenna in specific trajectories facilitates attaing very high resolution radar imagery with signal processing, and achievement of a synthetic antenna several kilometers in size. In this technique as presented in Figure 3.6, the antenna with a physical length of l is moving with speed of $\underline{V}$, and sending the radar EM waves toward the targets. Swath is the distance between near range and far range of the radar scan, and the radar image consists of these limitations, and the distance between early and late azimuth, similar to what we have in RAR systems. The specific target (here assumed to be a point target) on the ground with distance R_0 from antenna (known as slant range), is illuminated with the EM beam, at the rate of $\theta = \frac{\lambda}{l}$. This target has been seen by the radar system from just encountering the target to losing the target (see the Figure 3.6). This arrangement is known as synthetic antenna making, and the synthetic antenna size measures out to $L = R_0 \frac{\lambda}{l}$. As an example, for ENVISAT-ASAR and ERS1&2 satellites which were operating in the wave length of $C = 5.6cm$, and $R_0 \approx 800km$, the synthetic antenna measured out to $L \approx 4.48km$, with physical antenna size of $l = 10m$. The resolution of SAR images in the azimuth direction is given by $\delta_a = l/2$, which in our example would be $\delta_a = 5m$.

Now, the question is how much the range direction resolution in SAR systems would be? As explained in the last sections, radar resolution in the range direction is $\delta_r = \frac{c\tau}{2} = \frac{c}{2B}$, where B is the bandwidth to pass the pulse without significant alteration. If B could be maximized, the radar image resolutions could be increased in the slant range direction. In signal processing, B is defined as the difference between the maximum and minimum frequencies of chirp signals, which is the basis of pulse compression. A popular chirp pulse waveform is given by

$$\psi(t) = exp\left[j\left(\omega t + \frac{\alpha t^2}{2}\right)\right] rect\left[\frac{t}{\tau}\right], \tag{3.1}$$

where $rect\left[\frac{t}{\tau}\right]$ is the standard rectangular window function pulse,(i.e., $rect[t/\tau] = 1$ if $|t| \leq \tau/2$, otherwise $rect[t/\tau] = 0$) of duration τ, $\omega = 2\pi f$ is the angular frequency with f the carrier frequency, and α is the chirp rate related to the pulse bandwidth by $\alpha\tau \approx 2\pi\Delta f$.

This procedure is depicted in Figure 3.7. As this figure shows during the pulse length of τ, the frequency of the signal increases from f_i to f_o. This trick will decrease the value of the δ_r, which is correspondingly equal to the increasing of the image resolution in the range direction. For instance for a radar in C band, which is used by ENVISAT-ASAR satellite, the central frequency is 5300 MHz, and the $\tau_p = 37\mu s$, with signal compression technique, B would be reached to $15.5MHz$ during the τ_p pulses. In this case, the resolution in the range direction will be:

$$\begin{cases} \tau_p[s] = \frac{1}{B} = \frac{1}{15.5} MHz = 64 \times 10^{-9}[s], \\ \delta_r = 0.5c\tau_p[m] = 9.6[m], \end{cases} \tag{3.2}$$

Which compared to what is obtained in the RAR system ($i.e., \delta_r = 4.47[km]$), is a remarkable enhancement.

3.6 Doppler effects and SLR arrangements

Figure 3.8 shows the fundamental necessities for understanding Doppler effect and SLR arrangements in SAR data configurations. Imagine that a sensor (satellite or airplane) is moving with speed of V_{sat}, and for the sake of simplicity, the sensor movement has solely x direction component, i.e., $\underline{V} = V\hat{x}$. The EM pulses have been sent one by one on the right hand side of the sensor (see Figure 3.8). Any point in the radar image (i.e., pixels), has the coordinate (x_p, y_p, z_p), and the antenna is at the coordinate $(x_s, 0, 0)$. The slant range vector at any time will be $\underline{R} = (x_p - x_s)\hat{x} + y_p\hat{y} + z_p\hat{z}$. The transmitted EM wave has the central frequency of f_c, and the radial velocity of the sensor with respect to the ground will be:

$$v_r[m/s] = -\frac{\underline{V} \cdot \underline{R}}{|\underline{R}|} = -V\frac{x_p - x_s}{|\underline{R}|}, \tag{3.3}$$

And the observed Doppler frequency will be:

$$f_d[Hz] = -\frac{2v_r}{\lambda} = 2V\frac{x_p - x_s}{|\underline{R}|\lambda}, \tag{3.4}$$

For $x_s = 0$, the Doppler frequency will be:

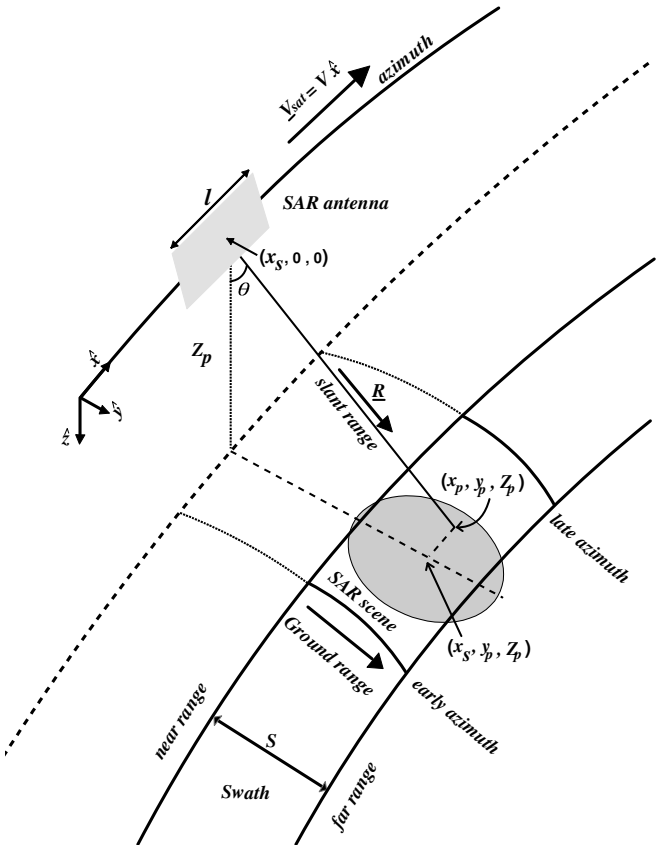

Figure 3.8. Sensor configuration, for Doppler effect measurements in SAR arrangement.

$$f_d[Hz] = -2V\frac{x_p}{R_0\lambda}, \tag{3.5}$$

Equation (3.5) could be written in the form of:

$$\left[\left(\frac{2V}{\lambda f_d}\right)^2 - 1\right]x_p^2 - y_p^2 - z_p^2 = 0, \tag{3.6}$$

where $R_0^2 = x_p^2 + y_p^2 + z_p^2$. Equation (3.6) shows a hyperbola on the $Z = const$ plane, since $\left(\frac{2V}{\lambda f_d}\right)^2 - 1 > 0$, $-z_p^2 \neq 0$, and $-1 < 0$. Furthermore,

$\underline{R}_{|x_s=0}$ shows the location of a circle with $rang = const.$ This circle and the Doppler hyperbola are depicted in Figure 3.9 simultaneously. The symmetry of Doppler effect and range curves, answers the question as to why Side Looking Radar (SLR) systems are being used in remote sensing studies: to resolve the range ambiguities.

With a little work on the instantaneous frequency of the EM waves, the Doppler rate of moving sensors can be calculated as

$$Doppler_{rate}\big[rad/s/s\big] = \frac{4\pi V^2}{\lambda|\underline{R}|}, \tag{3.7}$$

As an example for ENVISAT-ASAR satellite, which was operating on C-band radar, ($|\underline{R}| \approx$) $800km$ above Earth's surface, and $V \approx 7.45km/s$, the Doppler rate could be calculated to be as $15568rad/s/s$.

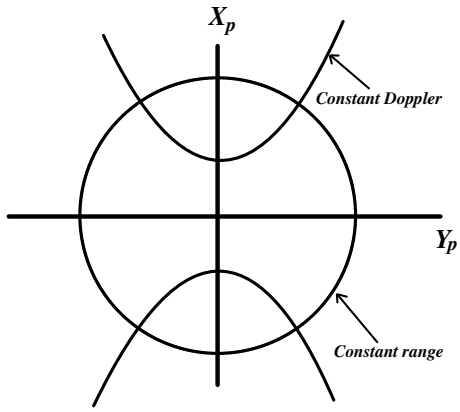

Figure 3.9. Constant Doppler and constant range representation in SAR. Scatterer is assumed to be at intersection of range and Doppler curves.

3.7 InSAR interferometry

Radio interferometry was developed after World War II [29]. So far, SAR interferometry has earned a considerable reputation in engineering, envi-

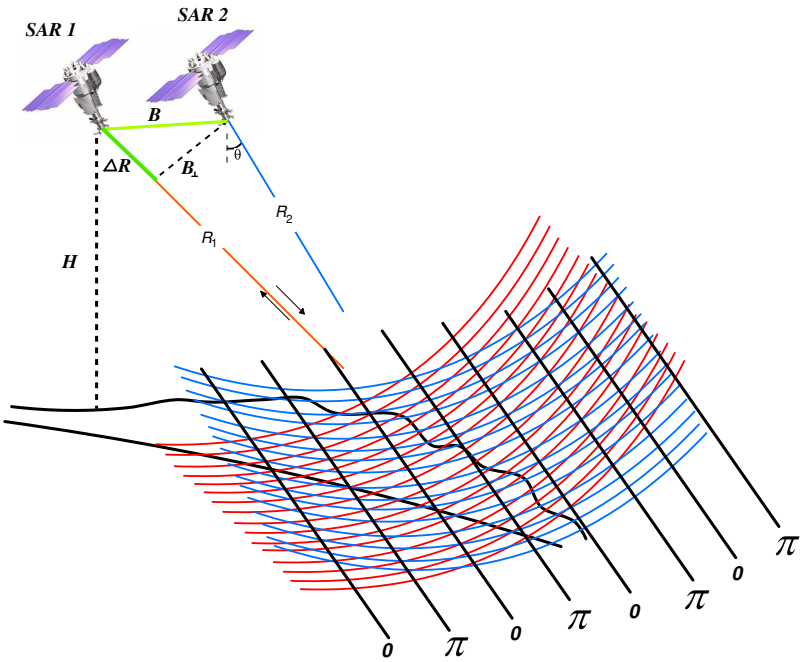

Figure 3.10. Concept of SAR interferometry in two pass radar antenna configuration, SAR1 and SAR2 (idea is from [30]).

ronmental science, oil and gas industries, Earth surface deformation, etc, achieving undeniable popularity in the monitoring of the Earth's surface.

Radar Interferometry is based on the interference/interaction of two EM waves, which in physics is demonstrated with a number of well-known experiments like Young's double-slit interferometry, Fraunhofer diffractions, Kirchhoff, and Fresnel experiments. The radar sources are coherent, signifying the consistency of the EM wave's properties, like frequency, and amplitude variations during the radar operation.

Radar interferometry is a simple extension of (say) Young's double-slit interferometric experiment. Two SAR radar antennas act like two point sources, similar to slits in the Young's double-slit interferometric experiment. The targeted surfaces will act like the curtain in the Young's experiment, and slices the interfered oncoming EM waves (from slits) into

different fringes. Therefore, the SAR images could be used for interferogram generation (even though they might not be measured at the same time).

In interferometry, phase information of the transmitted and backscattered signal, is the fundamental concept of the analysis. In comparison with the human body, a single eye is essentially "blind" when it comes to determining the difference in distance to object direction, thus for segregation of objects in distance, two eyes are needed [29]. Similarly in radar measurements for distinguishing two objects at the same range, different angle techniques must be applied [29]. For this reason, SAR images are acquired either by two antennas (single-pass) or by using repeat pass (double pass) acquisitions in the same orbit. In temporal repeat pass, data acquisitions are carried out in different time spacing (temporal baselines). Repeat pass data acquisitions in remote sensing can be done either in ascending or descending configurations. In ascending mode, the sensor moves from south to north (with the inclination angle of the orbits) and in descending mode, the sensor moves from north to south, and because SAR is a side looking acquisition method, the sensor looks west or east respectively.

From the historical point of view, the first InSAR interferogram produced by Zebker and Goldstein in 1986 [31] by multiplying two images and differentiation of the phase factor.

InSAR or radar interferometry practically is the phase consideration of two images that have been gathered from different locations and/or at different temporal baselines. The gathered images are multiplied together mathematically, and the phase part of this production further will be considered as the interferometric signature. Since the images' acquisition geometry, and satellite orbits are different, the target's coherency, and attached noises change over time. Meanwhile, many filtering regimes, geo-referencing, samplings of the images, and other kind of image enhancements, are inevitable (see for instance [32]).

Creation of topographic maps from interferometric measurements developed alongside InSAR interferometry [33], while DEMs (Digital Elevation Models) soon became a major tool in engineering, telecommunication, hydrology, Geo-hazards, cartography, and geophysics. Similar to stereographic methods, radar interferometric measurements of topography uses

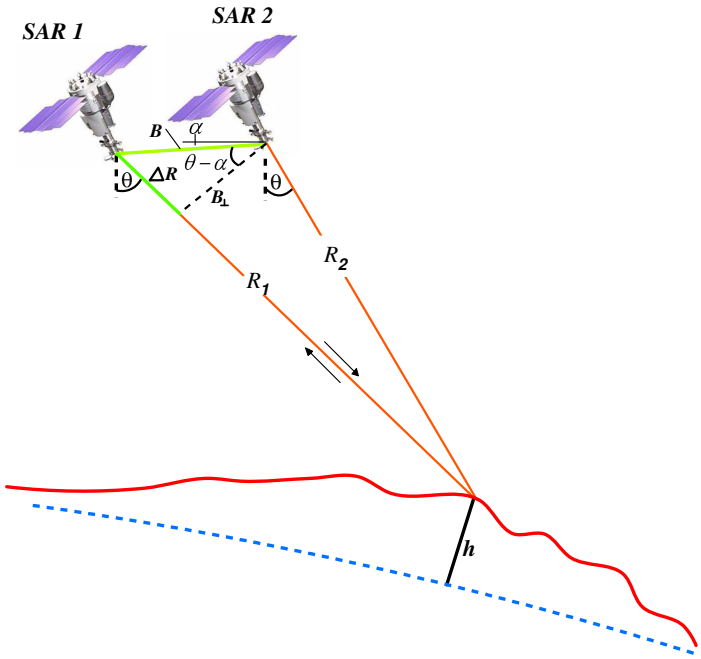

Figure 3.11. InSAR measurement configuration of the Earth's surface. The Earth's surface is not a flat surface, and the baseline B is not parallel to the Earth's surface.

two images for height segregations. The main difference is that in optical topography generation, parallax -direct angle measurements- is considered as the basic rule, but in the InSAR interferometry, ranging is the main player.

Interferometric DEM generation in a repeat pass method has its own problems like decorrelation -decrease of coherence over the time interval between the acquisitions-, layover, foreshortening, shadows, and atmospheric contamination of acquired data sets. After atmospheric errors, which can make the analysis difficult, baseline length (distance between two radar passes in orbits) could produce considerable errors too. For instance in repeat pass methodology, long baseline in DEM generations increases noise in InSAR data due to geometric de-correlations [31, 34]. Nevertheless, in single pass interferometry, similar to what SRTM mission

does (i.e., radar with simultaneously two operating antennas), such error is negligible, since the topography data/signal is acquired at the same time as the InSAR data/signal. Note that the possible deformation signal/component is also negligible, since the two imageries are acquired at the same time.

Besides topography mapping, Earth surface deformation monitoring with InSAR methodology is also possible with repeat pass data acquisition. The relative Line-Of-Sight (LOS) movement of scatterers in relation to a reference location/point in the image could be measured as a fraction of wavelength, yielding *cm* to *mm* accuracies for L, C, and X-band radars.

Figure 3.10 presents the main configuration of InSAR imaging. Two radar antennas mounted on two satellites (at the same or different times) namely $SAR1$ and $SAR2$, send the radar waves toward the Earth's surface, and collect the backscattered signals from targets. As is evident, the red and blue waves have interfered with one another, and the Earth's surface slices the interfered wave accordingly. Depending on the topography, the shape of the fringes varies. Since the radar's central wavelength is large enough (like L, C, and X), the signals could be digitized and the phase components could be measured easily. The measured phase then will be converted to the topography and/or deformation factors (if any).

Imagine that the Earth's surface is not flat and the baseline B is not parallel to the Earth's surface as depicted in Figure 3.11. The ground scatterer has a height of h relative to the Earth's geoids, i.e., zero altitude datum. We can see that $h = H_{sat} - Rcos(\theta - \alpha)$, and the differentiation of h with respect to the θ will be $\frac{\partial h}{\partial \theta} = Rsin(\theta - \alpha)$. Since $\Delta\varphi = \frac{4\pi\Delta R}{\lambda}$, and $\Delta R = Bsin(\theta - \alpha)$, the chain differentiation of the phase with respect to h reads:

$$\frac{\partial \Delta\varphi}{\partial h} = \frac{\partial \Delta\varphi}{\partial \theta}\frac{\partial \theta}{\partial h} = \frac{4\pi Bcos(\theta - \alpha)}{\lambda Rsin(\theta - \alpha)}, \tag{3.8}$$

which shows the change of the phase w.r.t. the elevation changes. By putting $B_\perp = Bcos(\theta - \alpha)$ (wherein α is the angle between B and the Earth's surface), we will get:

$$\frac{\partial \Delta\varphi}{\partial h} = \frac{4\pi B_\perp}{\lambda Rsin(\theta - \alpha)}, \tag{3.9}$$

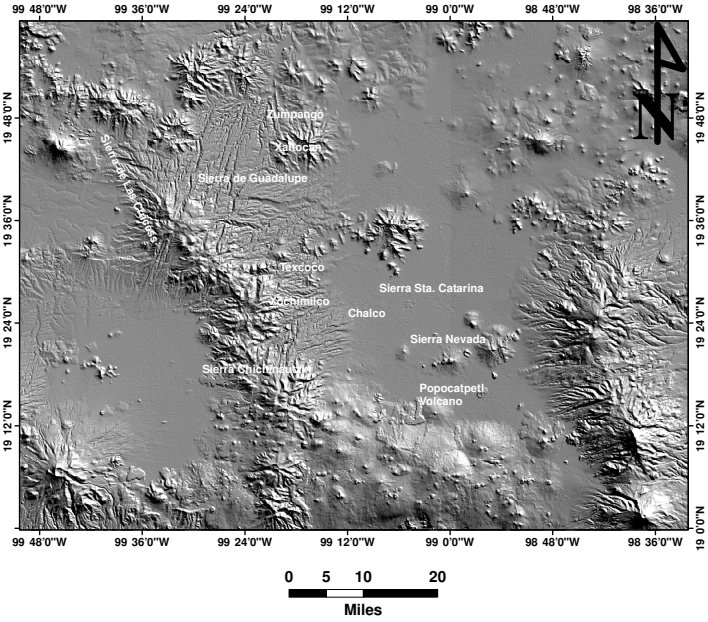

Figure 3.12. Shaded relief map generated from SRTM data of Mexico City area. The dataset is SRTM (3 arcsec), and the imagery resolution is 90m.

This equation shows that the rate of interferometric phase changes, is dependent on the elevation of the radar sensor $H_{sat} = Rcos(\theta - \alpha)$, perpendicular baseline $B_{\perp}$, and the radar wave incidence angle θ. As an example, for ERS satellites with $H_{sat} = 780km$, $\lambda = 5.6cm$, and $\theta = 23°$, for a perpendicular baseline $B_{\perp} = 500m$, we will get $\frac{\partial \Delta\varphi}{\partial h} = 338 \times 10^{-3}[rad/m]$. For a full round of phase i.e., $\Delta\varphi = 2\pi$, the elevation change will be $\Delta h = 18.6m$. In other words, a change of $18.6m$ on the elevation, will impose a full round fringe on the interferometric elevation imagery.

The accuracy of the ΔR is related to the baseline of the radar sensors, i.e., $\Delta R = R_1 - R_2 = Bsin(\theta - \alpha)$. For ordinary/direct measurements (without phase) this accuracy will be in the order of few hundred meters, which is not an acceptable level for InSAR analysis. If we consider the phase factor too, we will get ($\psi_i s$ are the phases from two radar sensors):

$$\Delta\varphi = \psi_1 - \psi_2 = -\frac{4\pi(R_1 - R_2)}{\lambda} = -\frac{4\pi\Delta R}{\lambda}, \tag{3.10}$$

By again putting $\Delta\varphi = 2\pi$, in equation (3.10), the rate of $\Delta R = 10^{-3}[rad/m]$ for the case of ERS1&2 sensors will be attained, which is a promising accuracy level for radar interferometric analysis.

Interferomtric SAR can be employed for generation of topographic or Digital Elevation Model (DEM) images. In other words, the change in the Earth surface elevation, imposes an extra phase at the rate of $\frac{\partial\Delta\varphi}{\partial h}$ which will be used further to generate the DEM images of the Earth's surfaces. In the example of Figure 3.11, we assume that both of the radar sensors have the ability to send and collect the radar waves separately. This task could also be done at the same time, implying that one of the radar sensors follows the other with a temporal delay of a few hours to a few years. For instance, such a configuration is valid for Italian CSK satellites, wherein the four constellation satellites are moving one after the other on predefined orbits, and could be used as an ideal instrument to generate the topography of the Earth's surfaces. In another configuration, valid for SRTM sensors, the radar system could have a transmitter and one or two receivers, to gather the radar data simultaneously. The baseline for SRTM sensor is in the order of $60m$, with the radar system capable of gathering the radar data simultaneously.

Figure 3.12 presents an example of radar topographic data: shaded relief map of SRTM dataset from Mexico City basin. The resolution for this data is $90m$, since higher resolution data is limited to specific areas like USA.

3.8 Terrain deformation

As shown in the last section, InSAR can be used for topographic image generation, assuming no significant change of the Earth's elevation. One of the brilliant uses of InSAR images is for measurement of mm order (or even sub mm) changes in the Earth's surface. To stress the importance of this kind of analysis, it is enough to say that more than 52 cities of Europe which host around 13% of the entire populations, were (and still are) under this kind of surveillance continually. One of the well-known

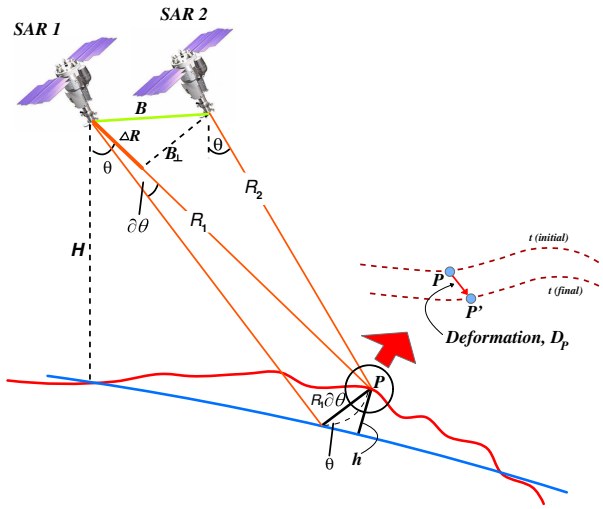

Figure 3.13. Fundamental representation of the Earth's surface change over time. Point P moves during the time period $t_{final} - t_{initial}$ to the new position.

InSAR programs for this kind of surveillance is named Pan-Geo, which mainly uses the InSAR time series like PSI and SBAS.

The First Earth surface deformation study with Interferometric SAR (InSAR) dates back to 1988 [35], where interferometric InSAR data was used to study ground motion rates over agricultural fields. After consecutive new generation satellites from ERS1&2 to CosmoSkyMed, and Sentinel-1, interferometric SAR (InSAR) mapping of deformations have acquired many proven abilities like studying urban areas, fault movements, sink holes, landslides, subsidence, uplifting, mining activities, glacier/ice cap motions, volcano deformation monitoring, etc. As explained earlier, the methodology is quite easy: for deformation mapping of an area, it is enough to have one pre-deformation (radar) image and one post-deformation image.

The geometry of terrain deformation measurement is given in Figure 3.13. Imagine a point P moves during the time period $t_{final} - t_{initial}$ to a new position, because of any kind of deformation criteria like earthquake, faults, subsidence, etc. The phase measured by two radar passes $SAR1$, and $SAR2$ at any pixel reads:

$$\begin{cases} \psi_1 = -\frac{4\pi R_1}{\lambda} + \psi_{scat1}, \\ \psi_2 = -\frac{4\pi R_2}{\lambda} + \psi_{scat2}, \end{cases} \tag{3.11}$$

where ψ_{scat1}, and ψ_{scat2} are the scattering phase attributes for the scatterer (ground) during the time period. Usually for good scatterers like what we have in urban areas, ψ_{scat1}, and ψ_{scat2} are considerably constant, which is not so for rural and highly vegetated areas. The interferometric phase could be measured by equation (3.10) with assumption of $\psi_{scat1} = \psi_{scat2}$. The derivation of this equation reads $\partial\Delta\varphi = -\frac{4\pi}{\lambda}\partial\Delta R$. As shown earlier $\Delta R = Bsin(\theta - \alpha)$, and its derivation is $\partial\Delta R = Bcos(\theta - \alpha)$. By substitution we have:

$$\partial\Delta\varphi = -\frac{4\pi}{\lambda}Bcos(\theta - \alpha)\partial\theta, \tag{3.12}$$

The elevation of point P relative to the Earth's ellipsoid is $h = R_1 sin\theta\partial\theta$ (see Figure 3.13), and the elevation changes with phase reads:

$$h = -\frac{\lambda R_1 sin\theta}{4\pi Bcos(\theta - \alpha)}\partial\Delta\varphi = -\frac{\lambda R_1 sin\theta}{4\pi B_\perp}\partial\Delta\varphi, \tag{3.13}$$

As this equation shows, the elevation of any point on the ground is inversely proportional to the perpendicular baseline $B_\perp$ ($B_\perp \neq 0$). Now, imagine that, the displacements of the point P along the Line Of Sight (LOS) during the time period $t_{final} - t_{initial}$, would be D_P. From equation (3.10)

$$\Delta\varphi = \psi_1 - \psi_1 = -\frac{4\pi\Delta R}{\lambda} = -\frac{4\pi}{\lambda}D_P, \tag{3.14}$$

where if $\Delta\varphi = 2\pi$, we get $D_P = -\lambda/2$, which means that one full cycle of fringe color changes, is equal to half of the satellite's given wavelength. In other words, if we move from one color like red to another level of red in the interferogram, the total elevation changes (i.e., deformation) in the sweeping of the color cycle, is equal to half of the given wavelength of the radar sensor. As an example, for ERS1&2 or ENVISAT sensors $D_P = -\lambda/2 = -2.813cm$, for each color cycle in the interferogram.

With consideration of the terrain and topographic phase together, the general equation of the phase changes for the InSAR survey reads

$$\partial\Delta\varphi = -\frac{4\pi\Delta R}{\lambda}\left(D_P + \frac{B_\perp}{R_1 sin\theta}h\right), \tag{3.15}$$

This equation shows that any imposed elevation and/or deformation in the Earth's elevation i.e., h and/or D_P will be a source of phase changes on the radar's interferograms. However, as this equation shows, sensitivities to Earth surface changes are 1000 times greater than sensitivity to topographical changes; due to the presence of R_1 factor in the denominator of the equation (3.15), in respect of topographic phases.

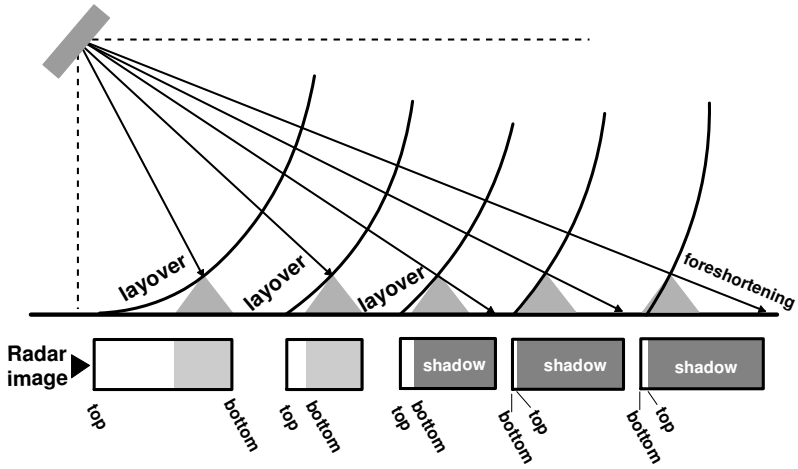

Figure 3.14. Geometric distortions inherent in SAR data acquisition methodology: Layover, foreshortening, and shadows.

3.9 InSAR data processing concepts

In InSAR data analysis, look angle θ varies for different sorts of satellites and different configurations. For instance, usually ERS uses 20.3° and CosmoSkyMed uses 33.1° (mostly). The dielectric properties of the environments and range/distance of target from satellite, cause a time delay and decrease in strength of returned signals, which could be translated to the imaginary and real (complex numbers) part of the received signals.

Since InSAR is Side Looking imaging Radar system (SLR), geometric distortion is inherent in SLR methods. Figure 3.14 depicts some important distortion types that are most probable in SAR analysis: Layover, foreshortening, and shadows. Whenever the radar's incidence angle is greater than the terrain's slope angle, radar shadows will occur. The opposite setting is known as layover: when the radar's incidence angle is smaller than the terrain's slope angle. Some mathematical methods, multiple looking InSAR, and use of proper DEM could mitigate/rectify this kind of distortion effectively.

As mentioned earlier, the InSAR images consist of two-2D arrays (raw and column) that are filled with complex values named phasors-each point has a real and an imaginary part. InSAR images are in multi looked formats and must be focused based on some algorithms like GAMMA and ROI-PAC approaches, to be able to feed to the InSAR processors.

From the statistical point of view, amplitude of a received signal in the InSAR imageries can be modeled by the Rice probability distribution function [36]

$$f_a(a) = \frac{2a}{\sigma_n^2} \times I_0\left(\frac{2a}{\sigma_n^2}\right) \times e^{-(1+a^2)/\sigma_n^2}, \tag{3.16}$$

where $a = \| z \|$ is the amplitude of the signal, and $I_0(\cdot)$ is the modified Bessel function. "n" is the noise part from other objects/scatterers and uncorrelated noise (white noise) sources. We assume the noise has circular Gaussian distribution function with zero mean and variance of σ_n^2.

Correspondingly, the phase part $\angle z = \theta$ can be modeled with error distribution functions [37]

$$f_\theta(\theta) = \frac{1}{2\pi} \times e^{-(sin^2\theta)/\sigma_n^2} \times \left[e^{-(cos^2\theta)/\sigma_n^2} + \sqrt{\frac{\pi}{\sigma_n^2}} cos\theta \times erfc\left(-\sqrt{\frac{1}{\sigma_n^2}} cos\theta \right) \right], \tag{3.17}$$

If we define InSAR (or SAR) image arrays (filled with complex numbers) by Z_1 and Z_2, from basic algebra

$$\begin{cases} Z_1 = |Z_1| exp(j\theta_1), \\ Z_2 = |Z_2| exp(j\theta_2), \end{cases} \tag{3.18}$$

Depending on the size of the study area i.e., Area Of Interest (AOI), InSAR/SAR images should be cropped to the proper dimensions to cover the entire targets, this also helps to reduce the analysis time and PC memory requirements.

The next step in InSAR/SAR data analyzing is re-sampling of one image with respect to another one, to facilitate the multiplication of images. Selection of the optimal kernel and interpolation methods in the re-sampling step is very crucial. As reported by [29], re-sampling and/or interpolation errors are highly dependent on the correlation between two images, i.e., variance-covariance matrices. But strictly speaking, there is not a single and deterministic kernel for all types of InSAR/SAR interpolation and re-sampling processes, and they should be found with some focused work.

For generating of the interferogram (ifg), we multiply the so-called "master" image by the re-sampled conjugate of the other so-called "slave" image

$$ifg = Z_1 Z_2^* exp\big(j(\theta_1 - \theta_2)\big), \tag{3.19}$$

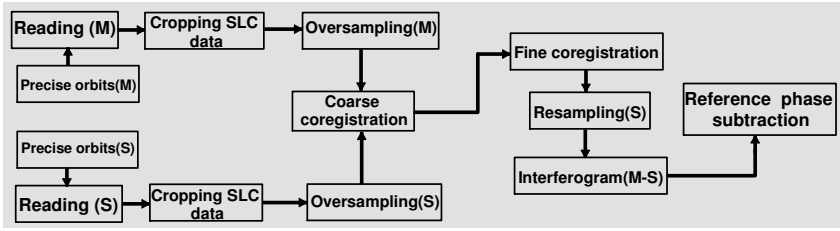

Figure 3.15. Flowchart overview of interferometric processing of InSAR imagery based on the DORIS approach.

where $*$, means the complex conjugate of the InSAR image array. ifg represents the interferogram produced between two InSAR images. Coherency of the targets during the time period -correlation between two InSAR images- is one of the most important factors in InSAR interferometry. If two images have weak or no correlation during the radar scanning temporal baseline, we say these two images are de-correlated (or uncorrelated). Usually man-made structures like buildings, railways, and roads in urban areas remain coherent in radar interferograms for a long time,

while their surroundings (like rural areas) stay completely de-correlated [38, 39, 40, 41, 42].

Phase unwrapping procedure -resolving of the phase ambiguity- is the other important and crucial part of InSAR/SAR data processing (see for instance [33, 43, 44, 45]). When coherency decreases, the phase unwrapping around the low coherence area would be very difficult and inaccurate (see for instance [46, 47, 48, 49]). The upcoming sections talk about coherency of points instead of whole images (time series methodology), that increase the feasibility and ease of interpretation of our InSAR data analysis.

Another important issue, that could be a possible source of huge errors, is co-registration of InSAR/SAR images. Co-registration ensures that each ground target contributes to the same range and azimuth in both master and slave images. In some satellites like ERS1&2 and ENVISAT-ASAR, co-registration is very simple: just a small rotation of two images or a range and azimuth stretch take care of the co-registration step. But in general, and mainly in rough topography conditions, high order kernel polynomials must be applied to minimize the co-registration errors. In softwares programs like DORIS, the co-registration step is designed to be in coarse and fine scales [50]. Validation analyses for interferometry and PSI analyses frequently report that co-registration errors are very crucial issues that must be judiciously taken care of (for instance, see [51, 52]).

There are lots of InSAR (or SAR) software programs that are capable of performing the entire aforementioned analysis. Some of them like ROI-PAC, DORIS, and NEST are used in this book.

ROI-PAC is a software package created by the Jet Propulsion Laboratory division of NASA and CalTech for processing of InSAR images and generating interferograms. ROI-PAC stands for Repeat Orbit Interferometry PACkage and is UNIX based.

DORIS (Delft Object-oriented Radar Interferometric Software) is also used extensively for InSAR data processing from Delft University of Technology (Netherlands). Some other available softwares for InSAR and PSI analysis software packages are listed below with brief explanation:

1. **ScatterersTM** - The most popular InSAR and PSI data analysis software that include the original Permanent scatterer from Tele Rilevamento Europe (TRE).

2. **GMTSAR**- An InSAR processing system based on Generic Mapping Tools (GMT)-open source GNU General Public License- [53].

3. **GAMMA software** - Commercial software with different modules covering SAR data processing, SAR Interferometry, differential SAR Interferometry, and Interferometric Point Target Analysis (IPTA), which is comparable to the PSI procedure.

4. **SARscape** - Commercial software consisting of different modules covering SAR data processing, SAR and ScanSAR focusing and Interferometry, differential SAR Interferometry, Persistent Scatterers and SBAS, Polarimetry and Polarimetric Interferometry, running as an extension of ENVI on Windows and/or Linux OSs.

5. **PulSAR** - Commercial software from Phoenix systems for InSAR data analysis, works on UNIX based computers.

6. **DIAPASON** - Originally developed by the French Space Agency CNES, and maintained by Altamira Information, Commercial software suite for UNIX and Windows.

7. **RAT (RAdar Tools)** - A free software based on IDL (Interactive Data Language) programming language, and can be used for interferometry (InSAR), Polarimetric Interferometry SAR (PolInSAR) etc., works on Windows and Linux.

8. **NEST (Next ESA SAR Toolbox)** - is a user friendly open source toolbox (JAVA) for InSAR data processing. Core is DORIS and with a few clicks Interferograms could be produced easily. No PSI analysis available.

9. **StaMPS (Stanford Method for Persistent Scatterers)** - is a software package for InSAR and persistent scatterer (PS) analysis. It uses DORIS for interferogram production to feed data to the PSI processor.

The key steps of DORIS approach to interferogram generation, are summarized in Figure 3.15.

As an example of InSAR data analysis for interferogram generation, Bam's earthquake data from Iran have been processed in Figure 3.16.

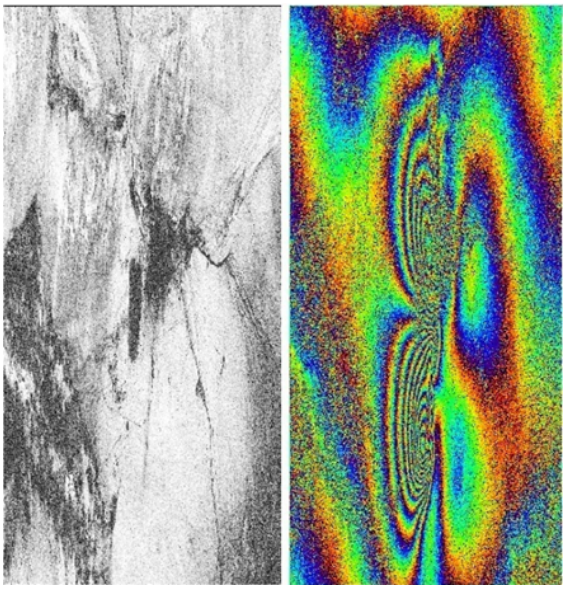

Figure 3.16. Interferogram (right) and coherence (left) map of Bam (Iran) earthquake have been produced based on two ENVISAT-ASAR images before (03/12/2003) and after (11/02/2004) earthquake with NEST software.

Two ENVISAT-ASAR images of 03,12,2003 and 11,02,2004 from Bam area (Iran) earthquake (26 December, 2003) have been imported to NEST software, and interferogram (right panel) and coherence map (left panel) have been generated. For this analysis $B_{temp} = 70$ days (temporal baseline), and $B_{\perp} = 0.6m$ (perpendicular baseline) respectively. This kind of analysis could help us to model earthquakes and dynamical movements of the Earth's surfaces in terms of strain accumulation calculation. The map with colored fringes, shows the deformation of the Earth's surface. Each color cycle- for instance from red to red- shows a deformation rate in the radar's Line Of Sight (LOS), in the order of 2.8 centimeters (= 5.6/2 half of the signal wavelength in C-band). The produced interferogram and coherence maps are presented in radar coordinates (i.e., non geo-referenced representation). For similar areas with high risk of earthquakes, frequent radar observations, and strain accumulation rate monitoring, could help us to assess the risk of probable upcoming earthquakes.

In the next chapter, the more effective methodology for InSAR data analysis, i.e., Persistent Scatterer Interferometry (PSI) will be addressed in details.

Bibliography

[1] Skolnik, M. I., *Radar Handbook,* McGraw-Hill, New York, 1970.

[2] Curlander, J. C. and R. N. McDounough, *Synthetic Aperture Radar, Systems and Signal Processing,* John Wiley & Sons, New York, 1991.

[3] Ulaby, F. T., R. K. Moore, and A. K. Fung, *Microwave Remote Sensing: Active and Passive, Vol.I,* Artech House, Norwood, 1981.

[4] Thompson, T. W., A User's Guide for the NASA/JPL Synthetic Aperture Radar and the NASA/JPL L- and C-band Scatterometers, 8338, *JPL Publication,* 1986.

[5] *IEEE standard dictionary of electrical and electronic terms, 3rd ed.,* ANSI/IEEE standard 100-1984.

[6] Drinkwater, M. K., R. Kwok, and E. Rignot, "Synthetic aperture radar polarimetry of sea ice," *Proceeding of the 1990 International Geoscience and Remote Sensing Symposium,* Vol. 2, 15251528, 1990.

[7] Walker, B., G. Sander, M. Thompson, B. Burns, R. Fellerhoff, and D. Dubbert, "A high-resolution, four-band SAR Testbed with real-time image formation," *Proceeding of the 1986 International Geoscience and Remote Sensing Symposium,* 18811885, 1996.

[8] Storvold, R., E. Malnes, Y. Larsen, K. A. Hogda, S.-E. Hamran, K. Mueller, and K. Langley, "SAR remote sensing of snow parameters in norwegian areas - Current status and future perspective," *Journal of Electromagnetic Waves and Applications,* Vol. 20, No.13, 17511759, 2006.

[9] Hovland, H. A., J. A. Johannessen, and G. Digranes, "Slick detection in SAR images," *Proceeding of the 1994 International Geoscience and Remote Sensing Symposium,* 20382040, 1994.

[10] Alpers, W.R. 1983. Monte Carlo simulations for studying the relationship between ocean wave and synthetic aperture radar spectra. *J. Geophysical Research,* vol.88, no. C3, pp. 17451759.

[11] Alpers, W.R. and C. Bruning 1986. On the relative importance of notionrelated contributions to the SAR imaging mechanism of ocean surface waves. *IEEE Transactions on Geoscience and Remote Sensing,* vol. GE- 24, no.6, pp. 873885.

[12] Lynne, G. L, and G. R. Taylor, "Geological assessment of SIRB imagery of the amadeus basin," *IEEE Transactions on Geoscience and Remote Sensing,* Vol. 24, No. 4, 575581, 1986.

[13] Grenerczy, G, Wegmller, Urs. 2012. Deformation analysis of a burst red mud reservoir using combined descending and ascending pass ENVISAT ASAR data. *Nat Hazards* (2013). DOI: 10.1007/s11069-012-0470-4.

[14] I. Hajnsek, *"Inversion of surface parameters from polarimetric SAR,"* Ph.D. dissertation, DLR, Oberpfaffenhofen, Germany, 2001.

[15] Lanari, R., Lundgren, P., Manzo, M., Casu, F., Dec. 2004. Satellite radar interferometry time series analysis of surface deformation for Los Angeles, California. *Geophysical Research Letters* 31, 23613.

[16] Kong, J. A., S. H. Yueh, H. H. Lim, R. T. Shin, and J. J. van Zyl, "Classification of earth terrain using polarimetric synthetic aperture radar images," *Progress In Electromagnetics Research,* PIER 03, 327370, 1990.

[17] Joe, P., J. Scott, J. Sydor, A. Brando, & A. Yongacoglu, "Radio local area network (RLAN) and C-band weather and radar interference studies", *Proceedings of the 32 AMS Radar Conference on Radar Meteorology,* Albuquerque, New Mexico, Oct 24-29, 2005.

[18] Bell, J., Amelung, F., Ramelli, A., Blewitt, G. (2002). Land subsidence in Las Vegas, Nevada, 19352000: New geodetic data show evolution, revised spatial patterns, and reduced rates. *Environmental and Engineering Geoscience,* 8(3), 155174.

[19] A. Hooper, H. Zebker, P. Segall, and B. Kampes. A new method for measuring deformation on volcanoes and other natural terrains using InSAR persistent scatterers. *Geophysical Research Letters,* 31(23), 2004.

[20] Nelson SA (2000) *Subsidence: dissolution and human-related causes.* University of Tulane, http://www.tulane.edu/ sanelson/-geol204/subsidence.htm.

[21] Held, D. N., W. E. Brown, A. Freeman, J. D. Klein, H. Zebker, T. Sato, T. Miller, Q. Nguyen, and Y. L. Lou, "The NASA/JPL multifrequency, multipolarisation airborne SAR system," *Proceeding of the 1988 International Geoscience and Remote Sensing Symposium,* 345349, 1988.

[22] Thompson, D. G., D. V. Arnold, and D. G. Long, "YSAR: A compact, low-cost synthetic aperture radar," *Proceeding of the 1996 International Geoscience and Remote Sensing Symposium,* 18921894, 1996.

[23] Livingstone, C. E., A. L. Gray, R. K. Hawkins, and R. B. Olsen, "CCRS C/X-airborne synthetic aperture radar: An R&D tool for the ERS-1 time frame," *IEEE Aerospace and Electronic Systems Magazine,* Vol.3, No. 10, 1120, 1988.

[24] Jordan, R. L., B. L. Huneycutt, and M. Werner, "The SIR-C/XSAR synthetic aperture radar system," *IEEE Transactions on Geoscience and Remote Sensing,* Vol. 33, Issue 4, 829839, 1995.

[25] Nemoto, Y., H. Nishino, M. Ono, H. Mizutamari, and K. Nishikawa, K. Tanaka, "Japanese Earth Resources Satellite- 1 synthetic aperture radar," *Proceedings of the IEEE,* Vol.79, Issue 6, 800809, 1991.

[26] Birk, R., W. Camus, E. Valenti, and W. J. McCandles, "Synthetic aperture radar imaging systems," *IEEE Aerospace and Electronic Systems Magazine,* Vol. 10, No.11, 1523, 1995.

[27] Way, J. and E. A. Smith, "The evolution of synthetic aperture radar systems and their progression to the EOS SAR," *IEEE Transactions on Geoscience and Remote Sensing,* Vol. 29, Issue 6, 962985, 1991.

[28] Agenzia Spaziale Italiana (2007). *"COSMO-SkyMed System Description and User Guide", Document No: ASI-CSM-ENG-RS-093-A.* Roma, Italy: ASI, Agenzia Spaziale Italiana.

[29] Hanssen, R. F., 2001. *Radar Interferometry: Data Interpretation and Error Analysis.* Kluwer Academic, Dordrecht.

[30] Bamler R, Hartl P (1998) *Synthetic aperture radar interferometry.* Inverse Problems 14:154.

[31] Zebker, H. A., Villasensor, J., Sep. 1992. Decorrelation in interferometric radar echoes. *IEEE Transactions on Geoscience and Remote Sensing* 30, 950-959. URL http://adsabs.harvard.edu/abs/1992ITGRS..30..950Z14.

[32] Small, D., Rosich, B., Meier, E., Nuesch, D., 2004. Geometric calibration and validation of ASAR imagery. *In: Proc. of CEOS SAR Workshop.*

[33] Goldstein, R. M., H. A. Zebker, and C. L. Werner (1988), Satellite Radar Interferometry: Two-Dimensional Phase Unwrapping, *Radio Science,* 23(4), 713720.

[34] Zebker, H. A., P. A. Rosen, and S. Hensley (1997), Atmospheric effects in interferometric synthetic aperture radar surface deformation and topographic maps, *J. Geophysical Research,* 102(B4), 75477563.

[35] Andrew K. Gabriel and Richard M. Goldstein, "Crossed orbit interferometry: theory and experimental results from SIR-B," International Journal of Remote Sensing, vol. 9, no. 5, pp. 857, 1988.

[36] Papoulis, A., *Probability, Random Variables and Stochastic Processes*, 3rd edn., McGraw-Hill, New York, 1991.

[37] Abramovitz, Milton & Irene Stegun, 1972, *Handbook of Mathematical Functions. With Formulas, Graphs, and Mathematical Tables.* Dover Publications, New York.

[38] Usai, S. and Klees, R. (1998), On the Feasibility of Long Time Scale INSAR, *in: International Geoscience and Remote Sensing Symposium,* Seattle, Washington, USA, 610 July 1998, pp. 24482450.

[39] Usai, S. and Klees, R. (1999a), On the interferometric characteristics of anthropogenic features, *in: International Geoscience and Remote Sensing Symposium,* Hamburg, Germany, 28 June2 July 1999.

[40] Usai, S. and Klees, R. (1999b), SAR Interferometry On Very Long Time Scale: A Study of the Interferometric Characteristics Of Man-Made Features, *IEEE Transactions on Geoscience and Remote Sensing,* 37(4):21182123.

[41] Usai, S. and Hanssen, R. (1997), Long time scale INSAR by means of high coherence features, *in: Third ERS SymposiumSpace at the Service of our Environment,* Florence, Italy, 1721 March 1997, pp. 225228.

[42] Usai, S. (1997), The use of man-made features for long time scale INSAR, *in: International Geoscience and Remote Sensing Symposium,* Singapore, 38 Aug 1997, pp. 15421544.

[43] Costantini, M. A novel phase unwrapping method based on network programming. *IEEE Transactions on Geoscience and Remote Sensing*, 1998, 36, 813-821.

[44] Costantini, M.; Farina, A.; Zirilli, F. A fast phase unwrapping algorithm for SAR interferometry. *IEEE Transactions on Geoscience and Remote Sensing*, 1999, 37, 452-460.

[45] Tribolet, J. (1977), A New Phase Unwrapping Algorithm, Acoustics, Speech and Signal Processing, *IEEE Transactions on Geoscience and Remote Sensing,* 25(2), 170177.

[46] Teunissen, P. J. G. (1988), *Towards a Least-Squares Framework for Adjusting and Testing of both Functional and Stochastic Models*, vol.26 of Mathematical Geodesy and Positioning series, Delft University of Technology.

[47] Teunissen, P. J. G. (1995), The least-squares ambiguity decorrelation adjustment: a method for fast GPS integer ambiguity estimation, *Journal of Geodesy,* 70(12):6582.

[48] Teunissen, P. J. G. (2000a), *Adjustment Theory; An Introduction*, Delft University Press, Delft, 1st edition.

[49] Teunissen, P. J. G. (2000b), *Testing Theory; An Introduction*, Delft University Press, Delft, 1st edition.

[50] Kampes, B., Usai, S., 1999. Doris: The delft object-oriented radar interferometric software. *In PROC. 2nd int. symp. Operationalization of remote sensing.* URL http://citeseerx.ist.psu.edu/viewdoc/summary?doi=10.1.1.46.1689.

[51] (Available online): www.terrafirma.eu.com/validation.

[52] (Available online): www. Earth.esa.int/psic4 validation projects.

[53] (Available online): http://topex.ucsd.edu/gmtsar.

Chapter 4

Stability of Railways studied in Campania (Italy) with InSAR data

In this chapter railways' stability in Campania (Italy) by space-borne Differential Interferometric Synthetic Aperture Radar (DInSAR) techniques is discussed. Radar (DInSAR) techniques have shown their capabilities in monitoring of Earth surface displacements. Persistent Scatterer Interferometry (PSI) methodology is gradually becoming known for its capabilities of providing ground displacement monitoring with an accuracy up to the millimeter scale, especially in urbanized areas, where the Earth surface's deformation risk is much noticeable. In particular, Campania region is characterized by intense urbanization, active volcanoes, complicated fault systems, landslides, subsidence, and hydrological instability; therefore, the stability of public transportation structures is highly concerned. We have applied Differential Interferometric Synthetic Aperture Radar (DInSAR), and PSI techniques to a stack of 25 X-band radar images of Cosmo-SkyMed (CSK) satellites collected over an area in Campania (Italy), in order to monitor the railways' stability. The study area was already under investigation with older, low-resolution sensors like ERS1&2 and ENVISAT-ASAR before, but the number of obtained persistent scatterers (PSs) was too limited to get useful results.

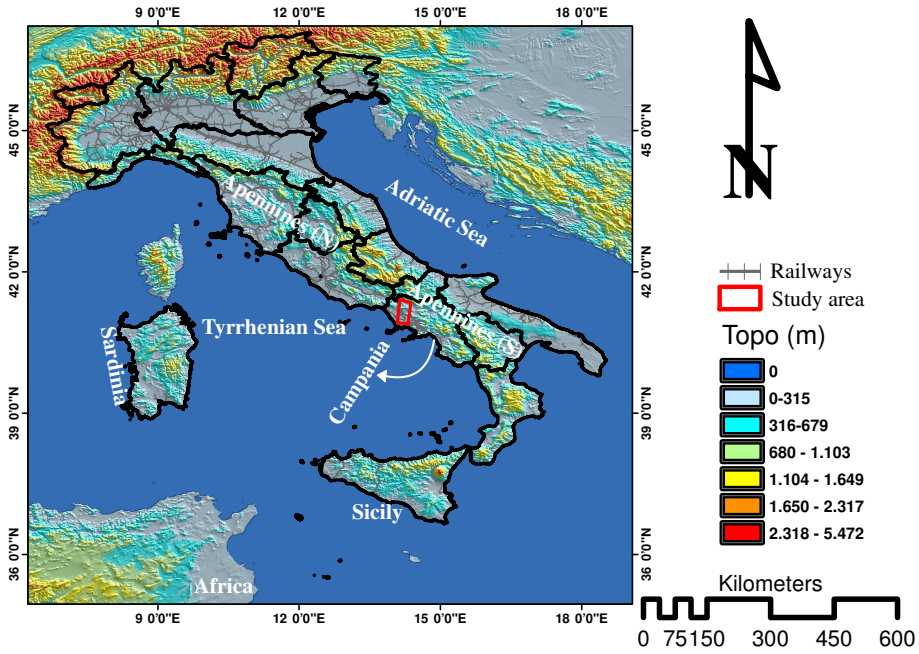

Figure 4.1. Campania region (Italy) and the study area.

4.1 Introduction

Persistent Scatterer Interferometry (PSI) is a powerful technique that has been employed for more than 15 years for studying/monitoring of soil deformation rates.

Historically speaking, different PSI techniques have been proposed in the last decades [1, 2, 3, 4, 5]. The first PSI technique, named Permanent Scatterers Interferometry, was developed by researchers of the Politecnico di Milano (POLIMI) [4, 5]. Soon after, some other similar methodologies have been rapidly developed. The other similar well known time series radar interferometric approach is named Small Baseline Subset (SBAS) [6, 10].

In PSI analysis all acquisitions are employed, whereas in SBAS some of them are not, because their spatial baseline is too high. SBAS methodologies are more sensitive to geometric and temporal decorrelation com-

pared to PSI analysis [6]. In SBAS, much more interferograms are created than in a single master approach (like PSI). The unwrapping procedure for SBAS and PSI is also different. In SBAS, at least in its original implementation, the interferograms are unwrapped first spatially and then temporally, while it is the opposite in the PSI analysis. One of the major disadvantages of SBAS is that in this approach disconnected clusters of interferograms might be obtained in the temporal and perpendicular baseline graphs. However, SBAS allows to measure displacements not only on highly stable point-like scatterers, but also on distributed scatterers (DS), i.e., areas with intermediate coherence. Therefore, several researches have been reported aiming to develop techniques able to combine advantages of both PSI and SBAS. For instance, minimization of the baselines and use of all radar images also in SBAS methodology were proposed in the literature (e.g., [11]). Another similar technique for the earth surface's change monitoring was reported in [12]. A geophysical approach in [13] and a stepwise linear deformation with least square adjustment in [14] has been reported. Interferometric Point Target Analysis (IPTA), and stable point networks are reported in [15] and [16], respectively. In [17] multiple image pixels are used within a certain radius to estimate spatially correlated parameters (e.g., deformation rates, atmospheric signal delay). In this methodology, PSI and small baseline analysis have been combined heuristically. The SqueeSAR algorithm, capable of simultaneous analysis of PSI (i.e., PS) and DS, was reported in [18]. In SqueeSAR algorithm, combination of PS and DS helps to work in rural areas, where the coherency is lower. In [19] a similar algorithm, with contribution of polarimetric based radar data, was heuristically proposed. All the different PSI implementations described above, however, share some main features, that are described in the following. In all of them, a large stack of radar images are considered for estimation of historical changes of the Earth surface's, with proper modeling techniques. The output of PSI algorithms are deformation time series of the scatterers, and the elevation of those scatterers. PSI technique exploits the fact that some radar's pixels remain coherent during the time. With this method and by using a large stack of SAR images (usually more than 20 SAR images), atmospheric errors (i.e., the Atmospheric Phase Screen, APS) can be estimated with sufficient accuracy, and the proper phase correction can be implemented to remove them. In the standard

PSI methodologies, a single master image with specific criteria is selected (from N given images), and $(N-1)$ differential interferograms w.r.t. the master image are generated. Then, with different approaches, Permanent Scatterers Candidates (PSCs) are selected. By refinements of the selected PSCs, and by using Permanent Scatterers Potentials (PSPs)[20], final Permanent Scatterers (PSs) can be generated. For each PS point, time series of the historical records of the Earth surface's height changes, and the height of each PS with respect to a reference point, are measurable. This methodology shows promising results in urban areas, where it is able to achieve an average of $100 PSs/km^2$ (points densities) with low resolution sensors like ERS1/2 and ENVISAT-ASAR, and an average of a couple of thousands PSs/km^2 with high resolution sensors like TerraSAR-X and Cosmo-SkyMed. On the contrary, the rural/vegetated areas might not be explored properly with PSI methodology. The main reason is the absence of proper stable scatterers in such areas. Another disadvantage of the PSI is the need for a minimum amount of images for making appropriate phase unwrapping steps, which could severely influence the degree of correctness of the selected PSC. The other limitation of InSAR time series methodologies, is that PSI (and SBAS too) is a relative technique, i.e., all of the calculated time series for PS points are measured w.r.t. a reference point, which is assumed to be without any kind of movements. Nonetheless, many promising methodologies, like continuous GPS or leveling, could resolve this problem properly [21]. Another limitation is mainly due to the observation geometry of the satellite systems. PSI deformation rates are only measured along the satellite Line Of Sight (LOS) direction; therefore, the obtained value of the deformation is actually just the projection of the deformation vector onto the SAR look direction.

4.2 Study area

The Campania region includes the Campania plain as a Northwest-Southeast elongated structure (see Figure 4.1) delimited at north, south and east by the Apennines chain (see Figure 4.1). To the west, the Campania region is bounded by the Tyrrhenian Sea. Intense urbanization, active volcanoes, complicated fault systems, landslides, subsidence, and hydrological instability (flooding) are the characteristics of this region [22, 23, 24, 25, 26].

246 out of 652 sinkholes (38%) of entire Italy are located in Campania region itself [26]. Volcanism is very developed in this area and is observed at Roccamonfina, Ischia, Vesuvius, and Phlegraean Fields regions. Historical eruptions happened at Vesuvius (several, the last one in 1944 A.D.), Ischia (1302 A.D.), and Phlegraean Fields (1538 A.D.). Complicated fault systems are developed in Campania, which can be observed in many locations. Complicated behavior of the hydrothermal systems played a key role in triggering of seismicity, uplift and subsidence in Vesuvius, Ischia, and Phlegraean Fields. Many destructive historical earthquakes happened in Campania: 1930 (Ms=6.7), 1962 (Ms=6.2), 1980 (Ms=6.9). Most of the previous studies from Leveling, GPS, and SAR data are concentrated on the volcanic areas like Vesuvius, and Napoli city itself. Conversely, we are here interested in the area at north of Napoli, including the Volturno river and a local railway, see Figure 4.2, with a bridge at Triflisco on which our interest is mainly focused. This bridge over the Volturno river and the entire railway considered in this study were made in 1953. In order to increase the stability of this bridge, the local railway company (EAV) made some rock bolts installations and cement injections to make the three pillars of the bridge more stable. Despite these efforts, EAV still was interested to evaluate the probable geophysical change of the railways (deformation rates) with other independent methods like InSAR and PSI.

4.3 Methodology

Several different algorithms for PSI methodologies have been proposed in the last 15 years, but most of them follow this standard routine/mechanism [20]:

(i) Generation of the interferograms based on the available InSAR imageries.

(ii) Generation of differential interferograms using a Digital Elevation Model (DEM) and orbit data.

(iii) Selection of Permanent Scatterer Candidates (PSC).

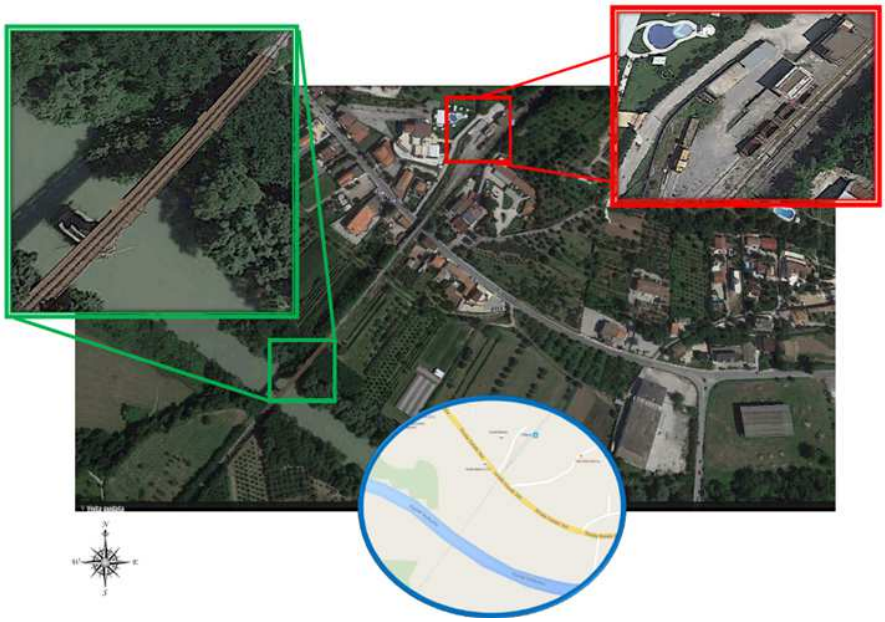

Figure 4.2. Study area, railways, targeted bridge, and Volturno river are depicted in this Figure. Down in the middle a global view of the study area is depicted (from google map). On top left, the targeted bridge of the Volturno river, and on the top right, the train station are enlarged.

(iv) Refinement of PSCs to get the real PSs with different methodologies and phase unwrapping.

(v) Repeating of the steps from (i) to (iv), with Permanent Scatterer Potentials (PSPs) to densify (compact) the PSs network.

Producing of InSAR interferograms from InSAR imageries is the fundamental concept of PSI analysis. For N available InSAR images, $N-1$ interferogrms could be generated with respect to the selected master (m) image. There are number of different methodologies to select the master image from the entire set of N radar images. The most important one is based on minimization of the dispersion of the perpendicular baseline. In [20] also another methodology based on maximization of coherence of interferometric stack is presented. In this work, we perform a heuristic

minimization of the perpendicular and temporal baseline dispersion: we visually select the most central image in the graph of temporal/perpendicular baselines, shown in Figure 4.3.

After selection of the master image (m) and generation of interferograms, a DEM and precise orbit data must be used to generate $N-1$ differential interferograms from N radar images. The differential phase equation for a differential interferogram reads:

$$\phi = \varphi_{atm} + \varphi_{orb} + \varphi_{def} + \varphi_{scat} + \varphi_{DEM} + \varphi_n, \tag{4.1}$$

We are interested in the surface displacement component of the total observed phase (φ_{def}). Other contributions to the total observed phase are the topographic contribution φ_{DEM}, and the orbital error φ_{oeb}, that can be minimized using precise orbit data. The atmospheric contribution, φ_{atm} is related to the APS, and φ_{scat} is the change in the scattering attributes over the time. Usually, the scattering component is small in manmade objects (like railways). Finally φ_n is the noise component of the phase, which for strong scatterers should be negligible. With selection of proper DEM data, and precise orbit data, the topographic and orbital phase components in general phase equation would be handled properly.

Amplitude dispersion index D_a is used to generate the first rank Persistent Scatterer Candidate (PSC). This index is defined as the ratio of standard deviation σ_a and temporal mean $\langle a \rangle$ of the pixel's (temporal) amplitudes a, and it can be also approximately related to the phase standard deviation σ_φ [27]:

$$D_a = \frac{\sigma_a}{\langle a \rangle} \cong tan(\sigma_\varphi) \cong \sigma_\varphi, \tag{4.2}$$

where the last approximate equality holds for small values of σ_φ (i.e., $\sigma_\varphi < 0.25$).

Points for which this index is smaller than a prescribed user-defined threshold are selected. The choice of the threshold for D_a may depend on the number of images, but usually it lies in the range from 0.2 to 0.3. [27]. The selected points (PSCs) are used to make the first rank network. Assume that φ_i^{ms} is the interferometric phase difference between master (m) and slave (s) imageries, for persistent scatterer in position i. At the

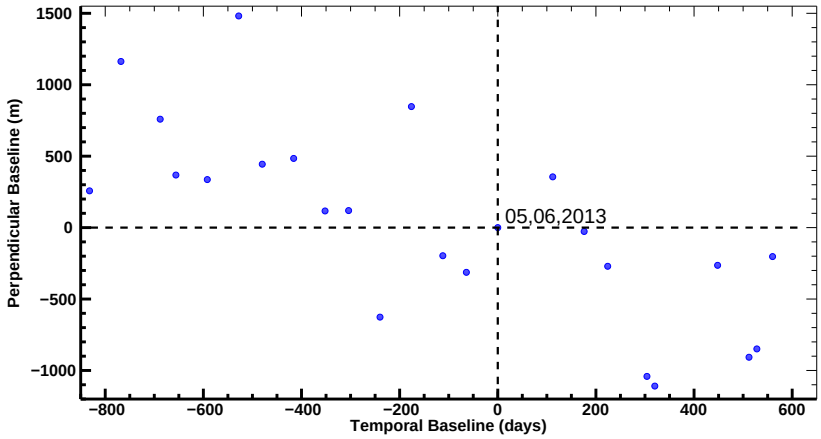

Figure 4.3. Perpendicular and temporal baselines. The image acquired on 2013 06 05 has been selected as the master image.

beginning, the phase difference φ_i^{ms} is ambiguous -wrapped- and should be unwrapped to get the actual -physically meaningful- amount of phase.

The first "interpretable" PSI observation is the double-difference φ_{ij}^{ms}, which is the difference between φ_i^{ms} and φ_j^{ms}, where i and j are two different PSs, so that is represented both in temporal and spatial domains simultaneously. This implies that PSI observations require a determined spatial and a temporal reference basis, i.e., a reference point (selected in an area that can be considered fixed) and a reference time (i.e., the master acquisition, as already described) must be selected, and all deformations must be intended with respect to that point and that time. The number of independent double-differences that can be formed from the original phase observations is equal to $(N-1)\times(P-1)$, for N InSAR acquisitions and P PSs. By maximization of the ensemble coherence w.r.t. the double difference phase and the phases related to the modeled height and velocity, we are able to measure the height and speed of deformation on each network's branches. After finding these parameters (i.e., height of scatterers and speed of deformation), the only remaining task is the proper phase unwrapping of the phase, that can be carried out by using one of

the many well-known unwrapping methodologies (see e.g., [20, 28, 29]). Densification of PSs is then performed by iterating previous steps.

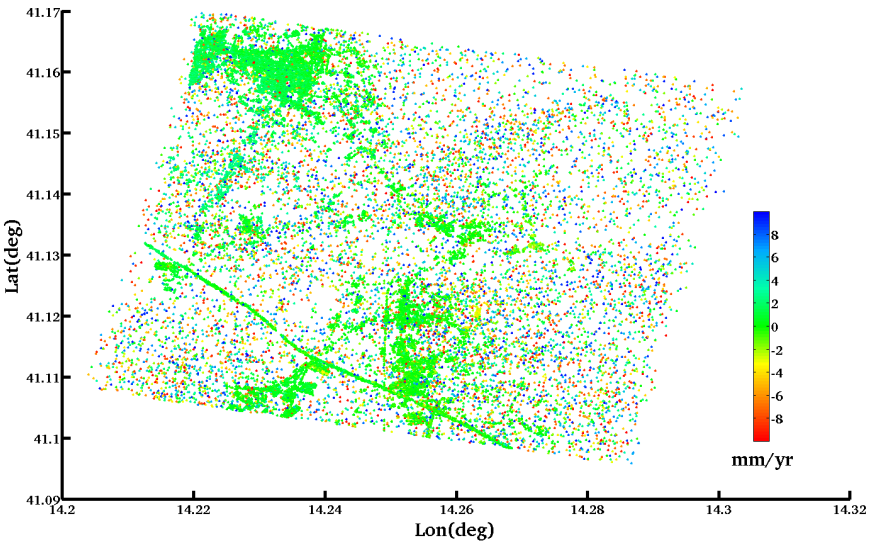

Figure 4.4. Mean surface displacement velocity of the study area based on 25 InSAR images from 2011 02 24 until 2015 03 23, estimated with PSI methodology. Colored pixels are PSs, white pixels are not PSs and no velocity estimation is obtained for them.

4.4 Results and discussions

The study area has already gone under PSI analysis with low resolution images like ERS, and ENVISAT-ASAR from PlaneTek Company before [30]. However, with these sensors, the number of PSs in the study area is too small. For instance, on the bridge over the Volturno river considered in this study, with ERS data sets from 1992 till 2000, in the ascending mode, only two, and, with the descending mode, only one PS have been selected. With ENVISAT-ASAR sensor in temporal baseline of 2003-2010, in the ascending mode six, and in the descending mode only one PS have been selected. Therefore, the need for using high resolution imageries for

a better understanding of the deformation phenomena on the bridge is obvious.

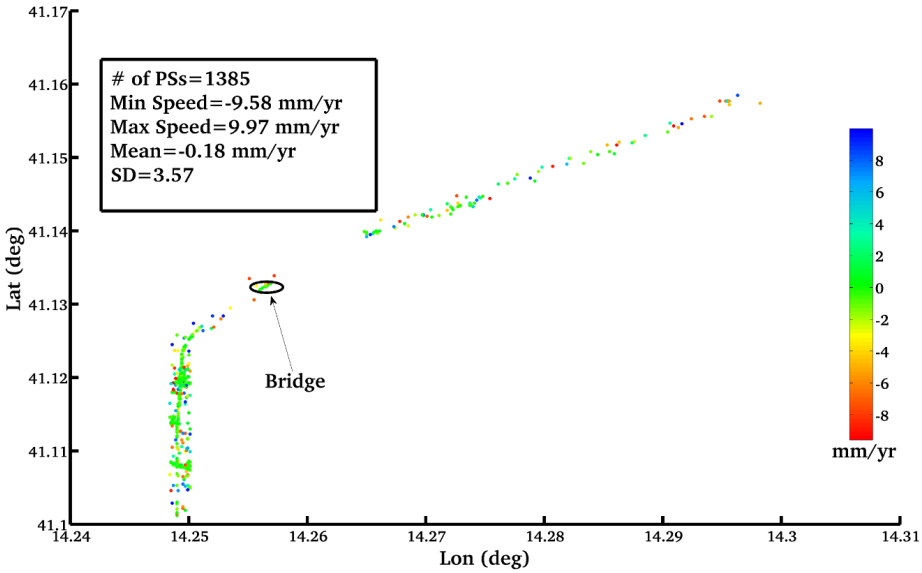

Figure 4.5. Mean displacement rates of PSs on the railways and statistics of these PSs.

Accordingly, 25 InSAR images of Cosmo-SkyMed sensors at descending mode of HIMAGE/Stripmap were used for our study area, (it is depicted in Figure 4.1 as a red rectangle). Images are acquired in HH polarization, right looking, X-band (EM wavelength: 3.1228 cm), with mean incident angle of 26.60 degrees (incidence angle at the center of the transmitted beam). Data cover a temporal baseline between February 24 2011 till March 23 2015. We examine this stack of images to identify the number of scatterers on the ground that consistently/permanently show stable reflections back to the satellite on all images in the temporal baseline. With PSI analysis historical motion of the permanent scatterers on the ground was determined. Image of 5th June of 2013 (see Table 4.1) has been selected as master image (see Figure 4.3), and radar images were cropped in an area as big as $7.5 \times 7.5 km^2$, centered at the bridge on Volturno river (Figure 4.2). Then, 24 differential interferograms have been

Table 4.1. Available CSK data sets (from same sensor of $CSK4\_HI01$), and perpendicular, temporal, and Doppler baselines. Image number 14 (20130605) has been selected as the master image.

Nr	Acquisition Date	Perpendicular Baselines [m]	Temporal Baselines [day]	Doppler Baselines [Hz]
1	20110224	252.5	-832	-46.33
2	20110429	1153.2	-768	-10.17
3	20110718	750.6	-688	-36.37
4	20110819	363.4	-656	-99.25
5	20111022	332.5	-592	-129.48
6	20111225	1472.9	-528	-72.75
7	20120211	438	-480	-65.46
8	20120415	479.8	-416	-11.3
9	20120618	113.1	-352	41.41
10	20120805	115.9	-304	-64.35
11	20121008	-623.4	-240	4.25
12	20121211	840	-176	-13.34
13	20130213	-196	-112	-7.23
15	20130402	-314.1	-64	-35.47
14	**20130605**	**0**	**0**	**0**
16	20130925	353.8	112	-2.92
17	20131128	-28.5	176	30.86
18	20140115	-266.4	224	15.19
19	20140405	-1034	304	43.15
20	20140421	-1102.5	320	-29.88
21	20140827	-263.7	448	3.75
22	20141030	-900	512	-8.94
23	20141115	-841.4	528	32.66
24	20141217	-201.3	560	6.62
25	20150323	348.6	656	69.11

generated w.r.t. the master image. With Cosmo-SkyMed data sets and for the selected study area of $7.5 \times 7.5 km^2$, more than 190,000 PSs including some on the railways, and some on the bridge of Volturno River have been selected. The average velocity and ensemble coherence are as big as -1.8 mm/yr (for whole area) and 73%, respectively, and the density of selected PSs is equal to 3378 PSs/km^2 for entire area.

The majority of the PSs are from man-made structures like houses, highways, railways, etc. Figure 4.4 shows the mean velocity (deformation rate) of the Earth surface's in the study area. As it is clear from this Figure, man-made structures like highways, railways, and cities are designated as potential permanent radar wave reflectors (i.e. PSs).

Figure 4.5 shows the selected scatterers (PSs) on the railways and the bridge itself. It turns out that they are 1385 and, as it is obvious from this Figure, most of them are stable. Minimum and maximum displacement rates are $-9.58 mm/yr$ and $9.97 mm/yr$, respectively, but these high values are only obtained in some isolated points (blue or red dots in Figure 4.5), surrounded by points for which the displacements rates are much lower (green dots), so that they are probably due to phase noise. The velocity averaged over all the 1385 PSs is $1.8 mm/yr$, and standard deviation (SD) is $3.57 mm/yr$. The PSs on the railways and nearby structures are selected in the GIS environment manually. Thirty of these PSs are located on the bridge, and they are highlighted by an ellipse in Figure 4.5. For these 30 PSs, minimum and maximum velocities of -0.9 and 0.05 mm/yr have been observed, respectively, with average of $-0.3 mm/yr$ and $SD = 0.3 mm/yr$.

For each PS, not only the displacement rate, but also the entire time series of displacements is obtained. For instance, in Figure 4.6, the time series of six PSs, out of the 30 PSs on the bridge, have been depicted. This allows us a deeper analysis of the bridge displacements' behaviour. In particular, we have compared the time variations of the bridge displacement (or deformation) with the time variations of temperature in the same considered area and in the same time interval.

In Figure 4.7, the green line shows the deformation time series averaged over the 30 PSs' on the bridge, and the blue points represent the temperature in the Neapolitan metropolitan area [31]. As it is obvious from this Figure, the deformation and temperature time series are very similar, demonstrating that most of the deformation is cyclical and it is

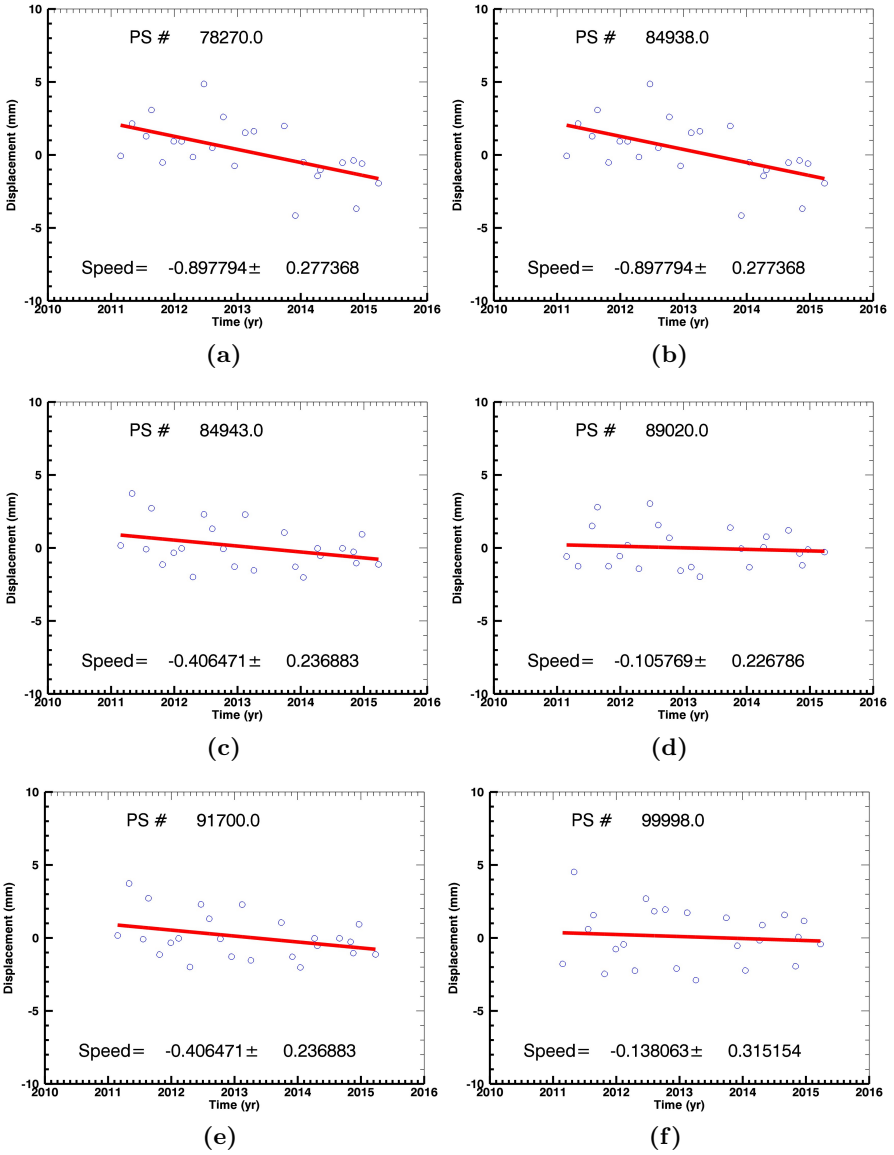

Figure 4.6. Six time series of the surface deformations on the Volturno river's bridge (speed is expressed in $mm/year$) .

related to the temperature seasonal changes in winter and summer time (thie behavior can be explained by assuming that detected deformations are due to thermal dilation). Decreasing of the detected amplitude of deformation yearly cycle in 2013 and 2014 (Figure 4.7) is actually probably due to undersampling: in fact, it is related to the smaller number of the images in that period, with no image acquired in summer 2013 and only one (at the end of August) in summer 2014.

In conclusion, comparison of average PSs time series on the bridge with thermal data shows that most of the Line Of Sight (LOS) changes are due to the periodical variations of the temperature (i.e., winter and summer), with cyclical, seasonal deformations superimposed to a small rate of deformation of -0.30 mm/yr.

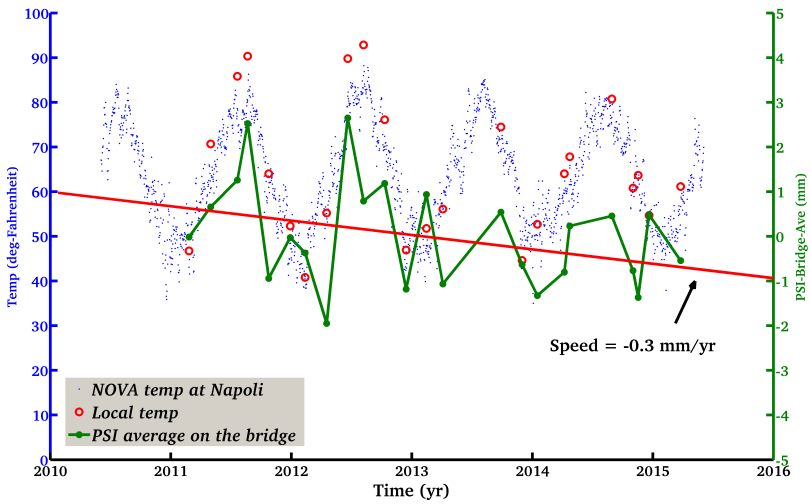

Figure 4.7. Bridge deformation as a function of time (green points) compared with temperature of the Neapolitan metropolitan area as a function of time (blue points). Bridge deformation is obtained by averaging the values of all the 30 PSs on the bridge, and temperature data are taken from NOAA (for more details see [32]).

Accordingly, use of higher resolution imageries like CSK and TSX to have better and smooth time series has been demonstrated by using CSK data. However, combination of descending mode with ascending mode imageries to achieve the deformation rates in both vertical and horizontal directions (i.e., not only along the line of sight), continuous GPS deformation monitoring, corner reflector establishment, and leveling data might improve understanding of this study area. Comparison of SBAS methodology with the employed PSI technique also would be helpful and is the subject of current study.

4.5 Summary

Monitoring stability of the railways in Campania (Italy) by using the DInSAR technique is the subject of this work. We analyzed 25 X-band radar images of Cosmo-SkyMed satellite from Campania during the time span of February 24 2011 till March 23 2015, with InSAR and PSI methodologies. We have focused our analysis on a railway, and in particular on a railway bridge over the Volturno river, at Triflisco. The use of higher resolution imagery has allowed us obtaining a much larger number of persistent scatterers with respect to previous studies on the same area, so that more reliable results have been obtained. In the average of more than 190 thousands of persistent scatterers, velocities and ensemble coherence are as big as -1.8 mm/yr and 73% respectively.

On the bridge over the Volturno river (the main target), 30 PSs have been obtained. In the studied time series, minimum velocity of -0.9 and maximum of 0.05 mm/yr with average of -0.3 mm/yr and $SD = 0.3mm/yr$ have been observed, demonstrating very stable and safe conditions on the bridge.

Comparison of average PSs time series on the bridge with thermal data shows that most of the Line Of Sight (LOS) changes are due to the periodical, seasonal variations of the temperature (i.e., winter and summer).

In conclusion, our five year spanning SAR data analysis shows the importance and capability of InSAR/PSI methodologies for deformation rate

evaluation. However, an important finding of our study is that the availability of high-resolution X-band SAR data is a key need for interferometric approaches if we want to monitor deformation rates of infrastructures. In addition, it should be pointed out that, due to limited (re)visiting and SAR viewing geometries, PSI is not always capable of providing a real-time warning of possible critical deformations that might be occurred on the railways, so that for this latter aim PSI should be employed in conjunction with other monitoring methods.

Bibliography

[1] Usai S., and Hanssen R. (1997) - Long time scale INSAR by means of high coherence features, *in: Third ERS SymposiumSpace at the Service of our Environment,* Florence, Italy, 1721 March 1997, pp. 225228.

[2] Ferretti A., Prati C., and Rocca F. (1999a) - Multibaseline InSAR DEM Reconstruction: The Wavelet Approach, *IEEE Transactions on Geoscience and Remote Sensing,* 37 (2):705715.

[3] Ferretti A., Prati C., and Rocca F. (1999b) - Non-Uniform Motion Monitoring Using the Permanent Scatterers Technique, *in: Second International Workshop on ERS SAR Interferometry, 'FRINGE99',* Liege, Belgium, 1012 Nov 1999, pp. 16, ESA.

[4] Ferretti A., Prati C., Rocca F. (2000) - Nonlinear subsidence rate estimation using permanent scatterers in differential SAR interferometry. *IEEE Transactions on Geoscience and Remote Sensing.* 38, 22022212.

[5] Ferretti A., Prati C., and Rocca F. (2001) - Permanent scatterers in SAR interferometry. *IEEE Transactions on Geoscience and Remote Sensing* 39(1), 820.

[6] Berardino P., Fornaro G., Lanari R., Sansosti E. (2002) - A new algorithm for surface deformation monitoring based on small baseline differential SAR interferograms. *IEEE Transactions on Geoscience and Remote Sensing.* 40, 23752383.

[7] Lanari R., Mora O., Manunta M., Mallorqui J.J., Berardino P., Sansosti E. (2004) - A small-baseline approach for investigating deformations on full-resolution differential SAR interferograms. *IEEE Transactions on Geoscience and Remote Sensing.* 42, 13771386.

[8] Pepe A., Manunta M., Mazzarella G., Lanari R. (2007) - A spacetime minimum cost flow phase unwrapping algorithm for the generation of persistent scatterers deformation time-series. *In Proceedings of the IEEE International Geoscience and Remote Sensing Symposium (IGARSS 2007),* Barcelona, Spain, 2328 July 2007.

[9] Pepe A., Sansosti E., Berardino P., Lanari R. (2005) - On the generation of ERS/ENVISAT D-InSAR time-series via the SBAS technique. *IEEE Geoscience and Remote Sensing Letters.* 2, 265269.

[10] Pepe A., Berardino P., Bonano M., Euillades L.D., Lanari R., Sansosti E. (2011) - SBAS-based satellite orbit correction for the generation of DInSAR time-series: Application to RADARSAT-1 data. *IEEE Transactions on Geoscience and Remote Sensing.* 49, 51505165.

[11] Perissin, D., Ferretti, A., Piantanida, R., Piccagli, D., Prati, C., Rocca, F., Rucci, A., and de Zan, F. (2008) - Repeat-pass SAR interferometry with partially coherent targets. *In Fifth International Workshop on ERS/Envisat SAR Interferometry, 'FRINGE07',* Frascati, Italy, 26 Nov-30 Nov 2007, page 6 pp.

[12] Mora O., Mallorqui J.J., Broquetas A. (2003) - Linear and nonlinear terrain deformation maps from a reduced set of interferometric SAR images. *IEEE Transactions on Geoscience and Remote Sensing.* 41, 22432253.

[13] Hooper A., Zebker H., Segall P., Kampes B. (2004) A new method for measuring deformation on volcanoes and other natural terrains using InSAR persistent scatterers. *Geophysical Research Letters.,* 31, doi: 10.1029/2004GL021737.

[14] Crosetto M., Crippa B., Biescas E. (2005) - Early detection and in-depth analysis of deformation phenomena by radar interferometry. *Engineering Geology,* 79, 8191.

[15] Werner C., Wegmller U., Strozzi T., Wiesmann A. (2003) - Interferometric point target analysis for deformation mapping. *In Proceedings of the 2003 Geoscience and Remote Sensing Symposium (IGARSS 2003),* Toulouse, France, 2125 July 2003.

[16] Crosetto M., Biescas E., Duro J., Closa J., Arnaud A. (2008) - Generation of advanced ERS and ENVISAT interferometric SAR products using the stable point network technique. *Photogrammetric Engineering and Remote Sensing,* 74, 443450.

[17] Hooper, A. (2008) - A multi-temporal InSAR method incorporating both persistent scatterer and small baseline approaches. *Geophysical Research Letters,* 35:L16302.

[18] Ferretti A., Fumagalli A., Novali F., Prati C., Rocca F., Rucci A. (2011) - A new algorithm for processing interferometric data-stacks: SqueeSAR. *IEEE Transactions on Geoscience and Remote Sensing.* 49, 34603470.

[19] Navarro-Sanchez V.D., Lopez-Sanchez J.M. (2013) - Spatial adaptive speckle filtering driven by temporal polarimetric statistics and its application to PSI. *IEEE Transactions on Geoscience and Remote Sensing.* 99, 110.

[20] Kampes B. (2005) - *Displacement parameter estimation using permanent scatterer interferometry.* Ph.D. thesis, Technische Universiteit Delft.

[21] Ketelaar V.B.H. Gini (2009) - *Satellite Radar Interferometry,* Remote Sensing and Digital Image Processing 14, Springer Business Media B.V.

[22] Calcaterra M., Parise M., Blonda P. (2003) - Combining historical and geological data for the assessment of the landslide hazard: a case study from Campania, Italy. *Nat. Hazards Earth Systems.* Science.,3(1/2), pp. 316.

[23] Vilardo G., Ventura G., Terranova C., Matano F., and Nardo S. (2009) - Ground deformation due to tectonic, hydrothermal, gravity, hydrogeological, and anthropic processes in the Campania Region (Southern Italy) from Permanent Scatterers Synthetic Aperture Radar Interferometry, *Remote Sensing and Environments.,* 113 (1), 197212.

[24] Del Prete, S., Di Crescenzo S., Santangelo N., Santo A. (2010) - Collapse sinkholes in Campania (southern Italy): predisposing factors, genetic hypothesis and susceptibility. *Geomorphology,* 54, pp. 259284.

[25] Blonda P., Parise M., Reichenbach P., Guzzetti F. (2012) - Rock-fall hazard assessment along a road in the Sorrento Peninsula, Campania, southern Italy. *Nat Hazards,* 61(1), pp. 187201.

[26] Parise M., Vennari C., A. (2013) - Chronological catalogue of sinkhole in ITALY: The first step toward a real evaluation of the sinkhole hazard. *13th sinkhole conference NCKRI SYMPOSIUM* 2013.

[27] Ferretti A., Prati C., Rocca F. (2001) - Permanent scatterers in SAR interferometry. *IEEE Transactions on Geoscience and Remote Sensing.* 39, 820.

[28] Usai S., and Klees R. (1999a) - On the interferometric characteristics of anthropogenic features, *in: International Geoscience and Remote Sensing Symposium,* Hamburg, Germany, 28 June2 July 1999.

[29] Usai S., and Klees R. (1999b) - SAR Interferometry on Very Long Time Scale: A Study of the Interferometric Characteristics Of Man-Made Features, *IEEE Transactions on Geoscience and Remote Sensing,* 37(4):21182123.

[30] Nutricato R., Nitti D.O. (2015) - *Processamento di scene Cosmo-SkyMed con tecniche di interferometria differenziale PS.* Internal report in Italian.

[31] http://www7.ncdc.noaa.gov/CDO/cdoselect.cmd?datasetabbv=GSOD & countryabbv= & georegionabbv=.

[32] Poreh D., Iodice A., Riccio D., Ruello G., railways' stability observed in Campania (Italy) by InSAR data, *European journal of remote sensing*, Volume 49, 2016, pp. 417-431.

Chapter 5

Pol-SARAS: a fully polarimetric SAR raw signal simulator for extended scenes

In this chapter we present a new Synthetic Aperture Radar (SAR) raw signal simulator, which is able to simultaneously generate the raw signals of the different polarimetric channels of a polarimetric SAR system in such a way that the correct covariance matrix is obtained for the final images. Extended natural scenes, dominated by surface scattering, are considered. A fast Fourier-domain approach is used for the generation of raw signals. Presentation of theory is supplemented by meaningful experimental results, including a comparison of simulations with real polarimetric scattering data.

5.1 Introduction

In recent years, Synthetic Aperture Radar (SAR) Polarimetry has been successfully applied to soil moisture retrieval, forest monitoring, change detection and marine applications [1]. Therefore, a polarimetric SAR raw signal simulator, based on a sound physical electromagnetic scattering model, would be certainly useful for mission planning, algorithm develop-

ment and testing, and prediction of suitability of the system to different applications. This simulator should be able to consider extended scenes, whose macroscopic topography is possibly prescribed by an external Digital Elevation Model (DEM), and to account for terrain roughness and soil electromagnetic parameters. Simulated raw signals of the different polarimetric channels, when focused via standard SAR processing algorithms, should lead to a realistic polarimetric covariance (or coherency) matrix.

An efficient simulator with many of the above cited features, called SARAS [2]-[5], is actually available in literature: in fact, it is a model-based raw signal simulator that, among other system characteristics, also accounts for the transmitting and receiving polarizations. However, it can only simulate one polarimetric channel at a time, with the result that data of different channels turn out to be independent. Accordingly, although the correct relations between polarimetric channels' powers are obtained, the covariance (or coherency) matrix of the final images is not realistic.

Here we present a new improved version of that simulator that is able to simultaneously produce the raw signals of the different polarimetric channels in such a way to obtain the correct covariance or coherence matrixes on the final images. We call this new simulator "Pol-SARAS", to indicate that it is the polarimetric version of the available SARAS. In the following, we will refer to the simulator for the classical stripmap acquisition mode [2], but the same modifications also apply to simulators for spotlight [3] and hybrid [4] acquisition modes, as well as to the one accounting for platform trajectory deviations [5]. In addition, we here only consider surface scattering, but, due to the modular structure of the simulator, also other scattering mechanisms (volumetric, double bounce) can be included, if reliable models are available.

It must be recalled that polarimetric SAR simulators including also other scattering mechanisms are available in literature, see [6, 7]. However, the simulator described in [6] is tailored for specific man-made targets, such as ships, tanks, etc., and it cannot be used to simulate extended natural scenes. On the other hand, the simulator described in [7] can consider a wide range of natural and man-made scenarios with different scattering mechanisms. However, with that method, computation of the raw signal is necessarily in time domain, and hence it is very computationally demanding. Conversely, our proposed simulator can handle extended scenes

(although, for the moment being, just including surface scattering), and it uses a fast Fourier-domain approach to generate raw signals, so that it is very efficient. In addition, at variance with available literature, we validate our simulator by using also a comparison with actual polarimetric scattering data. Apart from [6, 7], at the best of our knowledge the several SAR simulators available in literature (see [31]-[36], just to mention some of the most recent ones) are either not efficient, in the sense that they use time-consuming numerical scattering computation and/or time-domain raw-signal evaluation; or not polarimetric, in the sense that they are not able to simultaneously generate all the different polarimetric channels with a realistic polarimetric covariance matrix.

This chapter is organized as follows. In Section (5.2), the rationale of the proposed simulator is presented, highlighting similarities and differences with the available SARAS. Section (5.3) is dedicated to the description of simulation results. In particular, in Section (5.3.1) the polarimetric coherency matrixes obtained from simulated data are compared with those obtained by available approximate analytical scattering models; in Section (5.3.2) a comparison between simulated and real polarimetric data is presented; and in Section (5.3.3) potential applications of the simulator to soil moisture retrieval and terrain azimuth slope retrieval from SAR polarimetric data are illustrated. Finally, summary remarks are reported in Section (5.4).

5.2 Polarimetric simulation rationale

Similarly to the SARAS simulator [2]-[5], the presented Pol-SARAS simulator employs a procedure consisting of two main stages. In the first stage, given the illumination geometry and the scene description, the scene reflectivity map (more properly, backscattering map), i.e., the ratio between backscattered and incident field components, is evaluated, thanks to appropriate direct models. At variance with SARAS, the three reflectivity maps corresponding to the HH, HV and VV polarizations are here computed at the same time. In the second stage, the HH, HV and VV SAR raw signals are computed via a superposition integral in which each reflectivity map is weighted by the SAR system two-dimensional ($2D$) impulse response, computed from system data. This general simulator architecture

is schematized in Figure 5.1, and the geometry of the problem is depicted in Figure 5.2. It is assumed that the sensor moves at constant velocity v along a straight-line nominal trajectory and it transmits chirp pulses at regularly spaced times t_n; note that, in the employed reference system, x is the azimuth coordinate, while y and r are the ground range and slant range coordinates, respectively.

The simulator input data can be grouped into three classes: scene data, illumination data, and system data. Scene data include:

(i) The scene height profile $z(x, y)$, which can be either provided by an external digital elevation model (DEM), possibly resampled to fit the employed reference system (see [24]), or selected by the user among a set of canonical ones (plane, pyramid, cone);

(ii) Small-scale, $p(x, y)$, and large-scale, $\sigma(x, y)$, roughness parameter maps, (see below), which can be either provided by an external file or set by the user (in the latter case, the user can subdivide the scene in different rectangular patches, specifying the parameters of each of them);

(iii) Complex dielectric permittivity map $\epsilon(x, y)$, which again can be either provided by an external file or set by the user (in the latter case, the user can subdivide the scene in different rectangular patches, specifying the permittivity of each of them).

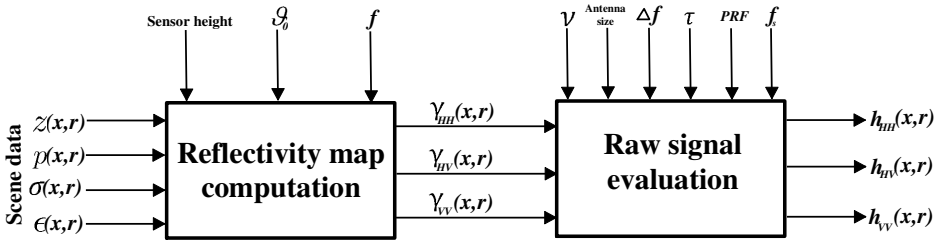

Figure 5.1. General architecture of the simulator

Illumination data include sensor height, scene-center look angle ϑ_0, and carrier frequency f.

Finally, system data include, for non-squinted stripmap mode, sensor velocity v, antenna size, chirp bandwidth Δf and duration τ, pulse repetition frequency (PRF) and received pulse sampling frequency f_s. Additional parameters (e.g., squint angle, length of the trajectory flight portion used to acquire the raw data, etc.) are required for other acquisition modes [2]-[5].

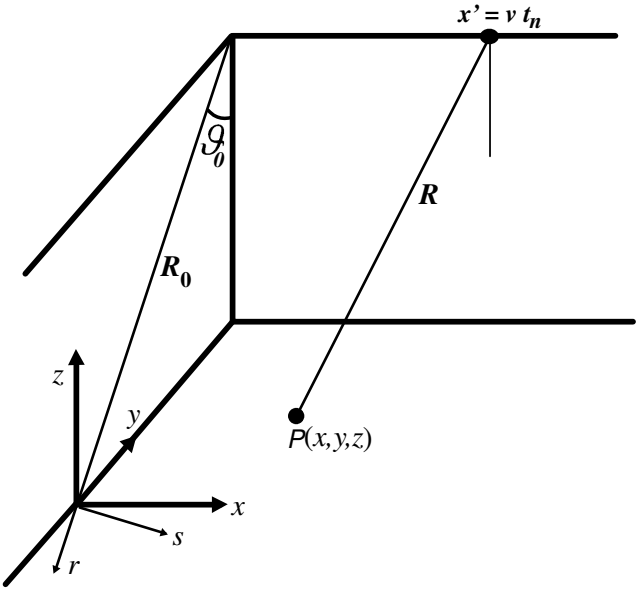

Figure 5.2. Geometry of the problem and coordinate reference systems

5.2.1 Computation of reflectivity maps

Let us now analyze the first simulation stage (i.e., reflectivity maps computation) in detail. Similarly to the usual SARAS simulator, the surface macroscopic height profile is approximated by rectangular rough facets, large with respect to wavelength but smaller than SAR system resolution. The facet roughness is here referred to as small-scale roughness, and it is modelled as a stochastic process, whose statistics are prescribed by the set of input parameters $p(x, y)$. Although different choices are possible, in this chapter we use a zero-mean band-limited $2D$ fractional Brownian

motion (fBm) isotropic stochastic process [11], characterized by its Hurst coefficient H_t (with $0 < H_t < 1$) and its topothesy T, so that $p \equiv (H_t, T)$. A notable property of the fBm process is that its power spectral density presents a power-law behavior and is given by

$$W(k) = S_0 k^{-2-2H_t}, \tag{5.1}$$

where $k = \sqrt{k_x^2 + k_y^2}$ is the (isotropic) roughness wavenumber, and S_0 is related to T and H_t as reported in [11].

At variance with the existing SARAS, here, to model the large-scale roughness, we add zero-mean random deviations to the facets' azimuth and range slopes prescribed by the macroscopic height profile. Therefore, we can express the azimuth and range slopes, a and b, of each facet as:

$$\begin{cases} a = a_0 + \delta a \quad (i), \\ b = b_0 + \delta b \quad (ii), \end{cases} \tag{5.2}$$

where a_0 and b_0 are the azimuth and range slopes prescribed by the input macroscopic height profile $z(x, y)$, and the slope deviations δa and δb are zero-mean jointly Gaussian random variables with joint probability distribution function (pdf) given by

$$p(\delta a, \delta b) = \frac{1}{2\pi\sigma_x\sigma_y\sqrt{1-\rho^2}} exp\Big[- \frac{1}{1-\rho^2}\Big(\frac{\delta a^2}{2\sigma_x^2} + \frac{\delta b^2}{2\sigma_y^2} - \frac{\rho\delta a\delta b}{\sigma_x\sigma_y}\Big)\Big], \tag{5.3}$$

wherein $\sigma \equiv (\sigma_x, \sigma_y, \rho)$ are the input large-scale roughness parameters, σ_x and σ_y being azimuth and range slope standard deviations, respectively, and ρ the correlation coefficient. A usual choice is $\sigma_x = \sigma_y = \sigma, \rho = 0$, so that the slope deviations δa and δb are independent identically distributed Gaussian random variables, and large-scale roughness is isotropic. However, with a different choice it is also possible to explore the effects of large-scale roughness anisotropy. Realizations of random variables δa and δb according to the pdf (5.3) are generated by using a standard algorithm [25].

From input illumination data (in particular, ϑ_0 and sensor height) and from $z(x, y)$, by using simple geometric relations, the facet center slant

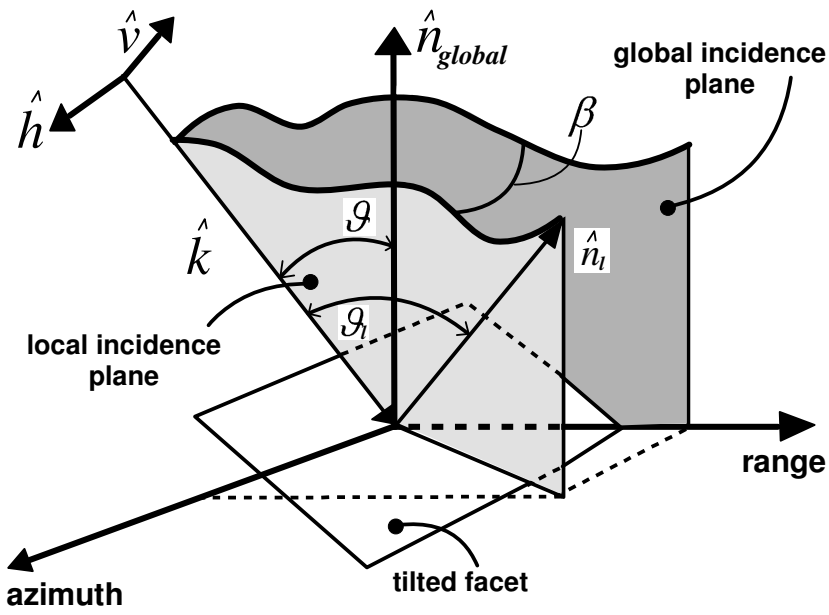

Figure 5.3. Facet geometry

range r and look angle ϑ (see Figure 5.3) can be easily computed. Once facet slopes a and b and look angle ϑ are known, it is possible to compute the local incidence angle ϑ_l, i.e., the angle formed by the look direction unit vector $\hat{k}$ and the local normal unit vector of the facet $\hat{n}_l$ (see Figure 5.3); in addition, it is possible to evaluate the orientation (or rotation) angle β, i.e., the angle between global and local incidence planes (i.e., between the vertical plane including the look direction, and the plane perpendicular to the facet and including the look direction, see Figure 5.3). In particular, being

$$\hat{k} = -sin\vartheta\ \hat{i}_y - cos\vartheta\ \hat{i}_z, \tag{5.4}$$

and

$$\hat{n}_l = -\frac{a}{\sqrt{1+a^2+b^2}}\hat{i}_x - \frac{b}{\sqrt{1+a^2+b^2}}\hat{i}_y + \frac{1}{\sqrt{1+a^2+b^2}}\hat{i}_z, \tag{5.5}$$

we can write

$$\begin{cases} \vartheta_l = cos^{-1}(\hat{k} \cdot \hat{n}_l) & (i), \\ \beta = sin^{-1}(\hat{h} \cdot \hat{\vartheta}_l) & (ii), \end{cases} \tag{5.6}$$

where

$$\begin{cases} \hat{h}_l &= \frac{\hat{k} \times \hat{n}_l}{|\hat{k} \times \hat{n}_l|}, \\ \hat{v}_l &= \hat{h}_l \times \hat{k}, \\ \hat{h} &= \frac{\hat{k} \times \hat{n}}{|\hat{k} \times \hat{n}|}, \\ \hat{v} &= \hat{h} \times \hat{k}, \end{cases} \tag{5.7}$$

At this point, we have all the elements to evaluate the reflectivity $\gamma(x, r)$ of each facet, which can be computed by using the Small Perturbation Method (SPM) or the Physical Optics (PO), according to the facet's small-scale roughness and incidence angle [8]: SPM holds for low roughness and intermediate incidence angles, PO for high roughness or small incidence angles. In particular, $\gamma(x, r)$ can be expressed as [8]-[10]

$$\gamma_{pq}(x, r; \vartheta_l, \beta, \epsilon) = \chi_{pq}(x, r, \vartheta_l, \beta, \epsilon) w(x, r; \vartheta_l), \tag{5.8}$$

where p and q are the polarizations of the incident and scattered field, respectively, and stand for H (horizontal) or V (vertical); ϵ is the input complex permittivity; χ_{pq} are the elements of the 2×2 matrix

$$\underline{\underline{\chi}}(\vartheta_l, \beta, \epsilon) = \underline{\underline{R}}_2(\beta) \begin{pmatrix} F_H(\vartheta_l, \epsilon) & 0 \\ 0 & F_V(\vartheta_l, \epsilon) \end{pmatrix} \underline{\underline{R}}_2^{-1}(\beta), \tag{5.9}$$

with

$$\underline{\underline{R}}_2(\beta) = \begin{pmatrix} cos\beta & sin\beta \\ -sin\beta & cos\beta \end{pmatrix}, \tag{5.10}$$

being the 2×2 unitary rotation matrix, and F_H and F_V either the Bragg (if SPM is used) or the Fresnel (if PO is used) coefficients for H and V polarization, respectively [8]-[10]; and $w(\vartheta_l)$ is a polarization-independent zero-mean circular complex Gaussian random variable, whose

variance $\langle |w(\vartheta_l)|^2 \rangle$ depends on small-scale roughness. The expression of this dependence changes according to the employed scattering and small-scale (i.e., facet's) roughness models [8]-[11]: in the SPM case, it is proportional to the power spectral density $W(\cdot)$ of the facet's roughness, given by (5.1) for fBm roughness, and it can be expressed as

$$\langle |w(\vartheta_l)|^2 \rangle = k^4 cos^4 \vartheta_l W(2ksin\vartheta_l), \tag{5.11}$$

where k is the electromagnetic wavenumber. In the PO case, the expression of $\langle |w(\vartheta_l)|^2 \rangle$ is related to the Kirchhoff scattering integral and depends on the model considered for the observed surface [10, 11]. In this chapter, with the exception mentioned at the end of this section, we will focus on SPM, but analogous results can be obtained by using PO. Realization of the complex random variable $w(\vartheta_l)$ is obtained by generating two independent realizations of a zero-mean Gaussian random variable, used as real and imaginary parts of $w(\vartheta_l)$.

It is important to note that, at variance with the already available SARAS simulator, in this updated version the three polarimetric channels HH, VV and $HV = VH$ (HV and VH coincide, due to reciprocity) are simulated at the same time, and the same realization of the random variable $w(\vartheta_l)$ is used for all the three channels. This ensures that the polarimetric channels are not independent; on the other hand, the randomness of the facet slopes (which causes the randomness of ϑ_l and β) introduces a decorrelation among the different channels. By performing different simulations with a varying number of facets per pixel (from 1×1 to 20×20) we verified that practically the same correlations among polarimetric channels are obtained by using any number of facets per pixel equal to at least 2×2. In addition, in Sections (5.3.1) and (5.3.2) we will show that the statistics of the simulated polarimetric channels are in agreement both with the ones predicted by theory and with the ones of real polarimetric data, so that we can conclude that if at least 2×2 facets per pixel are used, the correct joint statistics among polarimetric channels are obtained.

A few last remarks on the practical implementation of the above-described procedure are now due. First of all, since input data maps are sampled on a uniformly spaced grid over the x, y plane, the output reflectivity maps turn out to be sampled on a grid which is uniformly

spaced with respect to x, but non-uniformly spaced with respect to slant range r. To recover reflectivity maps sampled on a fully uniformly spaced grid also on the x, r plane, to be used in the second simulation stage, the same efficient range interpolation procedure, based on a "power-sharing" approach, used in SARAS, is here implemented.

In addition, the same efficient ray-tracing recursive algorithm employed in SARAS [2] is here implemented to identify shadowed facets, whose reflectivity is set to zero. Note that for areas in back-slope near to shadow condition, the local incidence angle is very large, so that both SPM and PO are not appropriate. However, in this case the backscattering is so low that even very large relative errors on the scattered field are of little practical importance, since in real data those areas are dominated by thermal noise.

Finally, particular care must be dedicated to areas near to layover conditions, for which local incidence angle is small. In fact, as already noted, SPM does not hold for small incidence angles, for which PO is more appropriate. In particular, (5.11) diverges as the incidence angle tends to zero; on the other hand, the PO value of $\langle |w(0)|^2 \rangle$ for fBm surfaces is available [11], and we call it w_{max}. Indeed, small incidence angles are of no interest in the SAR case, except occasionally for areas near to layover conditions. To allow dealing also with such areas without complicating the simulation algorithm, in the proposed Pol-SARAS simulator we use (5.11) if it leads to a value smaller than w_{max}, otherwise we let $\langle |w(\vartheta_l)|^2 \rangle = w_{max}$. This latter condition only occurs for incidence angles smaller than a threshold depending on small-scale roughness parameters T and H_t. For values of roughness parameters usually exhibited by actual natural surfaces [11], the threshold angle ranges from very few degrees to about 20 degrees.

The entire procedure described in this sub-section is summarized in the block scheme of Figure 5.4, where the parts that are new with respect to the SARAS simulator are evidenced by red dashed boxes.

5.2.2 Evaluation of raw signals

Let us now consider the second simulation stage, in which the raw signals for the different polarization channels are obtained from the corresponding reflectivity maps by weighting them with the SAR system impulse

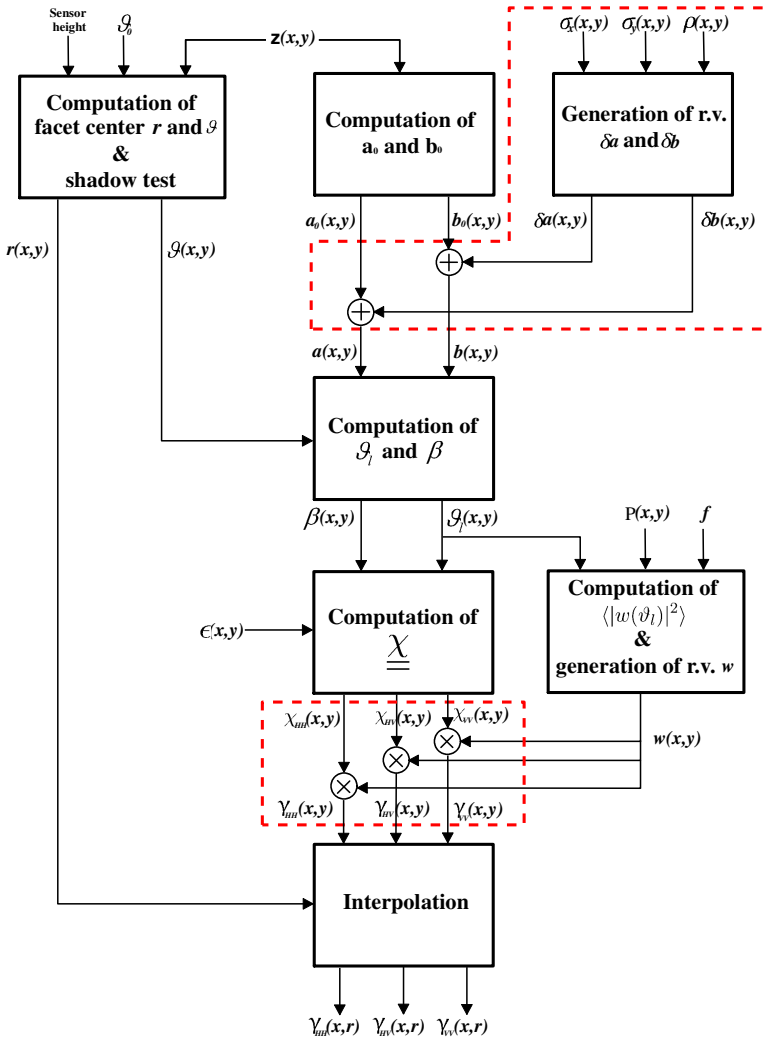

Figure 5.4. Block scheme of the reflectivity map computation; "r.v." stands for "random variable". Novelties with respect to the SARAS simulator are evidenced by red dashed boxes.

response. Apart from the fact that this operation is performed three times (one for each polarimetric channel), this simulation stage is not changed with respect to the SARAS case. Therefore, we here just briefly recall the procedure employed for the stripmap acquisition mode [2]. However, a similar efficient $2D$ Fourier-domain approach can be used also for the spotlight case [3] and/or in the case of sufficiently regular deviations with respect to the nominal trajectory [5]. In addition, a mixed time- and Fourier-domain approach can be used for the hybrid (i.e., sliding spotlight) acquisition mode and/or in presence of general trajectory deviations [4].

A chirp modulation of the transmitted pulse is assumed. The expression of the SAR raw signal is the following [2]:

$$h_{pq}(x', r') = \iint \gamma_{pq}(x, r) g(x' - x, r' - r; r) dx dr, \tag{5.12}$$

wherein

$$g(x'-x, r'-r; r) = e^{-j\frac{4\pi}{\lambda}\Delta R} e^{-j\frac{4\pi}{\lambda}\frac{\Delta f/f}{c\tau}(r'-r-\Delta R)^2} u^2\Big(\frac{x'-x}{X}\Big) rect\Big[\frac{r'-r-\Delta R}{c\tau/2}\Big], \tag{5.13}$$

is the SAR system impulse response, and

$$\Delta R = \Delta R(x' - x; r) = R - r = \sqrt{r^2 + (x' - x)^2} - r, \tag{5.14}$$

In eqs.(5.12 - 5.14), see also Figure 5.2,

- x' is the azimuth coordinate of the antenna position,
- R is the distance from the antenna to the generic point of the scene,
- R_0 is the distance from the line of flight to the centre of the scene,
- c is the speed of light,
- $u(\cdot)$ is the azimuth illumination diagram of the real antenna over the ground,
- $X = \lambda R_0/L$ is the real antenna azimuth footprint (we assume that $u(\cdot)$ is negligible when the absolute value of its argument is larger than $1/2$, and that it is an even function),

- λ is the electromagnetic wavelength and L is the azimuth dimension of the real antenna,
- $rect[t/T]$ is the standard rectangular window function, i.e., $rect[t/T] = 1$ if $|t| \leq T/2$, otherwise $rect[t/T] = 0$,
- r' is $c/2$ times the time elapsed from each pulse transmission,

and all other symbols have been already defined.

If we ignore the r-dependence of $g(\cdot)$, i.e., if we let $r = R_0$ in (5.14), then (5.12) is easily recognised as the $2D$ convolution between γ and g, that can be efficiently performed in the $2D$ Fourier transformed domain. Even considering the r-dependence, (5.12) can be efficiently computed in the $2D$ Fourier transformed domain: in fact, by using the stationary phase method it can be shown [2] that the Fourier Transform (FT) of eq.(5.12) is

$$H_{pq}(\xi,\eta) = G_0(\xi,\eta)\Gamma_{pq}\Big[\xi, \eta\Omega(\xi) + \mu(\xi)\Big], \tag{5.15}$$

where $H_{pq}(\xi,\eta)$ is the FT of $h_{pq}(x,r)$, $\Gamma_{pq}(\xi,\eta)$ is the FT of $\gamma_{pq}(x,r)$,

$$G_0(\xi,\eta) = e^{j\frac{\eta^2}{4b}} e^{j\frac{\xi^2}{4a(1+\eta\lambda/4\pi)}} rect\Big[\frac{\eta}{2bc\tau/2}\Big] u^2\Big(\frac{\xi}{2aX}\Big), \tag{5.16}$$

is the FT of $g(x'-x, r'-r; r = R_0)$,

$$\begin{cases} a = \frac{2\pi}{\lambda R_0} & (i), \\ b = \frac{4\pi}{\lambda}\frac{\Delta f/f}{c\tau} & (ii), \end{cases} \tag{5.17}$$

and the functions

$$\begin{cases} \mu(\xi) = \frac{\xi^2}{4aR_0} & (i), \\ \Omega(\xi) = 1 - \frac{\xi^2}{4aR_0}\frac{\lambda}{4\pi} & (ii), \end{cases} \tag{5.18}$$

account for the r-space-variant characteristics of the SAR system, i.e., for the r-dependence of $g(\cdot)$.

Eq.(5.15) suggests that the stripmap SAR raw signal simulation can be performed as shown in the flow chart in Figure 5.5[2,4], where the "Grid

Deformation" block performs an interpolation in the Fourier domain, to obtain the desired values $\Gamma_{pq}\Big[\xi, \eta\Omega(\xi) + \mu(\xi)\Big]$ from the available ones $\Gamma_{pq}(\xi, \eta)$.

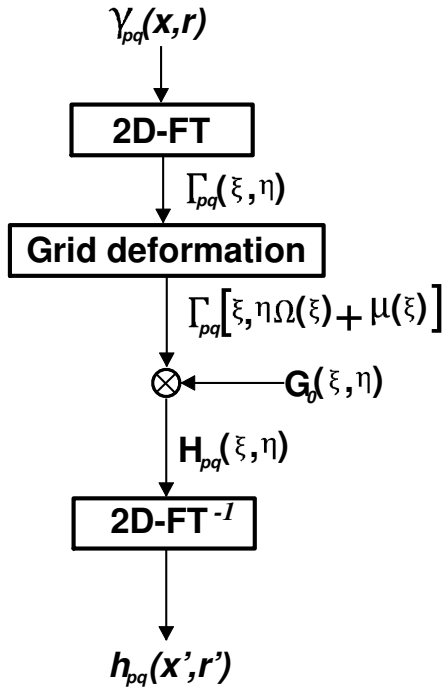

Figure 5.5. Flow chart of SAR raw signal simulation, given a reflectivity map.

This is the method employed in the stripmap SAR raw signal simulator presented in [2], and also adopted here. Use of efficient Fast Fourier Transform (FFT) algorithms leads, in the case of extended scenes, to a processing time of different orders of magnitude smaller than the one required by a time domain simulation directly based on (5.12-5.14).

Once the raw signals for the different polarization channels are simulated, they can be focused with usual processing algorithms employed for actual SAR data, in order to obtain the final single-look complex (SLC) images.

Table 5.1. Simulation parameters for flat and Vesuvius scenes

Sensor height	[km]	200
Sensor velocity	[km/s]	0.9
Azimuth antenna size	[m]	1.5
Range antenna size	[m]	8.5
Carrier frequency	[GHz]	1.28
Pulse duration	[μs]	1.9
Sampling rate	[MHz]	14
PRF	[Hz]	350
Doppler centroid	[Hz]	0
Chirp bandwidth	[MHz]	14
Topothesy	[m]	0.001
Hurst coefficient		0.8

5.3 Simulation results

In this Section, we illustrate some results obtained by using the PolSARAS simulator described in the previous Section. The presented experiments are aimed at:

- verifying the consistency of the proposed simulator by comparing the polarimetric coherency matrixes obtained from simulated data with those obtained by available approximate analytical scattering models;
- validating the proposed simulator by comparing simulated and actual polarimetric SAR data;
- illustrating the potentiality of the proposed simulator in some SAR polarimetry applications, and in particular in developing and verifying algorithms to retrieve soil moisture or terrain azimuth slope from SAR polarimetric data.

5.3.1 Comparison with theoretical models

As a first consistency check, let us verify that polarimetric data obtained from simulated raw signals are in agreement with those obtained by available approximate analytical scattering models.

The most popular approximate analytical scattering models are PO and SPM. However, they are not able to take into account crosspolarization and depolarization effects, which are essential for the modeling of polarimetric scattering from rough surfaces (i.e., according to PO and SPM, the HV backscattering is zero and HH and VV channels are perfectly correlated, both results being in disagreement with experiments) [9]. To properly deal with these effects, second-order SPM and Integral Equation Methods (IEM) have been proposed, but their formulations are not in closed form, and they are too involved to be used efficiently in practice [9, 10]. Two-scale models have been introduced, which, even if able to extend the SPM validity significantly, still do not take into account the depolarization effect [10]. In [13], the model called "X-Bragg" has been presented to take care of the cross-polarization and depolarization effects. However, X-Bragg uses an unrealistic uniform distribution to model the β angle (see Figure 5.3), and completely ignores the random variation of the local incidence angle due to (large-scale) roughness. The Polarimetric Two-Scale Model (PTSM) solves the aforementioned problems [9], taking into account both cross-polarization and depolarization effects properly: as demonstrated by meaningful experiments, in low-vegetated areas it presents a better agreement with measured data [9]. In the PTSM model, the SPM expressions of the covariance matrix elements of tilted rough facets are evaluated; in particular, they are expressed in terms of the facets' slopes a and b (along azimuth and range directions, respectively) by using the well-known relations linking them to β and ϑ_l [9]. Finally, the entries of the covariance matrix of the overall surface are obtained by averaging the corresponding tilted facets expressions over a and b, after a second order expansion around $a = 0$ and $b = 0$. Therefore, some similarity between the PTSM and the Pol-SARAS approach may be noted. However, relevant differences are also present between the two approaches. In particular, in PTSM a second order expansion around $a = 0$ and $b = 0$ is performed, in order to analytically evaluate the covariance matrix elements. Conversely, in Pol-SARAS this approximation is not needed, because the covariance matrix elements can be directly estimated on the polarimetric SAR images obtained by focusing simulated raw signals. In addition, at variance with PTSM, Pol-SARAS can account for anisotropic behaviors of the imaged surfaces, see eq. (5.3), as

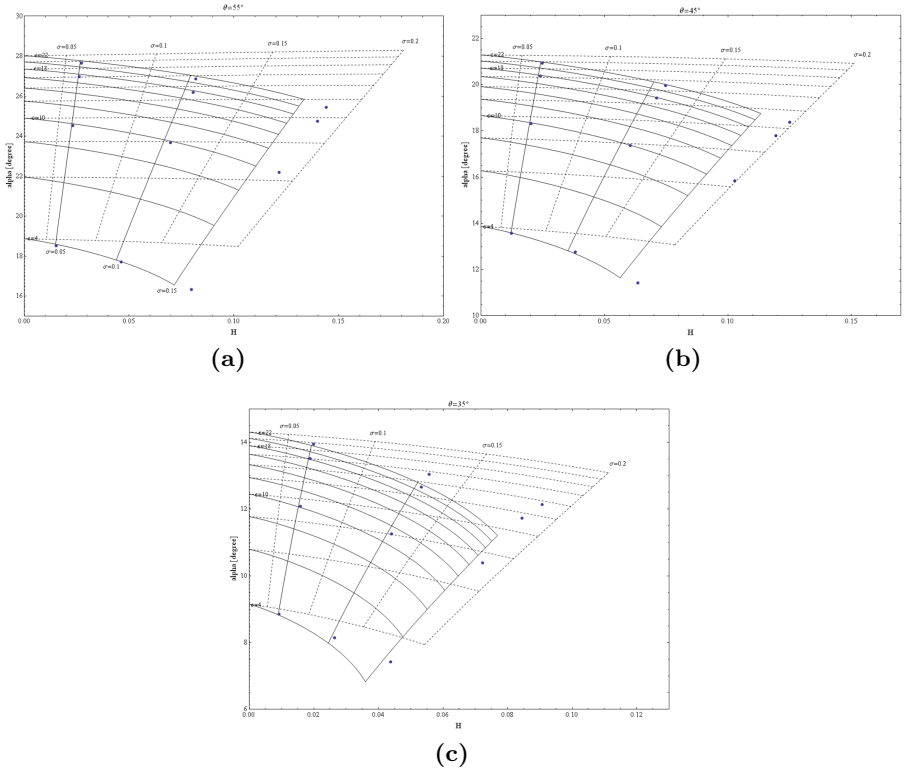

Figure 5.6. H-α chart obtained via PTSM (solid line), and X-Bragg (dashed line), compared with Pol-SARAS results (blue points) for (a) $\vartheta = 55°$, (b) $\vartheta = 45°$, and (c) $\vartheta = 35°$. Pol-SARAS points are evaluated for ϵ equal to 4, 10, 18, and 22, and for σ equal to 0.05, 0.1, and 0.15.

we will show in detail in Section (5.3.3). Summarizing, in general, the Pol-SARAS approach is expected to present a wider validity range than that of theoretical approximated models, and a meaningful comparison can be performed only with X-Bragg and PTSM models, which account for cross-polarization and depolarization.

X-Bragg and PTSM models allow computation of covariance or coherency matrixes [1], that have six independent elements, of which three are real and three are complex. Accordingly, comparison of coherency matrixes obtained by Pol-SARAS, X-Bragg and PTSM would amount to

Table 5.2. Comparision with measured data, surface 1-wet

surface 1-wet L-band (1.5 GHz) $\epsilon = 15.57$; $\sigma = 0.17$				
θ (degrees)	*crosspol* (ground)	*copol* (ground)	*crosspol* (Pol-SARAS)	*copol* (Pol-SARAS)
30°	-21	-2	-21.2	-2.3
40°	-19	-4	-20.1	-3.6
50°	-20	-6	-19.0	-5.6
60°	-19	-9	-18.1	-8.2

compare three sets of nine real numbers each, and this should be repeated for several combinations of input parameters (ϵ, small-scale and large-scale roughness parameters, ϑ, f). A simpler comparison can be obtained by considering proper combinations of the coherency matrix elements. A convenient choice is to use entropy and alpha angle [1]: entropy H is related to the eigenvalues of the coherency matrix and mainly measures the degree of randomness of the scattering process, whereas the angle α is related to eigenvalues and eigenvectors of coherency matrix, and it also depends on the kind of scattering mechanism, i.e., single, double, or volumetric scattering. In presence of surface scattering only, H and α mainly depend on ϑ, ϵ and large-scale roughness σ only. More details about H and α can be found in [1, 13, 18, 19]. In [9], PTSM and X-Bragg were compared with respect to H-α charts, i.e., graphs in which, for a fixed incidence angle, H and α values obtained in correspondence of ϵ and σ pairs are plotted (see Figure 5.6). Here we use the same graphs to compare Pol-SARAS with both PTSM and X-Bragg. To evaluate H and α, we simulated the polarimetric channels' raw signals giving as an input to the simulator a flat DEM (i.e., no macroscopic topography) and using the parameters of Table 5.1, with 3×7 facets per pixel in azimuth and range, respectively. Once the three channels' complex images were obtained via standard focusing of the raw data, we evaluated H and α from coherency matrix elements obtained by averaging over 8×8 pixel windows; we then applied a further average of the obtained H and α values over the whole scene. Finally, we repeated the simulations for several values of ϵ and σ, in order to obtain the desired graphs.

In Figure 5.6 a comparison between PTSM and X-Bragg H-α graph predictions and Pol-SARAS based ones is provided for three different val-

Table 5.3. Comparision with measured data, surface 1-dry

surface 1-dry L-band (1.5 GHz) $\epsilon = 7.99$; $\sigma = 0.17$

θ (degrees)	*crosspol* (ground)	*copol* (ground)	*crosspol* (Pol-SARAS)	*copol* (Pol-SARAS)
30°	-19	-1	-22.4	-2.0
40°	-19	-3	-21.3	-3.1
50°	-20	-4	-19.9	-4.8
60°	-18	-6	-19.0	-6.9

ues of the look angle. PTSM and X-Bragg graphs are evaluated assuming the same surface parameters used for the simulations. For large look angles, i.e., 55° and 45°, PTSM predictions are in good agreement with Pol-SARAS results, even if, for increasing values of σ, entropy tends to be slightly underestimated and α slightly overestimated by PTSM. Conversely, as expected, Pol-SARAS results significantly depart from X-Bragg predictions, which tend to underestimate H and overestimate α. For smaller values of the look angle (e.g. 35°, see Figure 5.6c) also the PTSM graph departs from the Pol-SARAS one, for σ larger than about 0.1. In particular, α and H tend to be underestimated by PTSM. Indeed, in this case the PTSM is close to the limit of its validity range, especially for increasing values of H.

By summarizing, we can state that the Pol-SARAS results are in reasonable agreement with the ones of the PTSM method, at least within the range of validity of the latter.

5.3.2 Comparison with measured data

Comparison of polarimetric data obtained from simulated and real data is now in order. To perform a meaningful comparison, real SAR polarimetric data should be available for a scene for which a DEM is available, as well as the maps of permittivity and small- and large-scale soil roughness (i.e., all the simulator input scene data). Unfortunately, while DEMs are available for most part of the world, permittivity and roughness maps are seldom, if not never, available. That is why quantitative comparisons between simulated and real SAR data are very seldom reported in literature. Here, we circumvent this problem in two ways: in one approach, we make reference to polarimetric scatterometer real data relative to a

small bare-soil flat area for which in situ measurements of surface permittivity and roughness are available; alternatively, in order to consider real SAR polarimetric data, we use for comparison purposes a combination of polarimetric channels that, in case of bare soils, only depends on topography, and is independent of surface permittivity and roughness (namely, the combination synthesizing the argument of correlation among right-handed and left-handed circular polarizations [20]), so that the correct knowledge of these input data is not critical.

With regard to the first approach, we compare simulation results with data acquired by the University of Michigan's LCX POLARSCAT [9, 22], which provides measured values of the polarimetric normalized radar cross section (NRCS) for HH, VV, and HV channels. At the same time of scatterometer acquisitions, also in situ measurements of soil parameters were performed [22]. This allows for comparing the measured values of the NRCSs with those obtained providing these parameters as input to Pol-SARAS. In particular, here we consider the case of L-band data and moderate soil roughness, i.e., POLARSCAT data relevant to the slightly rough bare soil surfaces 1 of [22]. For this surface, unfortunately, large-scale roughness was not measured, and only the standard deviation over $1-m$ long profiles s is available: in particular, for the considered surface we have $ks = 0.16$. Hence, for simulation purposes we fixed ϵ to the value measured in the top $4-cm$ soil layer: in particular, surface 1 was monitored in presence of two different moisture conditions, corresponding to two different values of ϵ. With regard to the large-scale roughness, we fixed its value to 0.17, i.e., the average value obtained via PTSM-based retrieval for different incidence angles and for the two moisture conditions: PTSM-retrieved large-scale roughness for surface 1 may be found in [9].

In Table 5.2 and Table 5.3 we present the results obtained for wet and dry soil-moisture states, respectively. In particular, we report the values (in dB) of copolarized ($copol$) and crosspolarized ($crosspol$) ratios measured by the scatterometer, along with those predicted by the simulations. The latter are defined as follows:

$$\begin{cases} copol &= \frac{\langle |i_{HH}|^2 \rangle}{\langle |i_{VV}|^2 \rangle}, \\ crosspol &= \frac{\langle |i_{HV}|^2 \rangle}{\langle |i_{VV}|^2 \rangle}, \end{cases} \tag{5.19}$$

where i_{pq} is the focused complex image relevant to the pq polarimetric channel. The parameters of Table 5.1 were used for simulations, apart from the carrier frequency that was set to $1.5GHz$, to match it with the scatterometer one. For ϵ and σ, the values used in the simulations are reported in the first row of Table 5.2 and Table 5.3. We note that the absolute difference between scatterometer and Pol-SARAS *copol* ratio values is at most $1dB$, i.e., comparable with POLARSCAT measurement precision of $\pm 0.4dB$ [22]. With regard to the *crosspol* ratio, for the wet case the maximum absolute difference is $1.1dB$, whereas for the dry case for an incidence angle of $30°$ the absolute difference is $3.4dB$ and for $40°$ is $2.3dB$. However, for larger incidence angles ($50°$ and $60°$) the absolute difference is less than $1dB$. These results confirm the validity of the proposed simulator, which is able to provide results in reasonable agreement with real data for a wide range of incidence angles and soil surface parameters.

Let us now move to the second approach, in order to directly compare simulated and real SAR polarimetric images of an area with significant topography. We here use May 1998 NASA/JPL AIRSAR L-band polarimetric data of Camp Roberts, CA, for which a DEM is also available [26]. Main AIRSAR system and acquisition data are listed in Table 5.4, and they have been used also as inputs of our simulator, together with the scene parameters also listed in Table 5.4. Since, as usual, permittivity and roughness maps of the imaged area are not available, for comparison purposes we use a combination of polarimetric channels that, at least for bare soils, is only dependent on topography, and, in particular, mainly on the mean terrain azimuth slope within each SAR resolution cell. This combination is [20]-[27]

$$I_2 = arctan\Big(\frac{4Re\langle(i_{HH} - i_{VV})i_{HV}^*\rangle}{4\langle|i_{HV}|^2\rangle - \langle|i_{HH} - i_{VV}|^2\rangle}\Big), \tag{5.20}$$

We used 2×2 facets per pixel in our simulations, and we computed averages in (5.20) by using 2×36 (range $\times$ azimuth) pixel windows on SAR images obtained from both real and simulated raw signals, so obtaining a final pixel spacing of about $20m \times 20m$. I_2 images obtained from real and simulated raw signals are shown in Figure 5.7a and 5.7b, respectively, and in Figure 5.7c the RGB false-color Pauli decomposition [1] of the real data is displayed. In the latter, $\sqrt{2\langle|i_{HH}|^2\rangle}$ is loaded on the green band,

Table 5.4. Simulation parameters for Camp Roberts AIRSAR data

Sensor height	[km]	7.6813
Sensor velocity	[km/s]	0.4323
Look angle	[degree]	44.8
Azimuth antenna size	[m]	3
Range antenna size	[m]	0.8
Carrier frequency	[GHz]	1.2
Pulse duration	[μs]	10
Sampling rate	[MHz]	45
PRF	[Hz]	840.3
Doppler centroid	[Hz]	0
Chirp bandwidth	[MHz]	14
Topothesy	[m]	0.001
Hurst coefficient		0.8
Permittivity (ϵ)		22

$\sqrt{\langle|i_{HH}+i_{VV}|^2\rangle/2}$ is loaded on the red band, and $\sqrt{\langle|i_{HH}-i_{VV}|^2\rangle/2}$ on the blue band, and all three bands are normalized with respect to $\sqrt{\langle|i_{HH}|^2\rangle+\langle|i_{VV}|^2\rangle+2\langle|i_{HV}|^2\rangle}$: with this representation, the red band is mainly associated with the surface scattering contribution, the green band to the volume scattering contribution, and the blue band to double bounce [1]. Visually, there is a reasonable agreement between real and simulated I_2 images, but the former is clearly noisier than the latter. This is due to two factors: first of all, I_2 is quite sensitive to thermal noise (due to the presence of the *crosspol* power at the denominator of (5.20) and to the correlation at the numerator of (5.20) [20]-[27]), which we have not included in the simulation, since the thermal noise level is not known; secondly, some parts of the imaged scene are covered with rather dense vegetation, as indicated by the green/blue areas of the Pauli-decomposition image (volumetric scattering due to tree foliage and branches, and double scattering due to trunk-ground reflections), and in such areas I_2 is not dependent only on topography, but also on the spatially-varying vegetation properties, which again are not included in the simulation (and anyway are not known). In order to perform a quantitative comparison, we considered three regions in the scene: a favorable one (indicated by a yellow polygon in Figure 5.7c), in which surface scattering is the dominant mechanism; an intermediate one (indicated by a blue polygon in Figure 5.7c),

in which surface scattering is mixed with the other mechanisms; and an unfavorable one (indicated by a green polygon in Figure 5.7c), in which volume and double scattering dominate. Mean values and standard deviations of real and simulated I_2 are reported in Table 5.5 for each of the three regions and for three values of the large-scale roughness parameter σ employed as simulator inputs. A reasonable agreement between real and simulated data is obtained for the mean values of I_2 in both the favorable ("yellow") and the intermediate ("blue") regions, whereas, as expected, a poor agreement is obtained in the unfavorable ("green") area. It can be also noted that, for the simulated data, in all regions I_2 mean values decrease (in modulus) as σ increases. Finally, confirming the result of the qualitative visual inspection, standard deviations on simulated data are smaller than those on real data, and this difference is more evident in the "green" area. This is in agreement with the explanation we have given above for the noisier look of I_2 real image. In conclusion, we can state that I_2 images obtained from real and simulated data are in good agreement in the areas where surface scattering is significant. This is further confirmed by the comparison of histograms of real and simulated I_2 images, shown in Figure 5.8a and 5.8b, respectively, for the "yellow" region.

5.3.3 Usefulness of the simulator in some applications

In this Sub-section, we present some simulation results illustrating the potentiality of the proposed simulator in some applications of SAR polarimetry. Let us first consider soil moisture retrieval, which is one of the main applications of fully polarimetric SAR data [1, 8, 9, 12, 13, 14, 15, 16, 17]. In fact, availability of different polarimetric channels, combined with the use of scattering models, in principle allows independently retrieving the different parameters on which backscattering depends (soil moisture, surface roughness, vegetation density and shape). In particular, some of the employed models also take into account the presence of double bounce and volumetric scattering mechanisms, to consider the presence of vegetation [14, 16, 17]. However, here we focus on the methods tailored for bare or little vegetated soils, which only need modeling of the surface scattering component [8, 9, 12, 13], because this is the case of interest for Pol-SARAS simulations. Some of these methods ([8, 9, 13]) try to define appropriate

Table 5.5. Comparison of I_2 (in radians) from actual and simulated data for the three Regions Of Interest (ROI) of Figure 5.7

	YELLOW ROI		BLUE ROI		GREEN ROI	
	Mean value	Standard deviation	Mean value	Standard deviation	Mean value	Standard deviation
Actual SAR data	1.78	1.49	1.71	1.37	-0.89	1.86
Simulated $\sigma = 0.1$	1.87	1.07	1.90	1.07	-1.81	0.79
Simulated $\sigma = 0.15$	1.82	1.15	1.81	1.18	-1.76	0.86
Simulated $\sigma = 0.2$	1.62	1.36	1.64	1.39	-1.72	0.91

(a)

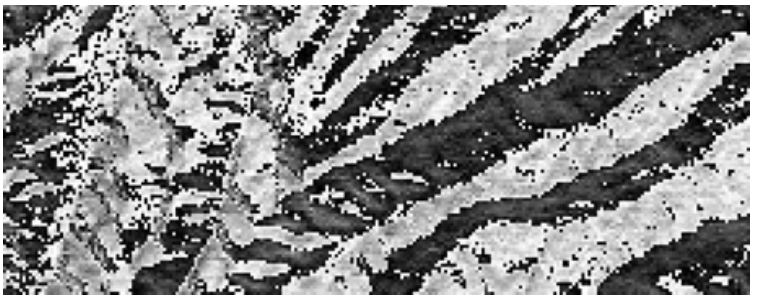

(b)

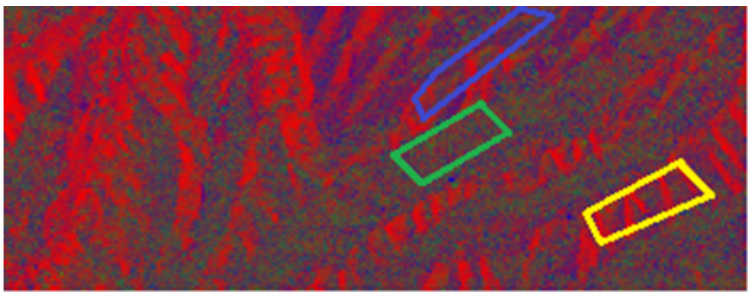

(c)

Figure 5.7. I_2 images obtained from (a) real and (b) simulated polarimetric SAR data ($\sigma = 0.15$), and (c) Pauli RGB decomposition. Yellow, green and blue boxes encircle the three regions of interest (ROI) of Table 5.5 and Table 5.6.

combinations of the polarimetric channels chosen in such a way to be dependent on the minimum number of physical parameters of the observed scene: in the ideal case, they should be a function of the soil dielectric

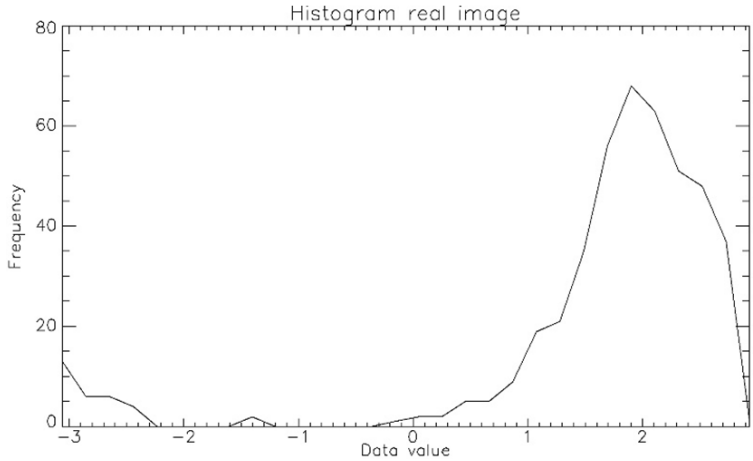

(a)

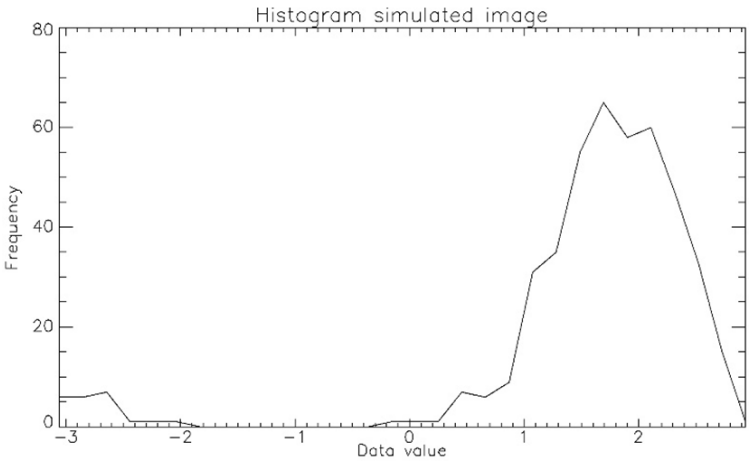

(b)

Figure 5.8. Histogram of I_2 (in radians) values in the "yellow" region of Figure 5.7, obtained from (a) real and (b) simulated data.

permittivity (and hence soil moisture) only; however, in practice, they also depend on the macroscopic roughness of the surface. In particular, in [8, 9], look-up tables based on PTSM *copol-crosspol* and *copol-corr* graphs are used for the estimation of soil moisture in presence of bare soil or low

vegetation cover. The *copol* and *crosspol* ratios are defined in (5.19), and the correlation is defined as:

$$corr = \frac{\langle |i_{HH} i_{VV}^*| \rangle}{\sqrt{\langle |i_{HH}|^2 \rangle \langle |i_{VV}|^2 \rangle}}, \tag{5.21}$$

For PTSM, the dependence on small-scale-roughness parameters cancels out in the ratios in (5.19) and (5.21), so that these ratios only depend on the large-scale-roughness σ and on the relative dielectric permittivity ϵ. This is exploited in [9] to devise a method for the estimation of ϵ from measured polarimetric data: the obtained estimates can be used for the estimation of the volumetric soil moisture, via appropriate mixing models [9]. In particular, in [9] a method based on the evaluation of the *copol-crosspol* graphs is used, whereas in [8] the use of *copol-corr* graphs is proposed, too. One enters the graphs with *copol* and *crosspol* ratios (or *copol* ratio and correlation coefficient) obtained from SAR data and reads the retrieved values of ϵ and σ on the graphs (of course, this can be done automatically by a computer program).

Since, as already discussed, Pol-SARAS simulations have a wider range of validity than PTSM, they provide the possibility to generate graphs that are not subject to PTSM approximations. In the following, we discuss how the proposed simulator can be used to obtain the abovementioned graphs.

To evaluate the quantities in (5.19) and (5.21), we used the same simulated images of Section (5.3.1). Once the three channels' images were obtained, we evaluated the quantities in (5.19) and (5.21) using a multilook of 8×8 pixels and then averaging over the whole scene, as discussed in Section (5.3.1) Finally, we repeated the simulations for several values of ϵ and σ, in order to obtain the *copol-crosspol* and *copol-corr* graphs. In Figure 5.9 the graphs obtained for a look angle of 45° are reported. Similar results are obtained for look angles of 35° and 55°. The behavior of the graphs matches with PTSM theoretical expectations, at least in the considered range of ϵ and σ values [8, 9]. However, the presented graphs are expected to provide a range of validity wider than the PTSM-based ones, especially for small look angles.

A unique characteristic of the Pol-SARAS simulator is the possibility to account for anisotropic features of terrain roughness. Indeed, in the simulator it is possible to set two different values for the standard devia-

tion of the facets' slopes in range and azimuth directions, i.e., $\sigma_x \neq \sigma_y$, see Section (5.3.1). This possibility is particularly interesting in case of agricultural applications, where harvesting and vegetation growth can easily impose anisotropy on soil shape. The results for this case are shown in Figure 5.10. The simulation parameters are those of Table 5.1, with a look angle of 45° and $\epsilon = 4$. In Figure 5.10a, we compare the results obtained for the *copol-crosspol* graph setting $\sigma_x = \sigma_y = \sigma$ (i.e., the isotropic case), with those obtained setting $\sigma_x = 0$ and $\sigma_= \sqrt{2}\sigma$, or $\sigma_y = 0$ and $\sigma_x = \sqrt{2}\sigma$ (i.e., two anisotropic cases). The square root of two factor is used to make the graphs comparable, considering that the overall roughness in the case $\sigma_x = \sigma_y = \sigma$ can be expressed as $\sqrt{\sigma_x^2 + \sigma_y^2} = \sqrt{2}\sigma$. As theoretically expected, since in the absence of azimuth slopes crosspolarization is not present, when $\sigma_x = 0$ (i.e., only range slope, no azimuth slope), the *crosspol* ratio is practically zero independently from σ_y value; however, for visualization purposes in Figure 5.10a we set it to the conventional value of $-60dB$. Moreover, we notice that, in this case, the values of *copol* ratio obtained for a certain σ are slightly lower than those obtained in the case of $\sigma_x = \sigma_y = \sigma$. When $\sigma_y = 0$, (i.e., only azimuth slope, no range slope) the results are somehow inverted. In particular, the range of variation of the *copol* ratio is smaller than for the case $\sigma_x = \sigma_y = \sigma$; conversely, the range of the variation of the *crosspol* ratio is larger than that of the case $\sigma_x = \sigma_y = \sigma$. This is due to the high sensitivity of the *crosspol* ratio to azimuth slopes. From the viewpoint of soil-moisture estimation, i.e., of ϵ estimation, it is evident that in presence of significant anisotropy the estimation is impaired, since ϵ =constant curves are very far from those relevant to the isotropic case, especially when azimuth slopes are negligible with respect to range ones.

In Figure 5.10b the results for the *copol-corr* graph are reported. When σ is equal to zero, *corr* is equal to one and, hence, (1-*corr*) is equal to zero: for visualization purposes in this case, we set (1-*corr*) to the conventional value of $-60dB$. Due to the strong dependence of both *copol* ratio and *corr* on range slopes, we note that the graph relevant to the case of $\sigma_x = 0$, is similar to the one obtained for $\sigma_x = \sigma_y = \sigma$, whereas the graph relevant to the case of $\sigma_y = 0$ significantly departs from the case $\sigma_x = \sigma_y = \sigma$. However, in this case we note that ϵ =constant curves in presence of anisotropy are very close to those relevant to the isotropic case. This

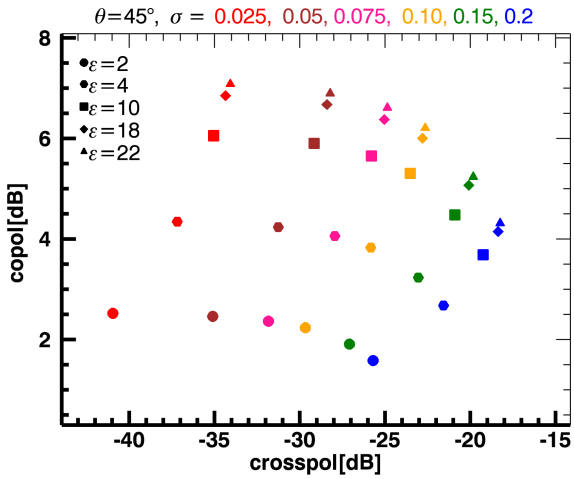

(a)

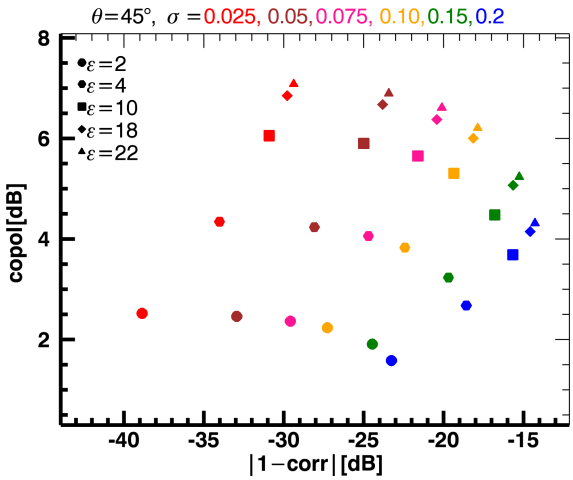

(b)

Figure 5.9. (a) *copol-crosspol* and (b) *copol-corr* graphs for $\theta = 45°$ (for visualization purposes, the absolute value of the *copol* ratio in *dB* is reported on the vertical axis).

is demonstrated by plotting the points relevant to different values of ϵ, which highlights how the estimation of ϵ is not significantly affected by anisotropic roughness. This is a very important result, suggesting that the use of *copol-corr* graphs should be preferred for bare soil moisture retrieval, whenever uncontrollable anisotropies may be present in the macroscopic roughness.

Let us now consider another application of SAR polarimetry, i.e., the rotation (or orientation) angle β estimation for the compensation or the estimation of terrain azimuth slope variation [20]. In fact, in [20, 27] it is shown that, if surface scattering dominates and if $|\beta| \leq \pi/4$, the parameter I_2 in (5.20) is equal to 4β , so that it can be used to retrieve β from polarimetric SAR data. Results presented in subsection (5.3.2) on simulated polarimetric SAR data of Camp Roberts already visually show that, as expected, and in agreement with real data, I_2 actually is related to the mean of the terrain slope along azimuth in the resolution cell via the rotation (or orientation) angle β (see Figure 5.7). For a quantitative assessment, as "ground truth" for the retrieval of β from SAR data, we computed the β angle for the considered scene from the available DEM (after averaging the latter to obtain the same $20m \times 20m$ pixel spacing of the I_2 maps). Obtained mean β values (computed by restricting β values to the interval $|\beta| \leq \pi/4$) over the three regions of interest selected in subsection (5.3.2) are reported in Table 5.6, together with the mean β values retrieved from real and simulated SAR data via (5.20). With regard to simulated data, we considered different, both isotropic and anisotropic, large-scale roughness conditions. In addition, in Table 5.6 we also report the mean β values retrieved via eq.(5.20) after a 2×2 boxcar smoothing on both real and simulated SAR data. Results of Table 5.6 show that, if no smoothing is applied to SAR data, then:

- β values retrieved from real SAR data are significantly underestimated (in absolute value), and this underestimation is higher on vegetated areas ("green" and "blue" regions);

- β values retrieved from simulated SAR data are also underestimated, but in better agreement to DEM-derived ones with respect to real data estimates; in addition, the underestimation increases as the large-scale roughness increases;

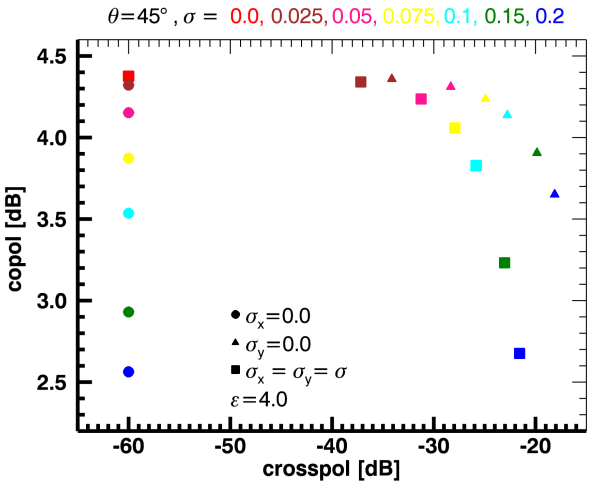

(a)

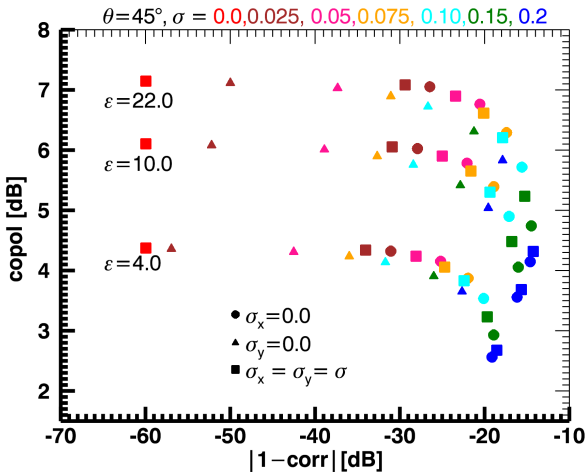

(b)

Figure 5.10. (a) *copol-crosspol* and (b) *copol-corr* graphs in case of anisotropic soil roughness for $\theta = 45°$ (for visualization purposes, the absolute value of the *copol* ratio in dB is reported on the vertical axis).

- when anisotropic large-scale roughness is considered, the underestimation effect due to roughness is much more significant if roughness slopes are along the azimuth direction.

Figure 5.11. Shaded representation of the smoothed LiDAR DEM of the Vesuvius volcano.

However, β estimations after smoothing of polarimetric SAR data are in much better agreement with the DEM-derived ones, and effects of roughness, noise and vegetation are significantly reduced. Also, retrievals from real and simulated data are in very good agreement, thus confirming that differences between real and simulated I_2 images in Figure 5.7 are mainly due to unmodeled noise, see discussion in subsection (5.4.2).

In conclusion, simulated results show that, if the elements of the coherency matrix are obtained by averaging over about 70-80 pixels (which is usually considered sufficient in most applications [1]), even for pure surface scattering, the retrieval of β from SAR polarimetric data may be affected by underestimation due to surface roughness, especially if the latter is prevalently along the azimuth direction. However, this effect is almost completely eliminated if a further 2×2 averaging is performed, so that the overall averaging is over about 300 pixels.

Figure 5.12. Simulated image relevant to the HH channel.

Table 5.6. Mean values of β [rad] retrieved from DEM and from actual and simulated data for the three ROI's of Figure 5.7

	YELLOW ROI		BLUE ROI		GREEN ROI	
	No smoothing	2×2 smoothing	No smoothing	2×2 smoothing	No smoothing	2×2 smoothing
DEM	0.54	0.54	0.57	0.57	-0.54	-0.54
Actual SAR data	0.44	0.56	0.43	0.53	-0.22	-0.47
Simulated $\sigma = 0.025$	0.48	0.52	0.50	0.53	-0.46	-0.48
Simulated $\sigma = 0.1$	0.47	0.51	0.47	0.52	-0.45	-0.47
Simulated $\sigma = 0.2$	0.41	0.49	0.41	0.50	-0.43	-0.47
Simulated $\sigma_x = 0.2, \sigma_y = 0$	0.38	0.49	0.35	0.46	-0.41	-0.48
Simulated $\sigma_x = 0, \sigma_y = 0.2$	0.45	0.49	0.46	0.51	-0.43	-0.44

(a)

(b)

Figure 5.13. Images of (a) entropy and (b) α angle relevant to the Vesuvius simulation.

Finally, to illustrate the application of the presented simulator to the assessment of classification methods based on polarimetric SAR data, and to show the simulator efficiency in terms of processing time, we present a last example regarding a scene with a non-flat DEM, simulated giving as input to Pol-SARAS a one-meter-resolution LiDAR DEM of the volcano Vesuvius, close to Naples, Italy [23]. Since the high-resolution LiDAR DEM is too sensitive to the presence of vegetation and anthropogenic features, a preliminary smoothing step was applied, leading to a final resolution of $5m$. The DEM obtained after the smoothing is shown in Figure 5.11. The simulations were performed using the parameters reported in Table 5.1, with a look angle of $45°$, a relative dielectric constant equal to 4, and conductivity equal to $10^{-3}S/m$. As an example, the HH channel simulated image is reported in Figure 5.12: a multilook with a factor of 2 in range and 16 in azimuth is applied, to obtain an approximately square pixel.

Obtained results are here analyzed in terms of H and α images obtained from the Pol-SARAS simulations. In Figure 5.13, H and α images obtained for $\sigma = 0.1$ are shown. The values of H are low and tend to be

higher in areas of low intensity. The values of α are low in average and tend to increase for increasing values of the local incidence angle, as expected. These observations are confirmed by the $H - \alpha$ scatterplot shown in Figure 5.14, where the zones identified according to the classification scheme proposed in [19] are reported. The graph confirms that most of the points are located in zone 9, i.e., present low values of both entropy and α. Zone 9 is indicative of the presence of surface scattering mechanisms [19].

A few last words on computational complexity and processing time are now due. First of all, it must be noted that computational complexity has not been significantly increased with respect to the non-polarimetric SARAS simulator, so that it is still approximately proportional to $N \times logN$, where N is the number of pixels for the considered scene. In fact, overall computational complexity for the three polarimetric channels is slightly less than three times the one for a single channel (consider that many operations for reflectivity generation are in common for the three channels, which compensates for the fact that generation of random deviations of facets' slopes has been added). In particular, for the Vesuvius scene, with a 5261×1506 pixel raw signal size, on a general purpose PC with an Intel^{TM} Core i7-6700HQ CPU @ 2.60 GHz and a 16 GB RAM, processing time is 47 seconds for SARAS and two minutes and 18 seconds for Pol-SARAS.

5.4 Summary

In this chapter, a fully polarimetirc SAR simulator, which we named Pol-SARAS, has been presented. It is based on the use of sound direct electromagnetic models and it is able to provide as output the simulated raw data of all the three polarization channels in such a way as to obtain the correct covariance or coherence matrixes on the final focused images. At the moment, the proposed simulator takes into account the surface scattering contribution only; however, thanks to the simulator modularity, volumetric and double-bounce contributions can be included to account for vegetation, too, if efficient and accurate models become available. Ac-

tually, several quite accurate vegetation models are already available (see, e.g., [28, 29]), but their efficient implementation in the simulation scheme is not straightforward, and it is left to future work.

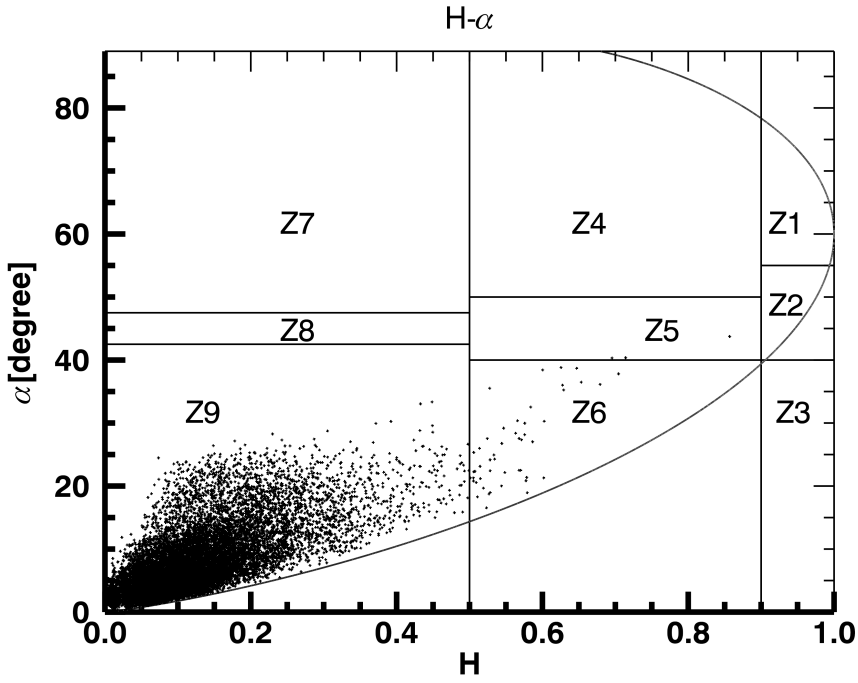

Figure 5.14. Scatterplot of the images in Figure 5.13 represented in the $H - \alpha$ plane partitioned according to the classification scheme proposed in [19].

In addition, we note that also man-made complex targets (for instance, buildings in urban areas) may be considered by the proposed simulator by including them in the DEM (with also an appropriate complex permittivity, see Section 5.3), but only provided that $z(x, y)$ remains single-valued (i.e., two or more facets with the same x, y coordinates and different heights cannot be considered). In addition, multiple bounces between different facets are not considered. For the non-polarimetric SARAS simulator, both limitations can be overcome as described in [30], but that solution cannot be easily extended to the Pol-SARAS case, and this has

not been made for the moment being. Finally, the proposed polarimetric SAR simulation scheme can be applied to time-varying marine scenes by extending the approach described in [37], but this is not straightforward, and has not been implemented for the moment being.

The proposed simulator has been shown to provide results in agreement with what predicted by available theoretical models, at least in the validity ranges of the latter. In addition, polarimetric data obtained from simulated raw signals have been shown to agree with those obtained from a real SAR sensor. Finally, the potentialities of the simulator in support of some practical applications of SAR polarimetry have been investigated. In particular, with regard to soil-moisture retrieval, the possibility to simulate scenes presenting anisotropic macroscopic roughness has been exploited to demonstrate that the use of *copol-corr* look-up tables have to be preferred to *copol-crosspol* ones for the estimation of ϵ, in presence of surfaces that may present an anisotropic roughness. Furthermore, with regard to the rotation (orientation) angle estimation from polarimetric SAR data, presented results show that, to avoid underestimation, sufficiently large windows must be used in computing the coherency matrix elements. Finally, the usefulness of the simulator for the analysis of polarimetric classification schemes has been also discussed: in particular, an example of the application of $H - \alpha$ analysis has been presented.

Bibliography

[1] J. S. Lee and E. Pottier, *Polarimetric Radar Imaging: From Basics to Applications.* Boca Raton, FL, USA: CRC Press, 2009.

[2] G. Franceschetti, M. Migliaccio, D. Riccio, and G. Schirinzi, "SARAS: a synthetic aperture radar (SAR) raw signal simulator", *IEEE Transactions on Geoscience and Remote Sensing.*, vol. 30, no. 1, pp.110 123, Jan. 1992.

[3] S. Cimmino, G. Franceschetti, A. Iodice, D. Riccio, and G. Ruello, "Efficient Spotlight SAR Raw Signal Simulation of Extended Scenes", *IEEE Transactions on Geoscience and Remote Sensing.*, vol. 41, no. 10, pp. 2329- 2337, Oct. 2003.

[4] G. Franceschetti, R. Guida, A. Iodice, D. Riccio, and G. Ruello, "Efficient Simulation of Hybrid Stripmap/Spotlight SAR Raw Signal From Extended Scenes", *IEEE Transactions on Geoscience and Remote Sensing.*, vol. 42, no. 11, pp. 2385-2396, Nov. 2004.

[5] G. Franceschetti, A. Iodice, S. Perna, and D. Riccio, "SAR Sensor Trajectory Deviations: Fourier Domain Formulation and Extended Scene Simulation of Raw Signal", *IEEE Transactions on Geoscience and Remote Sensing.*, vol. 44, no. 9, pp. 2323-2334, Sept. 2006.

[6] G. Margarit, J. J. Mallorqui, J. M. Rius and J. Sanz-Marcos, "On the Usage of GRECOSAR, an Orbital Polarimetric SAR Simulator of Complex Targets, to Vessel Classification Studies," *IEEE Transactions on Geoscience and Remote Sensing.*, vol. 44, no. 12, pp. 3517-3526, Dec. 2006.

[7] F. Xu and Y. Q. Jin, "Imaging Simulation of Polarimetric SAR for a Comprehensive Terrain Scene Using the Mapping and Projection Algorithm," *IEEE Transactions on Geoscience and Remote Sensing.*, vol. 44, no. 11, pp. 3219-3234, Nov. 2006.

[8] A. Iodice, A. Natale, and D. Riccio, "Polarimetric Two-Scale Model for Soil Moisture Retrieval via Dual-Pol HH-VV SAR Data", *IEEE J. Sel. Topics Appl. Earth Observ. Remote Sens.*, vol. 6, no. 3, pp. 1163-1171, June 2013.

[9] A. Iodice, A. Natale, and D. Riccio, "Retrieval of Soil Surface Parameters via a Polarimetric Two-Scale Model", *IEEE Transactions on Geoscience and Remote Sensing.*, vol. 49, no. 7, pp. 2531-2547, July 2011.

[10] F. T. Ulaby, R. K. Moore, and A. K. Fung, *Microwave Remote Sensing: Active and Passive.* Reading, MA, USA: Addison-Wesley, 1982.

[11] G. Franceschetti, A. Iodice, M. Migliaccio, and D. Riccio, Scattering from Natural Rough Surfaces Modeled by Fractional Brownian Motion Two-Dimensional Processes, *IEEE Transactions on Antennas Propag.*, vol. 47, no. 9, pp. 1405-1415, Sept. 1999.

[12] J. Shi, J. Wang, A. Y. Hsu, P. E. ONeill, and E. Engman, "Estimation of bare surface soil moisture and surface roughness parameter using L-band SAR image data," *IEEE Transactions on Geoscience and Remote Sensing.*, vol. 35, no. 5, pp. 12541266, Sep. 1997.

[13] I. Hajnsek, E. Pottier, and S. R. Cloude, "Inversion of surface parameters from polarimetric SAR, *IEEE Transactions on Geoscience and Remote Sensing.*, vol. 41, no. 4, pp. 727744, Apr. 2003.

[14] I. Hajnsek, T. Jagdhuber, H. Schn, and K. P. Papathanassiou, "Potential of estimating soil moisture under vegetation cover by means of PolSAR," *IEEE Transactions on Geoscience and Remote Sensing.*, vol. 47, no. 2, pp. 442454, Feb. 2009.

[15] A. Iodice, A. Natale, and D. Riccio, "Retrieval of soil surface parameters via a polarimetric two-scale model in hilly or mountainous areas," *in Proc. SPIE SAR Image Anal., Modeling, Tech., Prague, Czech Republic, 2011*, vol. 8179, pp. 19.

[16] T. Jagdhuber, I. Hajnsek, and K. P. Papathanassiou, "An iterative generalized hybrid decomposition for soil moisture retrieval under vegetation cover using fully polarimetric SAR," *IEEE J. Sel. Topics Appl. Earth Observ. Remote Sens.*, vol. 8, no. 8, pp. 39113922, Aug. 2015.

[17] G. Di Martino, A. Iodice, A. Natale, and D. Riccio, "Polarimetric two-scale two-component model for the retrieval of soil moisture under

moderate vegetation via L-band SAR data," *IEEE Transactions on Geoscience and Remote Sensings.*, vol. 54, no. 4, pp. 2470-2491, Apr. 2016.

[18] S. R. Cloude and E. Pottier, "A review of target decomposition theorems in radar polarimetry," *IEEE Transactions on Geoscience and Remote Sensing.*, vol. 34, no. 2, pp. 498518, Mar. 1996.

[19] S. R. Cloude and E. Pottier, "An entropy based classification scheme for land applications of polarimetric SAR," *IEEE Transactions on Geoscience and Remote Sensing.*, vol. 35, no. 1, pp. 68-78, Jan. 1997.

[20] J. S. Lee, D. L. Schuler, and T. L. Ainsworth, "Polarimetric SAR data compensation for terrain azimuth slope variation," *IEEE Transactions on Geoscience and Remote Sensing.*, vol. 38, no. 5, pp. 21532163, Sept. 2000.

[21] X. Shen et al., Orientation angle calibration for bare soil moisture estimation using fully polarimetric SAR data," *IEEE Transactions on Geoscience and Remote Sensing.*, vol. 49, no. 12, pp. 49874996, Dec. 2011.

[22] Y. Oh, K. Sarabandi, and F. T. Ulaby, "An empirical model and an inversion technique for radar scattering from bare soil surfaces," *IEEE Transactions on Geoscience and Remote Sensing.*, vol. 30, no. 2, pp. 370381, Mar. 1992.

[23] *DSM, DTM telerilevati mediante tecnologia Lidar*, (volo anno 2009/12). [Online]. Available: http://sit.cittametropolitana.na.it/lidar.html.

[24] G. Franceschetti, M. Migliaccio, D. Riccio, "SAR simulation of actual ground sites described in terms of sparse input data", *IEEE Transactions on Geoscience and Remote Sensing*, vol. 32, no. 6, pp. 1160-1169, Nov. 1994.

[25] Y. L. Tong, *The Multivariate Normal Distribution,* Springer-Verlag, New York, 1990.

[26] Available online: https://airsar.jpl.nasa.gov/.

[27] J.-S. Lee, D. L. Schuler, T. L. Ainsworth, E. Krogager, D. Kasilingam, and W. Boerner, "On the estimation of radar polarization orientation shifts induced by terrain slopes, *IEEE Transactions on Geoscience and Remote Sensing.*, vol. 40, no. 1, pp. 3041, 2002.

[28] C. Yang, J. Shi, Q. Liu, and Yang Du, "Scattering From Inhomogeneous Dielectric Cylinders With Finite Length", *IEEE Transactions on Geoscience and Remote Sensing.*, vol.54, no.8, pp. 4555-4569, 2016.

[29] M. Kvicera, F. Prez Fontn, J. Israel, and P. Pechac, "A New Model for Scattering From Tree Canopies Based on Physical Optics and Multiple Scattering Theory", *IEEE Transactions on Antennas Propag.*, vol.65, no.4, pp.1925-1933, 2017.

[30] G. Franceschetti, A. Iodice, D. Riccio, G. Ruello, "SAR Raw Signal Simulation for Urban Structures", *IEEE Transactions on Geoscience and Remote Sensing.*, vol.41, no.9, pp.1986-1995, 2003.

[31] O. Dogan and M. Kartal, "Efcient Strip-Mode SAR Raw-Data Simulation of Fixed and Moving Targets", *IEEE Geosci. Remote Sens. Lett.,* vol.8, no.5, pp.884-888, 2011.

[32] H. Chen, Y. Zhang, H. Wang, and C. Ding, "SAR Imaging Simulation for Urban Structures Based on Analytical Models", *IEEE Geosci. Remote Sens. Lett.,* vol.9, no.6, pp.1127-1131, 2012.

[33] T. Yoshida and C.-K. Rheem, "SAR Image Simulation in the Time Domain for Moving Ocean Surfaces", *Sensors,* vol. 13, no. 4, pp. 4450-4467, 2013.

[34] F. Zhang, C. Hu, W. Li, W. Hu, and H.-C. Li, "Accelerating Time-Domain SAR Raw Data Simulation for Large Areas Using Multi-GPUs", *IEEE J. Sel. Topics Appl. Earth Observ. Remote Sens.,* vol. 7, no. 9, pp. 39563966, 2014.

[35] K.-S. Chen, L. Tsang, K.-L. Chen, T. H. Liao, and J.-S. Lee, "Polarimetric Simulations of SAR at L-Band Over Bare Soil Using Scattering Matrices of Random Rough Surfaces From Numerical Three-Dimensional Solutions of Maxwell Equations", *IEEE Transactions on Geoscience and Remote Sensing.*, vol.52, no.11, pp.7048-7058, 2014.

[36] B. Liu and Y. He, "SAR Raw Data Simulation for Ocean Scenes Using Inverse Omega-K Algorithm", *IEEE Transactions on Geoscience and Remote Sensing.*, vol.54, no.10, pp.6151-6169, 2016.

[37] G. Franceschetti, M. Migliaccio, and D. Riccio, "On ocean SAR raw signal simulation," *IEEE Transactions on Geoscience and Remote Sensing.*, vol. 36, pp. 84100, Jan. 1998.

Chapter 6

Conclusions

For more than 30 years, radar remote sensing has established itself as an indispensable tool for Earth surface monitoring, especially for the areas where constant/continuous in-situ inspections are impossible. The most important capability of microwave remote sensing in comparison with the optical methods is the day and night time operation, under almost any kind of weather conditions. The other notable features of radar remote sensing is the usage of longer wavelengths (λ), and ability to penetrate (and get information) into (from) materials like vegetation, leaves, fog, soil, rock, etc.

Firstly EM field characteristic and polarimetric remote sensing fundamentals useful for understanding of concepts have been illustrated. Then the fundamental characteristics of SAR and InSAR have been given. EM fields, SAR/InSAR, and polarimetric remote sensing (Pol-SAR) being vast subjects, ranging from physics to algebra; for the sake of brevity, solely the concepts directly related to the algorithms that developed, have been discussed.

Chapter four, concerns about the PSI analysis and modeling that was carried out for a case study in the Campania region, Italy. 25 X-band radar images of Cosmo-SkyMed satellites from Campania during the time span of February 24 2011 to March 23 2015, modelled and analyzed with InSAR and PSI methodologies. We have focused our analysis on a railway and in particular on a railway bridge over the Volturno river, at Triflisco.

The use of higher resolution imagery has allowed us to obtaining a much larger number of persistent scatterers compared to previous studies on the same area, so that more reliable results have been obtained. Given the average of more than 190 thousand persistent scatterers for an area $56km^2$, velocities and ensemble coherence are measured in the rate of $-1.8mm/yr$ and 73% respectively. On the bridge over the Volturno river (the main target), 30 PSs have been obtained. In the studied time series, minimum velocity of -0.9 and maximum of $0.05mm/yr$ with average of $-0.3mm/yr$ and $SD = 0.3mm/yr$ have been observed, demonstrating very stable and safe conditions on the bridge. Comparison of average PSs time series on the bridge with thermal data shows that most of the Line Of Sight (LOS) changes are due to the periodic, seasonal variations of temperature (i.e., winter and summer).

In chapter five, a fully polarimetirc SAR simulator, which we named "Pol-SARAS", has been presented. It is based on the use of sound direct electromagnetic models and it is able to provide as output the simulated data of all the three polarization channels in such a way as to obtain the correct covariance or coherence matrixes on the final focused images.

Pol-SARAS has been compared to available theoretical models in terms of significant polarimetric quantities, i.e., $H - \alpha$. Moreover, the potentialities of the simulator in support of soil-moisture retrieval applications have been investigated.

The proposed simulator has been shown to provide results in agreement with what predicted by available theoretical models. In addition, polarimetric data obtained from simulated raw signals have been shown to agree with those obtained from a real SAR sensors. Furthermore, the potentialities of the simulator in support of some practical applications of SAR polarimetry have been investigated. In particular, with regard to soil-moisture retrieval, the possibility to simulate scenes presenting anisotropic macroscopic roughness has been exploited to demonstrate that the use of *copol-corr* look-up tables have to be preferred to *copol-crosspol* ones for the estimation of ϵ, in presence of surfaces that may present an anisotropic roughness.

With regard to the rotation angle estimation from polarimetric SAR data, presented results show that, to avoid underestimation, sufficiently large windows must be used in computing the coherency matrix elements.

Finally, the usefulness of the simulator for the analysis of polarimetric classification schemes has been also discussed. In particular, one example of the application of $H - \alpha$ analysis has been presented.